Max Planck Institut für Kolloid und Grenzflächenforschung

Heteroatom-containing carbons for high energy density supercapacitor

Dissertation

zur Erlangung des akademischen Grades
"doctor rerum naturalium"
(Dr. rer. nat.)
in der Wissenschaftsdisziplin "Kolloidchemie"

eingereicht an der
Mathematisch-Naturwissenschaftlichen Fakultät
der Universität Potsdam

von

Kang Ko Chung

Potsdam, im Juli 2013

EIDESSTATTLICHE ERKLÄRUNG /STATUTORY DECLARATION

"Hiermit erkläre ich an Eides statt, dass ich die vorliegende Dissertation selbständig und ohne Hilfe verfasst, keine anderen als die angegebenen Quellen und Hilfsmittel benutzt und wörtlich oder inhaltlich entnommene Stellen als solche kenntlich gemacht habe."

Potsdam, im Juli 2013

"I herewith formally declare that I myself have written the submitted dissertation independently. I did not use any outside support except for the quoted literature and all the other sources which I employed producing this academic work, either literally or in content."

Potsdam, in July 2013

Kang Ko Chung

Table of contents

Chapter 1

General introduction

1.1. Motivation

Since industrial revolution had occurred in the 18th century, humankind has been utilizing a limited resource of fossil fuels for making our lives affluent and convenient. They have been now mainly consumed for obtaining motive power sources by sliding piston in automobiles and by rotating turbine in thermal power stations. As a consequence, the exhaust gases such as carbon dioxide (CO_2), nitrogen oxides (NO_x) and sulphur oxides (SO_x) have been affording severe environmental problems, exemplified by acid rain, global warming and respiratory diseases. From this viewpoint, renewable energies utilizing solar, tide, wind, etc were developed so that humankind could accomplish a sustainable growth in the next decades. However, its production is decoupled from the actual energy consumption. In order to store or release the harvested energy on demand, high-performance energy storage devices are needed in order to complete renewable energy grids. Therefore, devices such as batteries and supercapacitors have been receiving ever-growing interest.

Lithium ion battery (LIB) is one of the most studied and commercially employed energy storage devices among batteries, affording a high energy density,[1] but a low power density, and a limited cycle life (up to 4500 cycles).[2] In addition, transition metals such as cobalt, manganese, etc has to be typically used in cathode material; they are not abundant in nature and their waste can do damage to our environment. Moreover, flammability of LIBs has been a big problem possibly due to the deposition of lithium metal as dendrites in the system. Li is stable only in inert atmosphere and flammable in air. Despite the great efforts for overcoming the drawback, fire accidents in which the exposure of lithium metal in air seems their cause sometimes occur.[3] Other devices such as lithium-air, lithium-, and sodium-sulphur batteries have also been investigated,[2] but the use of air-sensitive element of lithium or sodium is still necessary. From these reasons,

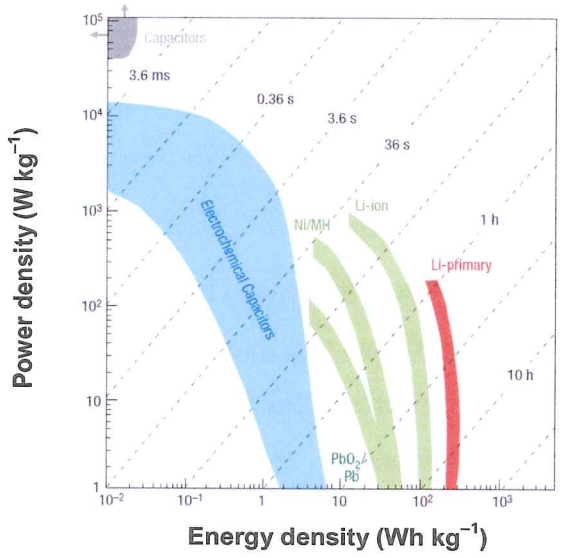

Figure 1–1 Plots of power density over energy density (Ragone plot) for various energy storage systems.[1]

Times shown are the time constants of the devices, obtained by dividing the energy density by the power. In the figure, PbO_2/Pb is lead-acid battery, Ni/MH is nickel metal hydride battery and Li-ion is lithium ion battery (LIB).

safer and more sustainable energy storage devices with comparable properties as LIBs should be urgently established. Supercapacitors, which are also referred to as ultracapacitors, are of focal interest as their construction allows for addressing most of the drawbacks of batteries; high power density, long cycle life (> 10^5 times), fast charge/discharge process, higher chemical safety and especially a construction potentially free of expensive transition metals and even lithium.[4] However, to make the supercapacitor to equal and overcome the properties for batteries, the issue on lower energy density must be solved.[4] Plots of power density over energy density (the so-called Ragone plot) for each device are shown in Fig. 1–1.

The energy density (E) and the power density (P) of a supercapacitor cell can be defined as equations (1–1) and (1–2):[5,6]

$$E = \frac{1}{2} CV^2 = \frac{1}{2} QV \qquad (1\text{–}1)$$

$$P = \frac{V^2}{4R_s} \qquad (1\text{–}2)$$

where C is the capacitance of the cell, V is the cell maximal operation voltage, Q is the stored total charge in the supercapacitor, and R_S stands for the equivalent series resistance (ESR) of the supercapacitor, which is comprised of the electrode resistance, electrolyte resistance and resistance from the diffusion of ions in the electrolyte porosity.[7] From these two equations, it is clear that C, V and R_S are the three important parameters determining the supercapacitor's performance; enhancement of both C and V is essential for a real system competing on the market.

For that purpose, various approaches from electrode together with electrolyte have been intensively examined,[4,8–11] and stable performances of 200 Wh kg^{-1} (high capacity, low voltage material)[12] – 300 Wh kg^{-1} (lower capacity, high voltage material)[13] have been reported. A conceptually possible combination of a 3.6 Volt system with a 1000 F g^{-1} material would however enable to break the magic limit of 1 kWh kg^{-1}, which exceeds even the best current Li-ion technology (*ca.* 700 Wh kg^{-1}).

To improve capacitance, employment of pseudocapacitive electrodes such as transition metal oxides,[14–16] conductive polymers,[17–19] heteroatom-containing carbon materials[20–23] and their mixtures[24–27] are reported, which is described in detail in Chapter 2. Introducing not only pseudocapacive elements but also high surface area is important for providing sufficient site for redox reaction. As to electrolyte, ionic liquids (ILs) having higher operation voltage up to 6 V than conventional aqueous solutions or organic solvent systems have been recently intensively investigated.[28–30] And a new strategy of introducing redox-active additives, *e.g.* hydroquinone (HQ),[22,31] potassium iodide,[32,33] methylene blue,[34] *p*–phenylenediamine,[35] etc have also been studied, disclosing higher capacitances than conventional aqueous electrolytes. Details are depicted in Chapter 3.

Among these methods, the author has become the most interested in developing brand-new heteroatom-containing carbon materials for electrode. The material can be synthesized inexpensively in the similar way as the activated carbons (ACs), which is currently employed as the electrode material for supercapacitor in most cases, by choosing proper set of the precursor along with the pore-directing additive (templates or activating agents). Despite the tremendous reported examples so far, there is still much room for the exploration because infinite sets of the starting materials can be considered.

For preparing electrode of capacitor on current collector, several ways could be considered. Conventionally, the electrode film is fabricated from the mixture of porous carbon particles with additives such as binder polymer (polytetrafluoroethylene (PTFE) or polyvinylidene fluoride (PVDF)) and conducting agent (acetylene black, carbon black, etc) (Fig. 1–2 (1)). In this method, the film is formed by either of two methods; the dispersed mixture in solvent is coated onto current collector before evaporation of the solvent, or well-mixed components are pressed to produce the film. These are reliable methods benefiting from plenty of the commercialization examples, but it should not be the most effective structure for supercapacitor. The low interparticle transmission efficiency decreases the overall conductivity as a whole electrode because the film consists of assembly of the carbon particles which is typically surrounded by less-conductive binder. Decrease of the overall conductivity for the resulting electrode film negatively affects the properties. In addition, the number of process increases for the film fabrication, and the burdensome handling of small particles which might be harmful to humankind lowers the producibility.

For addressing the drawbacks in the method above, porous carbon films can be directly fabricated from the precursor and the additive (templates and/or activating agents) onto current collector in principle (Fig. 1–2 (2)). This method allows for fabrication of three-dimensional networks without contact resistance due to the continuous and homogeneous structure. The fact that extra materials do not have to be included should also contribute to maximize the conductivity together with the

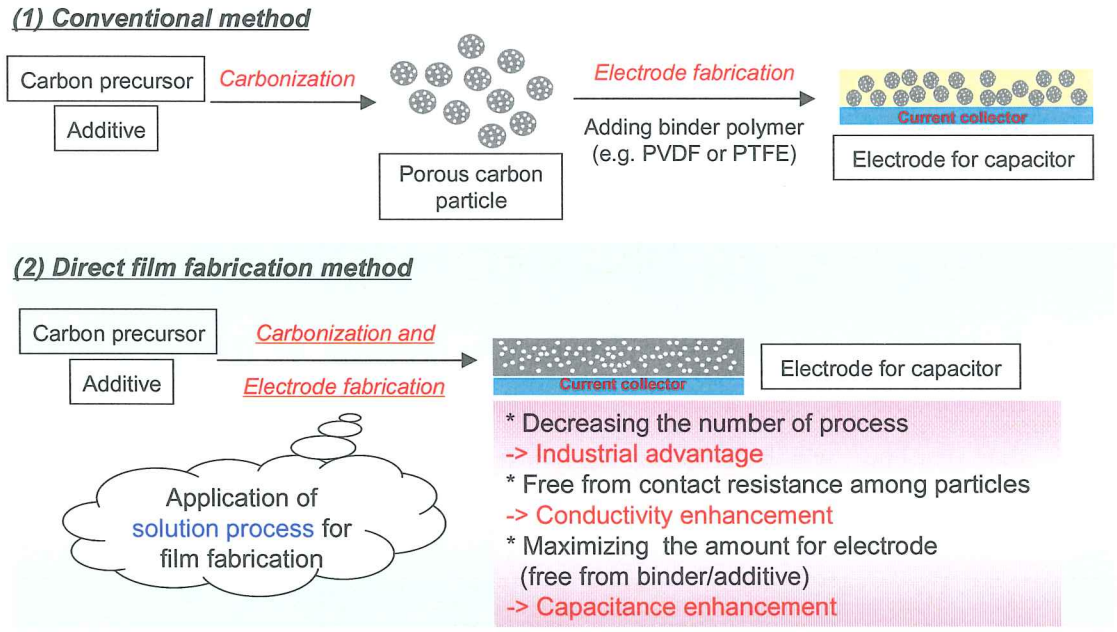

Figure 1–2 Schematic illustrations for electrode film fabrication.

capacitance. For fabrication of the film on current collector, solution processes such as spin coating, ink jet printing, etc is desirable when the process cost together with the possibility of large-area fabrication is taken into account. The number of process can be reduced for electrode fabrication without handling burdensome components. To date, carbon three-dimensional films have been fabricated by vapour process such as chemical vapour deposition (CVD) and physical vapour deposition (PVD) in most cases; examples for solution process are rather limited. Details are shown in Chapter 4. This attracted the author to prepare conductive carbon three-dimensional films with porous structures using solution process which could be applied as supercapacitor electrodes.

1.2. This work

With a view to achieving higher energy density for supercapacitor, a new carbon precursor for preparing heteroatom-containing carbons as electrode was considered. It is based on the prospect that the immediate commercialization can be put into practice by

the conventional method using a form of particles (Fig. 1–2 (1)), and that the direct film fabrication method (Fig. 1–2 (2)), by which the inherent issues of the former method such as contact resistance are solved, could be applied in the future. The precursor acrodam (Scheme 1–1), which was first appeared in 1958,[36] seemed appropriate from the reasons below:

1) It can be synthesized from inexpensive chemicals of diaminomaleonitrile (DAMN) and acrolein at ambient atmosphere.[37] Besides, the reaction time is less than one hour, which facilitates the industrial application. The reaction scheme is shown in Scheme 1–1.

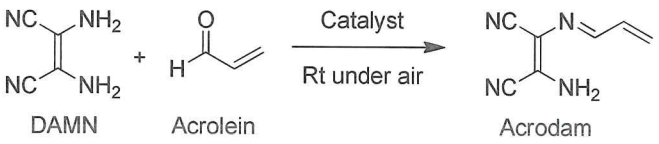

Scheme 1–1 Synthesis for acrodam.

2) The carbonization yield is reported to be as high as 60% after the 800 °C thermal treatment under nitrogen,[38] which is expected to contribute to both economic and environmental aspects. Besides in the case of film fabrication, the shrinkage can be reduced, which facilitates to obtain crack-free films with enough thickness.
3) Conductivity for the resulting particle is known to be 0.06 S cm^{-1},[38] which might be suitable for electrode material.
4) The material is known to oligomerize via consecutive addition, so it should be of advantage in preparing the solution for film fabrication using solution process. The proposed oligomerized form is shown in Fig. 1–3.

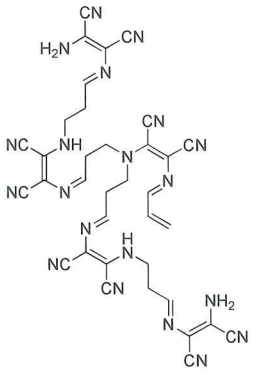

Figure 1–3 An oligomerized form example of acrodam.[38]

5) The high nitrogen content of acrodam (38 wt%) might affect positively the wettability towards electrolyte, along with build-up of pseudocapacitance. In addition, polarity originating from nitrogen atom might enhance the solubility in solvents.

In this doctoral dissertation, preparations, characterizations and electrochemical measurements of carbon particles as well as carbon three-dimensional films using the material of acrodam were carried out for the purpose of developing a high energy density supercapacitor that is comparable to batteries. Chapter 2 describes that porous carbon particles with the high surface area could be obtained by thermal treatment of acrodam along with caesium acetate (CsOAc) as a meltable flux agent, exhibiting promising properties as electrode for supercapacitor in aqueous electrolytes. In Chapter 3, redox-active aqueous electrolytes such as hydroquinone-loaded acidic solution were employed with the electrode described above for the purpose of attaining higher energy density. Some of the found energy densities are comparable to those of batteries. Chapter 4 discloses that conductive carbon three-dimensional films could be fabricated using spin coating method with the oligomer form of acrodam. The oligomer also allowed for preparing porous carbon films using an organic template, demonstrating the possibility for the application to supercapacitor electrode.

1.3. Fundamentals

1.3.1 Lithium ion battery and supercapacitor

The lithium ion battery (LIB) has been one of the most extensively studied energy storage devices. It has been already commercialized in automobiles, laptop computers, mobile phones, etc, benefiting from its high energy density stored in a relatively small volume and weight.[4] LIB consists of two electrodes that are an anode (negative) and a cathode (positive) where energy is stored and released through reversible redox reaction (Fig. 1–4).[8] The electrolyte typically contains lithium salts dissolved in an organic carbonate solution, for example a solution of lithium hexafluorophosphate ($LiPF_6$) in ethylene carbonate/diethylcarbonate. It should be a good ionic conductor and an electronic insulator. The electrodes in a LIB are separated by a porous polymer membrane. The storage capacity of a battery is given by the amount of lithium that can be stored reversibly in the two electrodes.

During the charging process, lithium ions are extracted from the cathode and simultaneously inserted into the graphitic carbon electrode, coupling with negatively charged electrons to keep overall charge neutrality. In addition, electrolyte reduction produces solid electrolyte interphase (SEI) films at the negative electrode (see Fig. 1–4). The formation of SEIs is associated with the irreversible consumption of both Li ions and the electrolyte. The process of SEI formation is detrimental to the specific capacity of the battery. However, stable SEIs stabilize the cycle life once formed. Much is known, but little is actually understood about the SEI, and many fundamental questions (formation details, chemical and phase composition, dynamic behaviour during charging/discharging, electrical and transport properties) remain unanswered. During the discharging process, lithium ions are reversibly extracted from the negative electrode and simultaneously inserted into the positive electrode. The lithium ions have to shift back and forth easily between the storage hosts of the cathode and anode. The electrochemical insertion/extraction process is a solid-state redox reaction involving electrochemical charge transfer coupled with the insertion/extraction of mobile guest ions into/from the

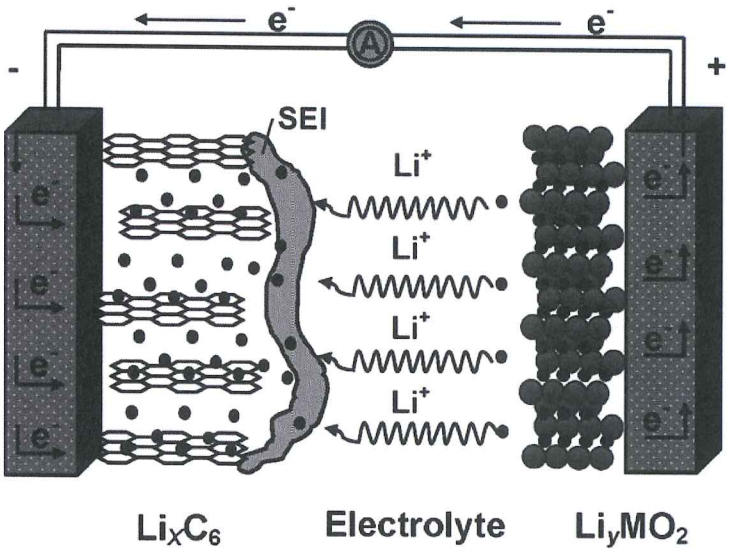

Figure 1–4 Schematic illustration of an intercalation-type lithium ion battery (LIB) in a charging process with graphite as anode and Li_yMO_2 as cathode.[39]

structure of the electronic and ionic conductive solid host. Typical chemical reactions in $LiCoO_2$ as cathode for example are:

$$Li_xC \rightleftharpoons C + x\,Li^+ + x\,e^- \qquad (1\text{–}3)$$

$$Li_{1-x}CoO_2 + x\,Li^+ + x\,e^- \rightleftharpoons Li_{x+y}CoO_2 \qquad (1\text{–}4)$$

Lithium has a very small atomic mass (6.94 g mol^{-1}), thereby reducing the weight of the battery drastically. In addition, lithium is extremely reactive, so it can give off a tremendous amount of energy in its chemical reactions, with a theoretical capacity of 3862 Ah kg^{-1} and higher potential (–3.05 V vs. normal hydrogen electrode), and these factors results in a rather, comparably high energy density of the cell.[40]

On the other hand, supercapacitor can be divided into two categories in principle; the electrical double layer (EDL) capacitance originates from pure electrostatic energy between ions and the charged surface of an electrode, and pseudocapacitance is

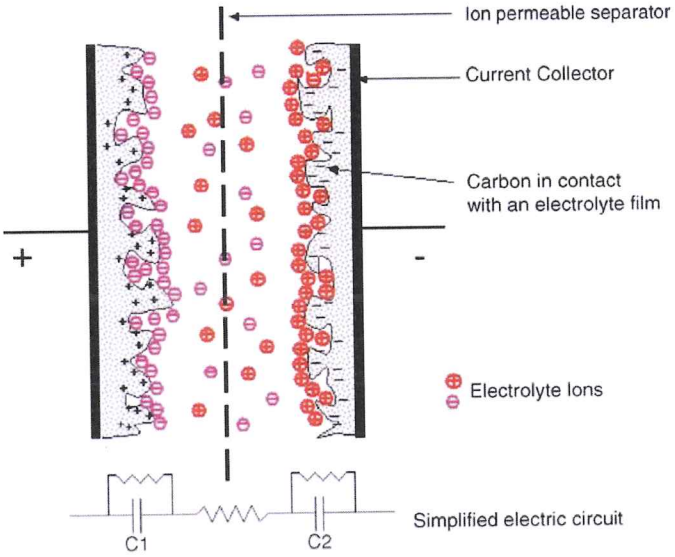

Figure 1-5 Schematic illustration for an electrochemical double layer based on porous electrode materials.[42]

associated with Faradaic charge transfer reactions (redox reactions) of the electroactive species to the surface of the electrode.[4,41]

Electrical double layer capacitor (EDLC) stores charge electrostatically through the reversible adsorption of the electrolyte ions onto active materials that are electrochemically stable and possess a high surface area. A schematic illustration of an EDLC is shown in Fig. 1–5. Schematically speaking, it consists of a pair of ideally polarizable electrodes which are immersed in an electrolyte and physically separated by a porous membrane through which ions can diffuse.[8] The electrolyte ions approach the electrode material, but do not react with it or are not absorbed into it. When a supercapacitor is charged, voltage (V) is applied across the two electrodes. The capacitance of an EDLC is assumed to follow that of a parallel-plate capacitor, determined by specific surface area of the electrode, the type of electrolyte and the effective thickness of the double layer (the Debye length), according to the formula:[4]

$$C = \frac{\varepsilon_r \varepsilon_0 A}{d} \qquad (1\text{–}5)$$

where C is capacitance of the EDLC, ε_r is the electrolyte dielectric constant, ε_0 is the dielectric constant of the vacuum (8.854×10^{-12} F m^{-1}), d is the effective thickness of the double layer and A is the electrode surface area. Only the surface that is accessible to electrolyte ions can contribute to charge storage; therefore, optimization of pore size, pore structure, surface properties and conductivity of the electrode materials is required. This storage mechanism of EDLCs enables excellent properties such as very fast energy uptake and delivery and high stability during up to millions of charge/discharge cycles.

In contrast to EDLCs, pseudocapacitors involve redox reactions between the solid electrode materials and the electrolyte. In this case, charges accumulated in the capacitor are strongly related to the electrode potential as follows;[4]

$$C = \frac{dQ}{dV} \qquad (1\text{–}6)$$

where C is the capacitance of the pseudocapacitor, Q is the quantity of charge, and V is the potential. Pseudocapacitors typically show much higher capacitance than that of EDLCs, but often suffer from low power density and lack of stability due to poor electrical conductivity and framework swelling during cycling. Nevertheless, it is important to note that although EDLCs and pseudocapacitors are differentiated on the basis of the predominant charge storage mechanism, all capacitors exhibit both mechanisms to some extent.[7]

Now supercapacitors are commercialized in uninterruptable power supplies (UPS), regenerative brake systems for automobile, train, etc, and backup energies for laptops, cameras, mobile phones, etc.[4] However, the size for supercapacitor market is not so large as the one for batteries; the sales for supercapacitor in the year 2009 were 275 million dollars[43] whereas they were about 10000 million dollars for batteries.[44] In order for supercapacitor, which is a safer and more environment-friendly device, to be alternative or supplement to batteries in the energy storage field, it is definitely required

to enhance its energy density while retaining their intrinsic high power density as shown in the section 1.1.

1.3.2. Porous carbon materials

Carbon materials are utilized in vast kinds of state-of-the-art applications such as supercapacitors, batteries, sensors, wind power stations, airplanes, automobiles, for gas storage and for water and air purification,[32] benefiting from its thermal and chemical stability, conductivity, light weight, low friction coefficient, high abundance, etc. As far as the application to electrode materials for supercapacitor is concerned, the porous structure is essential for increasing interaction between the electrode surface and the electrolyte ions. Up until now, template-derived carbons, activated carbons (ACs), carbon nanotubes (CNTs), graphenes, etc are studied for electrode materials of supercapacitor. New carbon allotropes of CNTs[45] and graphenes,[46] which have received much attention recently, can also serve as capacitors but, due to their moderate surface area and porosity together with their high costs, the application as additives is more desirable for enhancing the conductivity or providing additional porosity to the main electrode material.[47] Hence, template-derived carbons and ACs are considered to be the promising electrode materials in terms of inexpensiveness together with relatively easy introduction of heteroatoms that is important in enhancing capacitance.

Template-derived carbons can be prepared using either of two classes of templates: hard and soft.[4] The soft template method involves cooperative assembly between the structure-directing agents (usually surfactants or copolymers[48,49]) and organic precursor species in solution.[50] Unlike most hard templates, soft templates are thermally unstable, thus being removed from the starting nanocomposites during thermal treatments. This means that additional operations after carbonization such as washing are not necessary in principle. Because of that, the soft template method is preferred especially in porous carbon film fabrications.[51] However, there are currently only limited examples of the successful fabrication of porous carbon using soft templating methods, which were recently reviewed by Zhao *et al.*[49,52]

Hard templates are materials with inherited porosity, that is, zeolites and ordered mesoporous silicates, or that assemble to form a porous network, such as colloidal silica spheres. After infiltrating the templates with a carbon precursor, followed by carbonization and etching of the template using hydrofluoric acid (HF) solutions, porous carbons are formed with the pore size and structure being an inverse replica of that from the original template. In general, most porous hard templates are prepared from soft templates; hence most hard-templating procedures, that is, those using mesoporous silicates, imply additional synthesis steps compared to the one-pot soft-templating method. The hard-templating method further requires the use of toxic reagents such as HF for the etching of siliceous templates, imposing environmental problems to the development of carbons despite the fact that it is a "green" technology to solve the present energy problems.[52,53]

On the other hand, activation is often used to increase the surface area of the material through the introduction of large amounts of micropores, being conducted physically or chemically.[4] Physical activation is conducted in the presence of suitable oxidizing gasifying agents (O_2, CO_2 or steam) to develop the porosity, usually in the temperature range of 600–1200 °C. Chemical activation is generally carried out by mixing carbonaceous materials with chemical activating agents (KOH, H_3PO_4, $ZnCl_2$, etc), followed by the carbonization at 400–900 °C. This process affords porous carbons with high specific surface areas of over 2000 $m^2\ g^{-1}$ and large pore volumes mainly made up of micropores and some small mesopores. Compared to physical activation, chemical activation has superior advantages such as lower activation temperatures, higher yields, less activation time, higher specific surface area and suitable micropore volume ratio, although it has disadvantages including the corrosiveness of the chemical agents and the necessary washing process to remove the agents.[54] For example, the mechanism of KOH activation has been intensively investigated, although it has not been well understood because of the large number of variables in both the experimental parameters and the reactivity of different precursors used. The previous results[55–57] indicate that

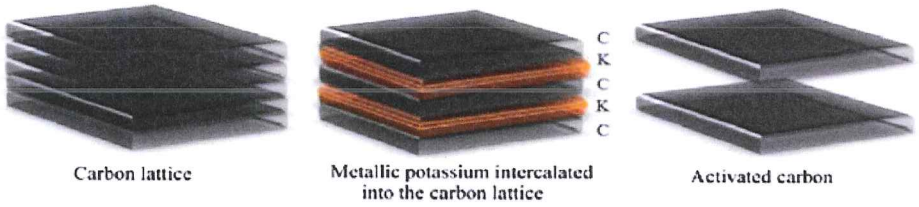

Figure 1–6 Activation mechanism using potassium hydroxide (KOH).[54]
This is done by the penetration of metallic K into the carbon lattices, the expansion of the lattices by the intercalated metallic K, and the removal of the intercalated K from the carbon matrix.

K_2CO_3 forms at about 400 °C. At about 600 °C, KOH is completely consumed in the ways such as the equations (1–7) to (1–10).

$$2\ KOH \rightarrow K_2O + H_2O \qquad (1–7)$$

$$C + H_2O \rightarrow CO + H_2 \qquad (1–8)$$

$$CO + H_2O \rightarrow CO_2 + H_2 \qquad (1–9)$$

$$CO_2 + K_2O \rightarrow K_2CO_3 \qquad (1–10)$$

The as-formed K_2CO_3 in equation (1–10), significantly decomposes into CO_2 and K_2O at temperatures higher than 700 °C (equation (1–11)) and completely disappears at 800 °C. Moreover, the resulting CO_2 can be further reduced by carbon to form CO at high temperature (equation (1–12)). The K compounds (K_2O and K_2CO_3) also can be formally reduced by carbon to produce metallic K at temperatures over 700 °C (equations (1–13) and (1–14)).

$$K_2CO_3 \rightarrow CO_2 + K_2O \qquad (1–11)$$

$$CO_2 + C \rightarrow 2\ CO \qquad (1–12)$$

$$2\ C + K_2CO_3 \rightarrow 3\ CO + 2\ K \qquad (1–13)$$

$$C + K_2O \rightarrow CO + 2\ K \qquad (1–14)$$

Based on the above observations and discussions, three main activation mechanisms for KOH activation of carbon can be concluded which have been widely accepted:[55–59]

a) Etching the carbon framework by the redox reactions between various potassium compounds as chemical activating reagents with carbon as shown in equations (1–13) and (1–14), called chemical activation, is responsible for generating the pore network.
b) The formation of H_2O (equation (1–7)) and CO_2 (equations (1–9) and (1–11)) in the activation system positively contributes to the further development of the porosity through the gasification of carbon, namely physical activation (equations (1–8) and (1–12)).[60]
c) The as-prepared metallic K (equations (1–13) and (1–14)), efficiently intercalates into the carbon lattices of the carbon matrix during the activation and results in the expansion of the carbon lattices in Fig. 1–6. After the removal of the intercalated metallic K and other K compounds by washing, the expanded carbon lattices cannot return to their previous nonporous structure and thus a high microporosity results.[54]

As can be assumed, the amount of charge accumulated in a supercapacitor is directly proportional to the surface area of the electrode. Hence, a well developed surface area of carbons seems to be a crucial parameter for efficient energy storage.[47] On the other hand, the specific surface area is closely related to the porosity of carbons, and the type of pores plays an important role in charge accumulation. Ions from the electrolyte can be effectively adsorbed only in the smallest pores (micropores) with a diameter below 2 nm, whereas mesopores (with diameters in the range 2–50 nm) usually adopt the role of transport channels for the ions which can be adsorbed in micropores.[61] Several investigators have carried out comprehensive studies on activated carbons to determine

correlation between the porous structure and the performance in supercapacitors. However, it was found that the specific capacitance was not proportional to total surface area as predicted by equation (1–5).[62–64] Two reasons were offered to explain this behaviour. Firstly, all surface area accessed by N_2 at 77 K (used to determine surface area) may not be accessible to the electrolyte and secondly that the local electroadsorption properties are dependent on pore size.[7] It clearly suggests that, apart from the well developed surface area, the porosity with an appropriate micro/mesopores ratio (reported in ref. 65 to be 20–50%) is necessary to enhance the capacitance values. Pore diameter should also perfectly fit the dimensions of the attracted ions to preserve favourable conditions for fast and effective electrostatic interactions.[66]

The selection of the carbon precursors is also very important for energy storage applications, taking into account the precursor availability and cost, the carbonization yield, and the presence of heteroatoms such as oxygen, nitrogen, boron and phosphor that could be incorporated into the final carbons and on the extent to which it can be graphitized. The search for new, available and inexpensive porous carbon sources has intensified, with focus on synthetic carbon sources that can combine all aforementioned properties. A large variety of carbon precursors are used such as biomass or of fossil origin, including alcohols,[67] carbohydrates, polysaccharides, lignocellulose sources,[68] cokes,[22] phenolic resins[69] and organic polymers.[23] Doping atoms, if contained in the precursors, can very beneficially contribute to build up pseudocapacitance, but activation processes usually remove significant amounts of them.[70]

Chapter 2

Enhancement of energy density using a new carbon storage material: Preparation of salt-flux carbon particles and their application to supercapacitor

2.1. Introduction

For the purpose of attaining a high energy density supercapacitor system, the heteroatom-containing carbon electrode having a superior capacitance was first established in this chapter. In order to obtain high capacitance, the materials exhibiting pseudocapacitive behaviour such as metal oxides, conductive polymers, heteroatom-containing carbon materials, etc have been recently energetically investigated by many researchers.

Metal oxides exhibit much higher specific capacitance than conventional activated carbons. For example, ruthenium oxide (RuO_2) is reported to display capacitance more than 600 F g^{-1} in an aqueous electrolyte.[14,15] Moreover, as high as 1300 F g^{-1} is reported in a hydrated RuO_2 ($RuO_2 \cdot xH_2O$).[16] This is attributed to their pseudocapacitive behaviour originating from the redox reaction below;[71]

$$RuO_2 + x\,H^+ + x\,e^- \rightleftharpoons RuO_{2-x}(OH)_x \qquad (2\text{–}1)$$

However, a satisfying electrochemical activity of this compound is obtained only in protic media, and owing to the high cost of ruthenium, the application field is limited to some special devices, *e.g.* for military applications.[47] Other inexpensive metal oxides such as manganese,[72] cobalt,[72–75] iron,[76] vanadium[77] and nickel[78–80] have been also studied in order to address the issue, but still have not reached commercialization because of their lower capacitances. For example, manganese oxides, especially manganese dioxide (MnO_2), have been paid much attention because of the low cost and the large potential window compared to the other metal oxides.[81] Manganese oxides generally

Table 2–1 Some of the recent reported examples of heteroatom-containing materials for the supercapacitor application in aqueous electrolytes.

Carbon precursor	Additive	Sample name	S_{BET}[a] ($m^2\ g^{-1}$)	Composition	Electrolyte	Electrochemical measurement	Maximal capacitance	Reference
Diaminomaleo-nitrile	Nothing	AMN1020K	230	$C_{2.0}N_{1.0}H_{0.73}O_{0.33}$	1 mol L^{-1} H_2SO_4aq	Three electrode	200 F g^{-1} (at 2 A g^{-1})	89
o-Phenylene-diamine	$FeCl_3$•$6H_2O$	AC-450	358	$C_1N_{0.23}O_{0.20}H_{0.64}$	1 mol L^{-1} H_2SO_4aq	Three electrode	690 F g^{-1} (at 0.1 A g^{-1})	20
Glucosamine	KOH	CA-GA-2	571	N 4.4%	1 mol L^{-1} H_2SO_4aq	Three electrode	280 F g^{-1} (at 0.2 A g^{-1})	90
Acrylonitrile and propylene by CVD	Zeolite	Y-AN	1680	N 6.0 wt% O 7.7 wt%	1 mol L^{-1} H_2SO_4aq	Two electrode	340 F g^{-1} (at 0.1 A g^{-1})	91
Benzene by CVD	MgO	CNC700	1854	Not shown	1 mol L^{-1} H_2SO_4aq	Two electrode	260 F g^{-1} (at 0.1 A g^{-1})	92
Sucrose	Mesoporous silica	H-CMK-8	1217	O 23.1 at% N 0.82 at%	2 mol L^{-1} KOHaq	Three electrode	246 F g^{-1} (at 0.5 A g^{-1})	93
Coke obtained from a coal tar pitch	KOH	KOH-650	1397	O 7.7wt%	1 mol L^{-1} H_2SO_4aq	Two electrode	351 F g^{-1} (at 65 mA g^{-1})	94
Semicoke	KOH	SP4-5	3204	O 4.1wt%	2 mol L^{-1} H_2SO_4aq	Two electrode	430 F g^{-1} (at 0.88 mA cm^{-2})	95

[a] Brunauer–Emmett–Teller surface area.

have the capacitance in the range from 150 to 250 F g^{-1}.[81,82] Prasad *et al.* reported a 400 F g^{-1} capacitance with an amorphous nanostructured hydrated manganese dioxide deposited on stainless steel;[83] however, it is much far from ruthenium system. Other disadvantages for manganese oxide supercapacitors belong to their instability in strong acidic and basic media along with their inherent low conductivity. These issues should be addressed in order to bring this system to commercialization.

Another promising material for high performance electrochemical capacitors is a conductive polymer, such as polyaniline (PANI),[17] polypyrrole (PPy),[84] polythiophene (PTh),[85,86] poly(3,4-ethyleno-dioxythiophene) (PEDOT)[18,19] and their derivatives.[87, 88] Khomenko *et al.*[89] revealed that the conductive polymer composites with carbon nanotubes (CNTs) as conductive support can afford 1100 F g^{-1} for a single electrode, in a selected potential range in 1 mol L^{-1} H_2SO_4 aqueous solution. However, in a two

electrode configuration, the capacitance drops dramatically to 360 F g^{-1} for the most promising composite. Besides, the long-term stability has revealed to be a problem owing to the repeated swelling and shrinking of conductive polymers during the charge/discharge process, which makes it difficult to attain position of the post-AC material.

The facts described above have been prompting many researchers to investigation on heteroatom-containing carbon materials. This class is intensively investigated because of its thermal and chemical stability, good electrical conductivity and high abundance.[6] The search for new, available and inexpensive porous carbon sources has been intensified. Some of the recent examples for heteroatom-containing carbon materials in which high capacitance could be achieved in aqueous electrolytes are shown in Table 2–1. In all the cases, nitrogen-rich precursors and/or activation methods are employed in order to introduce heteroatoms into the final carbons. However, some cases only disclosed the results using a three-electrode configuration which might lead to large errors when projecting the energy storage capability of an electrode material for supercapacitor use owing to the heightened sensitivity.[96] Besides in spite of the tremendous precedent investigations, the science is still far from optimization of the heteroatom-containing carbons because there are infinite sets of carbon precursors and additives (templates and/or activating agents) for the preparation. In order to control the final products precisely, employment of carbon precursors with a defined chemical structure is desirable. From this viewpoint, acrodam is a favourable choice for the carbon precursor in this study. The inexpensiveness, the high carbonization yield (60% after 800 °C heating)[38] and the high nitrogen doping yield (23 wt% nitrogen content after 800 °C heating)[38] should contribute to both economic and environmental aspects.

Originally carbon materials can have various kinds of functional groups on their surface, most of them being bonded with carbon atoms at the edge of hexagonal carbon

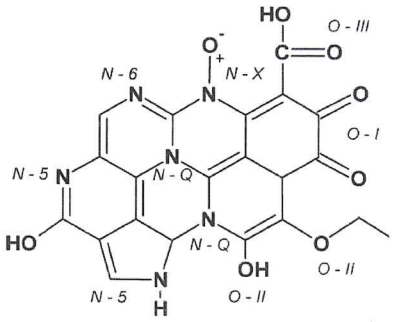

Figure 2–1 Schematic model of nitrogen- and oxygen-containing surface functional groups on carbon.[97]

layers. These functional groups contain often oxygen and/or nitrogen, such as –COOH, CO, pyridinic and pyrrolic nitrogen and others, depending strongly on the precursors and preparation conditions of the carbon material.[98] The schematic model of these functional groups are shown in Fig. 2–1. Some of these functional groups were considered to be acidic and electrochemically active, and to contribute to the capacitance of supercapacitors.[99] In the case of oxygen-containing functional groups, pseudocapacitance is generally considered to arise from redox reactions of these groups with electrolyte ions. However, the origin of increasing capacitance is not quite as simple as stated. The following reactions are postulated for different functional groups;[100]

$$>C{-}OH \rightleftharpoons >C{=}O + H^+ + e^- \qquad (2\text{–}2)$$

$$-COOH \rightleftharpoons -COO + H^+ + e^- \qquad (2\text{–}3)$$

$$>C{=}O + e^- \rightleftharpoons >C{-}O^- \qquad (2\text{–}4)$$

Oxygen-containing functional groups are simply formed by activation,[101,102] deliberately introduced on the surface of carbon by oxidation in O_2[103,104] or HNO_3,[105,106] or by electrochemical oxidation.[106,107] Oxygen species on the carbon surface can afford negative influence in non-aqueous electrolyte solutions, because they have unfavourable effects on the reliability of capacitors in terms of maximal operating voltage, self-discharge, leakage current, etc. In contrast, oxygen-containing functional groups increase

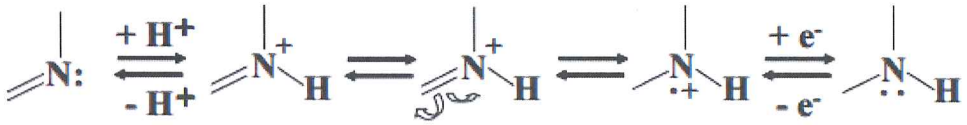

Figure 2–2 Possible pseudocapacitive reactions for the protonated nitrogen of nitrogen-containing carbon materials in the acidic solution.[89]

the total capacitance in aqueous electrolyte solutions like H_2SO_4, by developing pseudocapacitance.

Besides, nitrogen-containing carbon materials have recently attracted attention as well because a large pseudocapacitance was obtained even though they did not have a high surface area.[20,89] A high capacitance is not expected in non-aqueous electrolyte solutions, but only when the carbon materials were used as negative electrodes,[108] it appears that protons are associated with the pseudocapacitance due to nitrogen; however it was also reported that the capacitance increased in KOH solutions.[108,109] The possible mechanism for redox reaction of nitrogen-containing carbon materials in the acidic solution are shown in Fig. 2–2. For most of the nitrogen-containing carbons, however, the nitrogen content is not sufficiently high to explain the large enhancement in capacitance. Additional rationales are offered such as improving wettability of the pore walls by the formation of polar functional groups. At present, it is difficult to assign each contribution as well as to explain the effect of nitrogen incorporation reasonably. Linear relationships between capacitance and nitrogen content have been reported in a few individual cases,[110,111] but such correlation is difficult to be recognized. One of the reasons is that the contribution of double-layer capacitance is all different.

In this chapter, with the aim of attaining a high energy density for supercapacitor, the carbons were prepared from a polymer carbon precursor, acrodam, together with caesium acetate (CsOAc) as a meltable flux agent. Salt melt carbonization was just recently developed by to generate carbons with very high specific surface areas at adjustable pore volume.[112] We chose here CsOAc due to its appropriate larger atomic

size that might function as an ion pair template to generate defined micropores. Additionally, caesium salts are known to be rather polarizable flux agents that can solubilize polar polymers. These carbon materials are then tested as supercapacitor electrodes in conventional aqueous electrolytes of 1 mol L^{-1} sulphuric acid solution (H_2SO_4) together with 6 mol L^{-1} potassium hydroxide solution (KOH).

2.2. Results and discussion

2.2.1. Preparation of the salt-flux carbons and their characterization

The salt-flux carbons in this study were prepared by heating the mixture of acrodam and CsOAc at 700, 800 or 900 °C after the evaporation of their tetrahydrofuran (THF) / ethanol (EtOH) / water solution at 90 °C under ambient atmosphere. This means that carbonization process was performed in the presence of a salt melt that acts as a solvent and a porogen at the same time. Acrodam dissolves well in THF and a little in EtOH; on the contrary CsOAc dissolves well in water and EtOH to some extent. Therefore, EtOH plays an intermediary part for preparing a homogeneous solution from acrodam and CsOAc (Fig. 2–3a). The solution was evaporated to dryness without losing the homogeneity (Fig. 2–3b). The resulting material after the thermal treatment (Fig. 2–3c) was washed twice with pure water and pH 7 for the second aqueous filtrate was confirmed.

To identify if the caesium salt matrix works as a neutral template (no weight change), as an activation agent (reduces carbon mass) or even contributes to carbon formation (adds to the scaffold), the isolated yields after grinding were plotted over the CsOAc/acrodam weight ratio (Fig. 2–4). The samples are named "SFC–x–y", where "SFC" denotes salt flux carbon, "x" stands for the CsOAc/acrodam weight ratio and "y" for the thermal treatment temperature. It was found that at each carbonization temperature, the yield had a minimum; the yields for SFC–14–700, SFC–9–800 and SFC–4–900 were 42, 29 and 26%, respectively. Furthermore, the yields increased with raising the salt content again. This suggests that CsOAc is not a classical activation agent, but

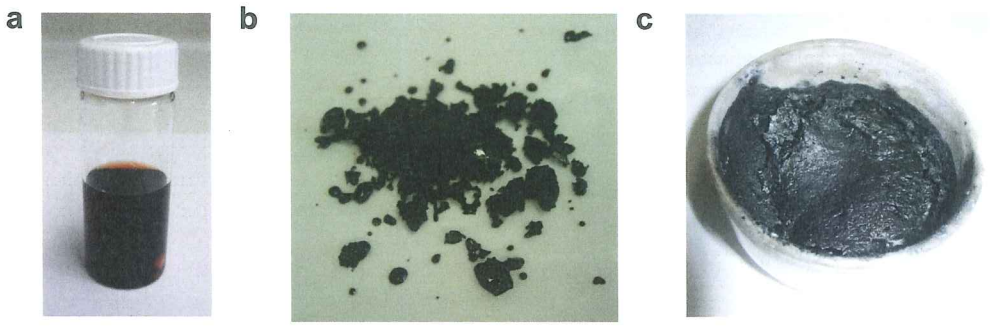

Figure 2–3 Digital photographs concerning preparation of the Cs salt-fulx carbons. **a,** THF/EtOH/water solution of acrodam and CsOAc before heating at 90 °C. **b,** Precursor for carbonization. **c,** Solid just after the thermal treatment before washing with water.

contributes by the decomposition of its organic counterion constructively to the carbon formation. Moreover, it should be noted that the yield for SFC–0–800, in which only acrodam was heated at 800 °C without CsOAc after evaporation of its THF/EtOH/water solution, was slightly lower than SFC–4–800. This is possibly because the precursor of SFC–0–800 is directly exposed to N_2 atmosphere during thermal treatment, facilitating evaporation of the decomposed volatile products. In SFC–4–800 on the other hand, the precursor is confined in a caesium salt-flux, while the CsOAc amount is still insufficient for a potential activation; therefore, the yield might have been raised.

For further understanding the role of CsOAc, anion analyses for the aqueous filtrate of SFC–9–800 after the caesium species removal from the carbonized sample were carried out (Table 2–2). The sample for measurement was prepared by collecting the first aqueous filtrate. It was found that most of them consisted of inorganic carbon (*e.g.* carbonate) and hydroxide ion (OH^-); acetate ion (OAc^-) was less than the detection limit. Their molar concentrations are calculated to be 6.26 mmol L^{-1} (inorganic carbon) and 3.16 mmol L^{-1} (hydroxide ion). This suggests that the CsOAc was completely decomposed to form the carbonate during the thermal treatment, and that some of the separated carbon species from the caesium salt participated in the final carbon scaffold.

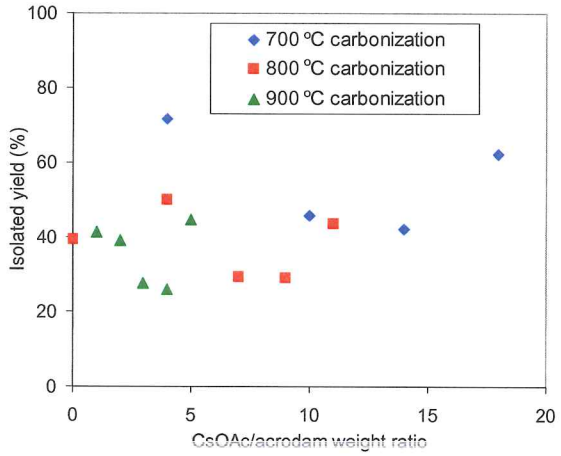

Figure 2–4 Relation of isolated yield to CsOAc/acrodam weight ratio.

Table 2–2 Anion analysis results for the first aqueous filtrate of SFC–9–800 after the caesium species removal.

Parameter	Result
pH value	11.5
Total inorganic carbon (TIC)	75.15 mg L^{-1}
Acetate (CH_3COO^-)	< 0.5 mg L^{-1}
Formate ($HCOO^-$)	10 mg L^{-1}
Chloride (Cl^-)	1.7 mg L^{-1}
Nitrate (NO_3^-)	0.1 mg L^{-1}
Sulphate (SO_4^{2-})	0.3 mg L^{-1}

In addition to the results below, it was found that fluoride (F^-), nitrite (NO_2^{2-}), chlorate (ClO_3^-), bromide (Br^-) and phosphate (PO_4^{3-}) ions were less than their detection limits.

The decomposition behaviour of the caesium species was also investigated by thermogravimetric analysis (TGA) under N_2 for CsOAc and the precursors with or without CsOAc (Fig. 2–5). In the measurement of the carbon precursor treated with CsOAc for instance, the solid just before the carbonization of SFC–9–800 was employed. The chart for only CsOAc exhibited the first drastic weight decrease at about 500 °C, which might correspond to formation of caesium carbonate by decomposition of the acetate. Considering the several per cent loss due to water evaporation at the beginning of

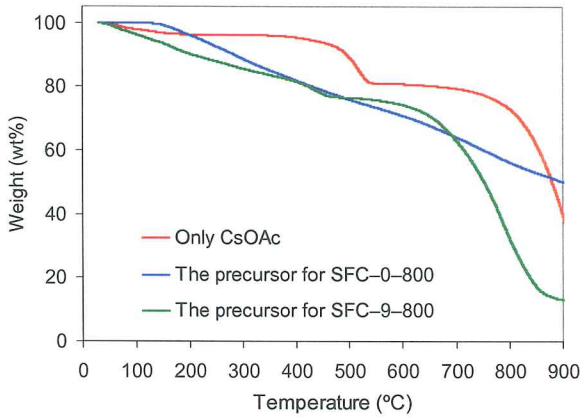

Figure 2–5 Thermogravimetric analysis (TGA) for the carbonization precursor.
In this figure, "Only CsOAc" means that only CsOAc without any treatment was used for the measurement, "The precursor for SFC–0–800" means the precursor solid was prepared by evaporating the THF/EtOH/water solution of acrodam, and "The precursor for SFC–9–800" means the precursor solid was prepared by evaporating the THF/EtOH/water solution of acrodam and CsOAc.

the measurement, the weight percentage value at plateau after the decomposition (about 600 °C) (81%) agrees very well to the theoretical weight ratio of the acetate to the carbonate (85%). The more intense weight decrease has started from about 800 °C that might reflect the onset of the carbonate decomposition, where most part of the decomposed including caesium metal (bp 671 °C) seems to begin evaporation. The test for the precursor with CsOAc ("The precursor for SFC–9–800" in Fig. 2–5) displayed the similar behaviour as "Only CsOAc" except that onset temperatures for the weight loss were lower. This might indicate that the presence of the carbon species accelerates decomposition of the caesium salts.

All the caesium salt-flux carbons in this study along with a commercially available AC reference, Norit DLC SUPRA 30 (Norit AC), displayed type–I sorption isotherms without hysteresis in the Brunauer classification (Fig. 2–6),[113] indicating that they express definitely microporous structures. The highest N_2 uptakes were observed in the lower yield samples, with SFC–9–800 exhibiting the highest surface area of 2413 m^2 g^{-1} in this study, applying the Brunauer–Emmett–Teller (BET) model (Table 2–3).[113] It

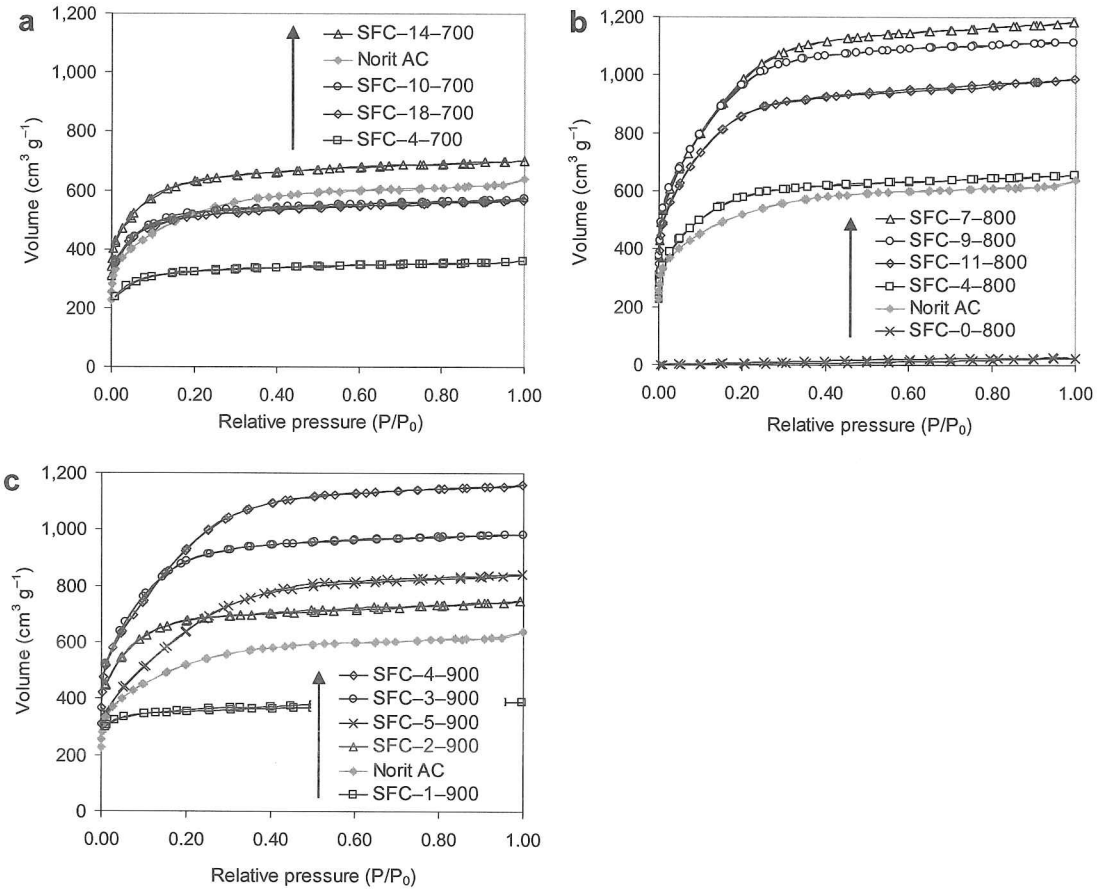

Figure 2–6 Nitrogen adsorption isotherms for the Cs salt-flux carbons.

a, For the 700 °C carbonized samples. **b,** For the 800 °C carbonized samples. **c,** For the 900 °C carbonized samples. The result for Norit AC was also indicated in each figure for comparison.

was significantly higher than Norit AC (1465 m^2 g^{-1}). When the samples with the lowest yield at each carbonization temperature are compared, SFC–9–800 together with SFC–4–900 had the similar N_2 sorption amount, but SFC–14–700 showed less N_2 uptake, indicating that heating temperature above 800 °C is necessary for obtaining high adsorption volume. It should be noted that SFC–0–800 showed little N_2 uptake, which means that the additional agent is needed to introduce the porous structure in this system. The pore size distribution, determined by the non-local density functional theory (NLDFT) equilibrium model method for slit pores,[114] displayed that most of the pore sizes lie in the supermicroporous range, with even larger percolation pores being smaller

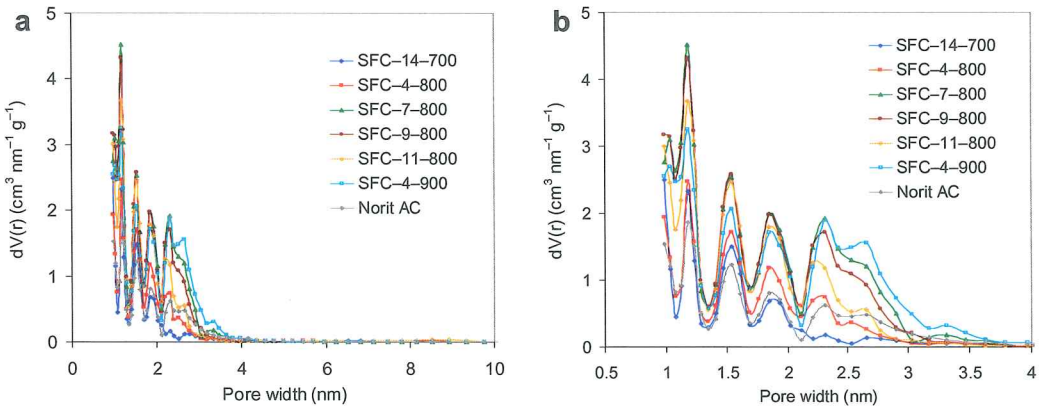

Figure 2–7 Pore size distributions for the Cs salt-flux carbons.

a, Pore width range of 0–10 nm. **b,** A magnification for **a**. The result for Norit AC was also indicated for comparison.

than 4 nm in each sample (Fig. 2–7). This nicely complies with the assumption that the caesium salts essentially act as a molecular template, that is carbonization takes place around ion pairs or small ion clusters. SFC–7–800 showed the highest pore volume of 1.64 mL g^{-1} of this series, along with 65% micropores (< 2 nm) (Table 2–3).

To quantify incorporation of heteroatoms, X-ray photoelectron spectroscopy (XPS) measurements were conducted (Table 2–4 and Fig. 2–8). In most of the samples, over 10 wt% of oxygen was found to be incorporated at the surface, which was higher than that for Norit AC (6.4 wt%). When the precursor for SFC–9–800 was prepared only by mechanically mixing of acrodam and CsOAc by a ball mill without solvent treatment, oxygen content for the resulting carbon was similar to the one with solvent treatment (Table 2–4). This indicates that the solvents for preparing the precursor (THF/EtOH/ water) are not the oxygen source. Considering the fact that the molecule of acrodam does not have any oxygen atom, oxygen-containing caesium species should be the source. Besides, there might be some contribution of gas adsorption onto the surface such as carbon dioxide (CO_2) and water. A finer analysis of the XPS O1s peaks (Fig. 2–9), gave for all the samples predominantly C–OH phenol groups and/or C–O–C ether groups

Table 2–3 Pore properties for the Cs salt-flux carbons.

Sample	S_{BET}[a] ($m^2 g^{-1}$)	Pore volume		
		Total[b] ($mL g^{-1}$)	Micro[c] ($mL g^{-1}$)	Micro/Total (%)
SFC–14–700	1679	0.97	0.74	76
SFC–0–800	11	0.04	0.03	73
SFC–4–800	1532	0.91	0.71	78
SFC–7–800	2400	1.64	1.06	65
SFC–9–800	2413	1.55	1.09	70
SFC–11–800	2176	1.36	1.03	75
SFC–4–900	2312	1.61	0.96	59
Norit AC	1465	0.86	0.62	72

[a] Total surface area calculated by the Brunauer–Emmett–Teller (BET) method using the P/P_0 range of 0–0.11.

[b] Total pore volume calculated at $P/P_0 = 0.995$ using the non-local density functional theory (NLDFT) equilibrium model method.

[c] The pore width is less than 2 nm.

Table 2–4 Elemental analysis results by combustion and X-ray photoelectron spectroscopy (XPS) for the Cs salt-flux carbons.

Sample	Elemental analysis (wt%)						
	XPS				Combustion		
	C	N	O	Cs	C	N	H
SFC–14–700	79.9	4.9	15.1	5.1	71.0	5.5	2.1
SFC–0–800	–[b]	–[b]	–[b]	–[b]	72.0	17.6	2.0
SFC–4–800	80.7	4.4	14.9	12.2	63.3	5.8	2.1
SFC–7–800	88.5	1.2	10.2	n.d[c]	88.0	2.2	1.1
SFC–9–800	87.6	1.4	11.0	1.1	86.2	2.6	1.3
SFC–9–800[a]	84.9	1.7	13.4	1.1	88.7	2.1	1.1
SFC–11–800	86.1	2.0	11.8	3.2	82.1	3.5	1.3
SFC–4–900	90.6	0.9	8.5	n.d[c]	91.7	2.4	1.1
Norit AC	93.6	n.d[c]	6.4	n.d[c]	94.0	0.3	1.0

[a] The precursor for carbonization was prepared without solvent treatment using THF/EtOH/water.

[b] Not measured.

[c] Not detected.

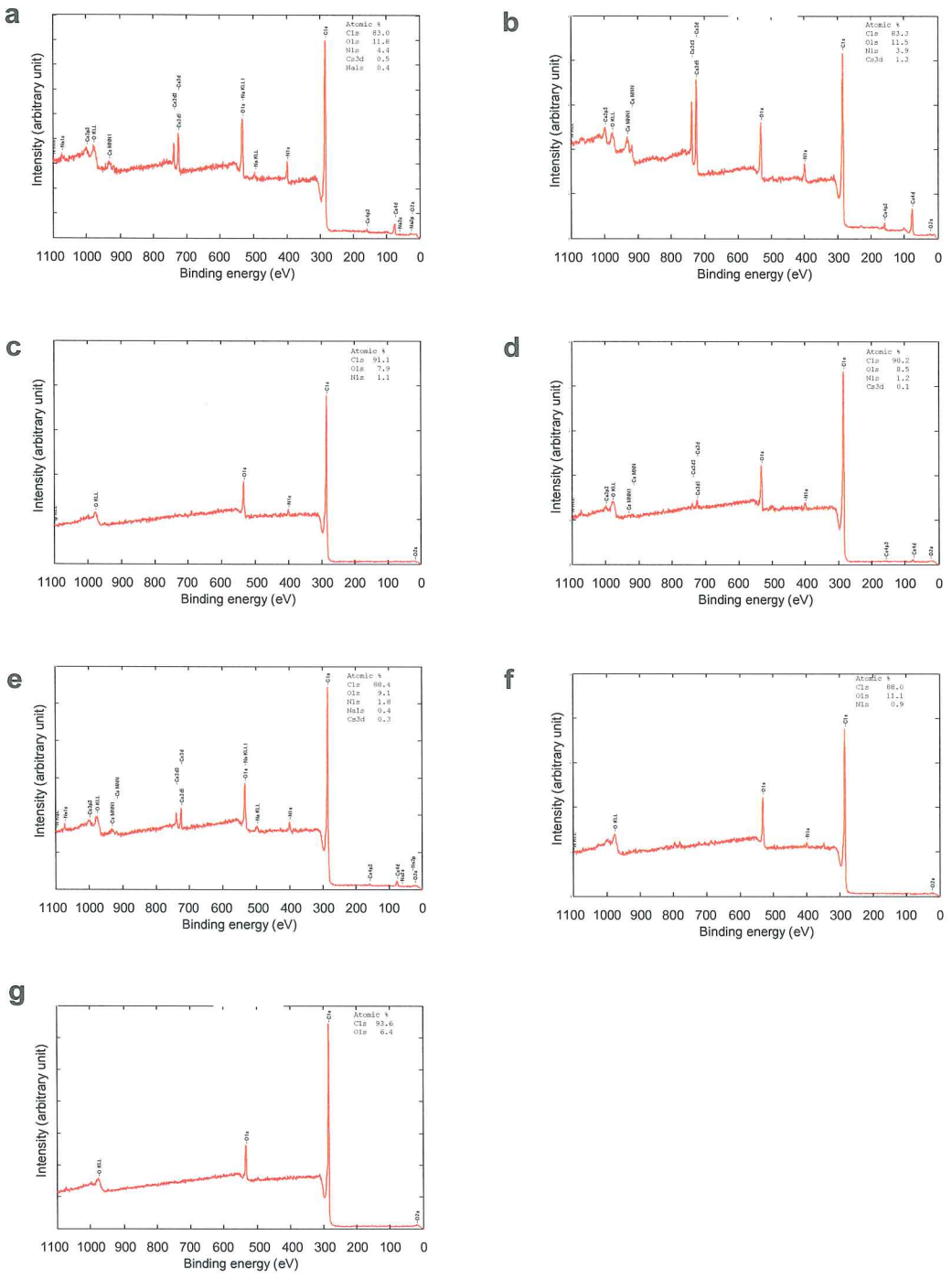

Figure 2–8 X-ray photoelectron spectroscopy (XPS) data for the Cs salt-flux carbons. **a**, SFC–14–700. **b**, SFC–4–800. **c**, SFC–7–800. **d**, SFC–9–800. **e**, SFC–11–800. **f**, SFC–4–900. **g**, Norit AC.

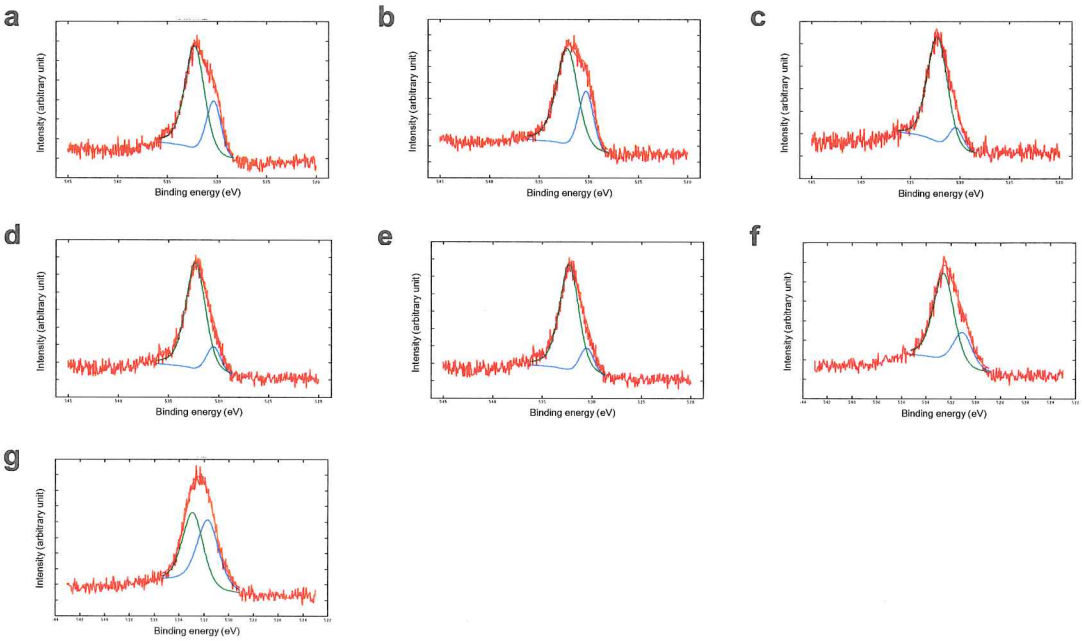

Figure 2–9 Chemical state analyses with XPS O1s for the Cs salt-flux carbons.
a, SFC–14–700. **b**, SFC–4–800. **c**, SFC–7–800. **d**, SFC–9–800. **e**, SFC–11–800. **f**, SFC–4–900. **g**, Norit AC.

centred at 532.2 eV, while the rest belongs to C=O quinone type groups centred at 530.4 eV.

On the contrary, most of surface nitrogen groups were lost during carbonization the content of which were as low as about 1 wt% in SFC–7–800, SFC–9–800 and SFC–4–900, as is often the case with nitrogen-containing systems.[98] When the lowest yield samples at each carbonization temperature were compared, their contents decreased with increasing the temperature, probably reflecting enhancement of the graphitization degree by loosing nitrogen. Combustion elemental analyses demonstrated slightly higher nitrogen contents than XPS, which suggests that the nitrogen atoms prefer to be inside the particles. It should be noted that the amount of caesium atom was confirmed to be negligible in the lower yield samples (SFC–7–800, SFC–9–800 and SFC–4–900) (Table 2–4 and Fig. 2–8) by XPS. Besides, the amount was found to be similar between the surface and the inside of the particles; the inductively coupled plasma-optical emission spectrometry (ICP-OES) analysis revealed that the content was 0.8 wt% in both SFC–7–

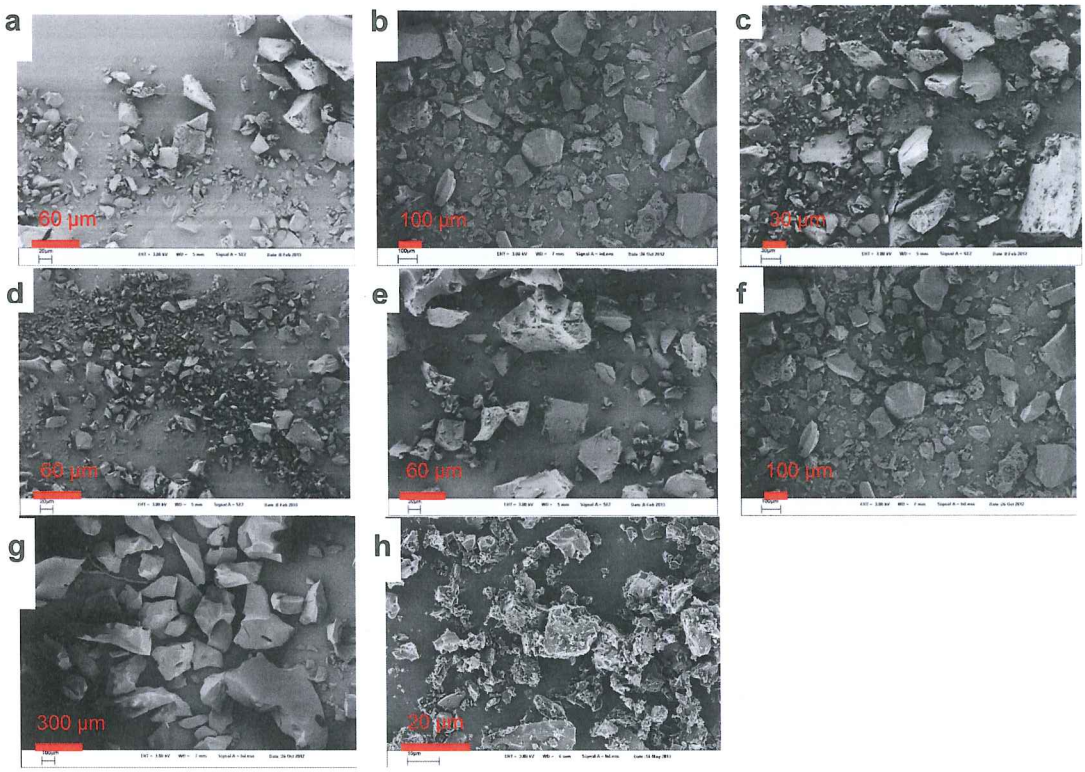

Figure 2–10 Scanning electron micrographs (overview) for the carbons.
a, SFC–14–700. **b**, SFC–0–800. **c**, SFC–4–800. **d**, SFC–7–800. **e**, SFC–9–800. **f**, SFC–11–800. **g**, SFC–4–900. **h**, Norit AC. Note that the scale is different in each figure.

800 and SFC–9–800. This indicates that the caesium salt can be easily removed by washing only with water.

Scanning electron microscopy (SEM) pictures revealed that the particle shape as well as the particle size distribution after grinding is rather similar with smooth surface in all the caesium salt-flux carbons observed (Figs. 2–10 and 2–11). The particle consists of approximately two kinds; the bigger one has particle size in the hundred micrometre region, and the smaller one in the several ten micrometre region. The smaller-size particle is capable of promoting the electrolyte diffusion by providing a short ion-transport pathway, the bigger one probably helping to keep the conductivity which enables the effective electron transport.[115] Their particle size was larger than Norit AC.

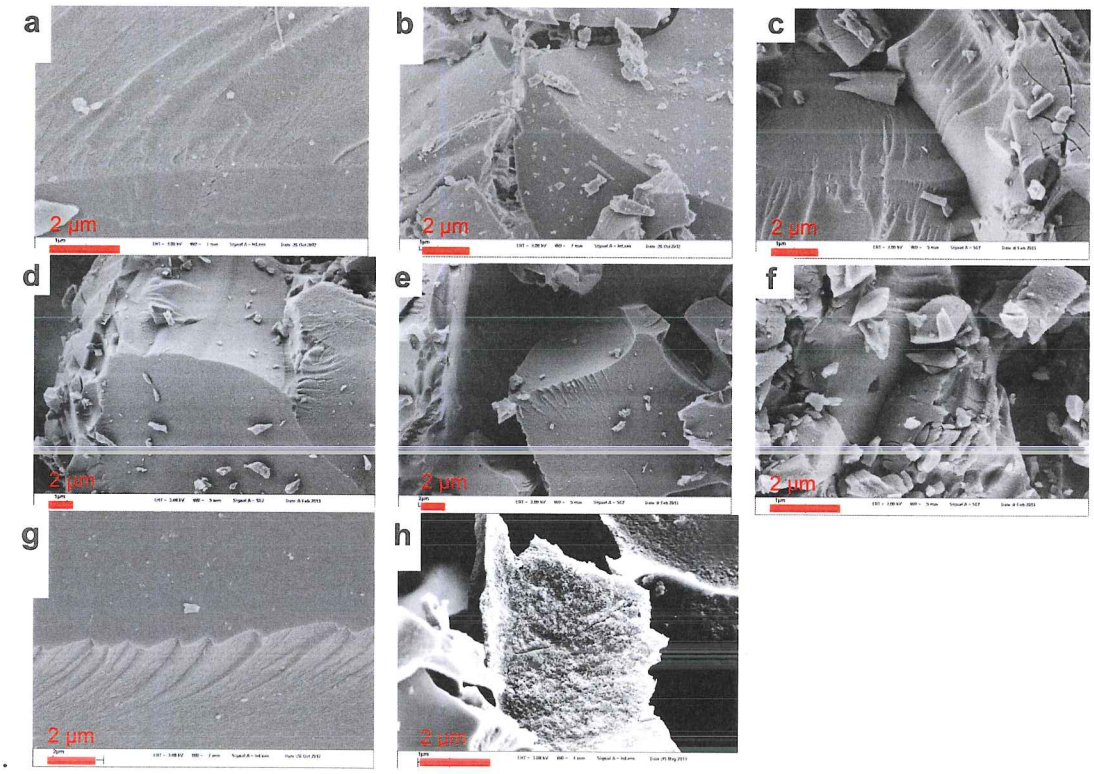

Figure 2–11 Scanning electron micrographs (magnification) for the carbons.
a, SFC–14–700. **b**, SFC–0–800. **c**, SFC–4–800. **d**, SFC–7–800. **e**, SFC–9–800. **f**, SFC–11–800. **g**, SFC–4–900. **h**, Norit AC. Note that the scale is different in each figure.

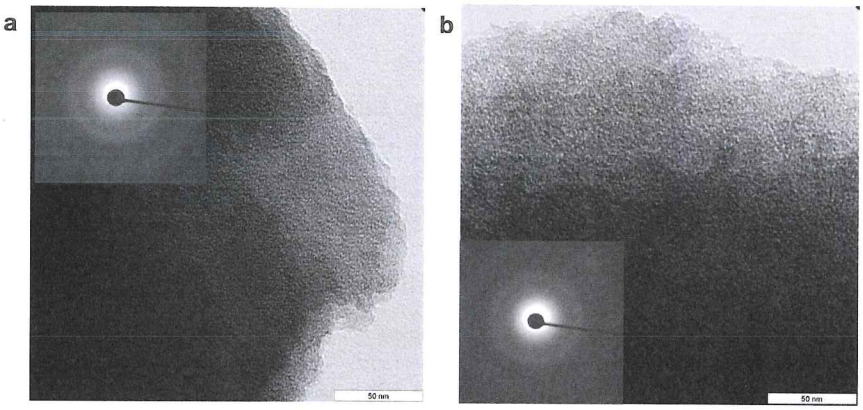

Figure 2–12 Transmission electron micrographs for the Cs salt-flux carbons.
a, SFC–7–800. **b**, SFC–9–800. Insets in figures: Selected-area electron diffraction (SAED) patterns.

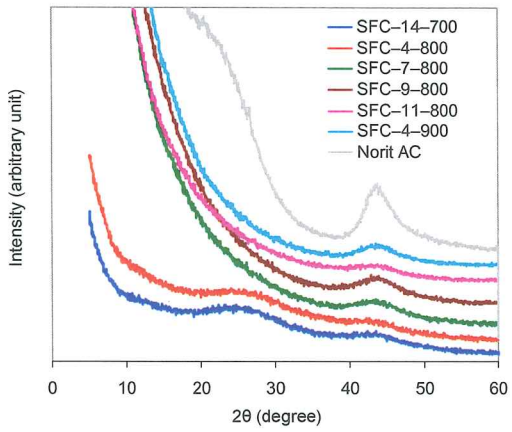

Figure 2–13 Wide angle X-ray scattering (WAXS) patterns for the Cs salt-flux carbons.

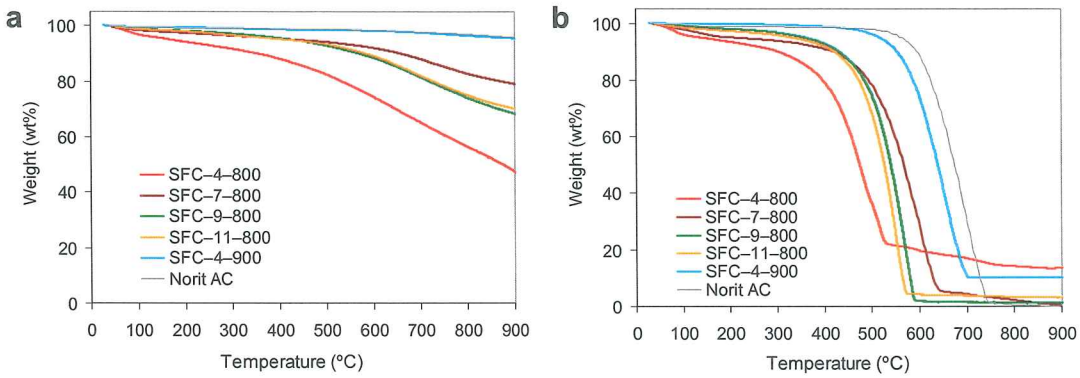

Figure 2–14 Thermogravimetric analysis (TGA) for the Cs salt-flux carbons.

a, Under N_2. **b**, Under synthetic air.

Transmission electron microscopy (TEM) pictures for SFC–7–800 and SFC–9–800 revealed a disordered structure of the porous carbons without crystallinity, which agrees well with their respective selected-area electron diffraction (SAED) analysis showing only amorphous halos (Fig. 2–12). Besides, the larger pores are already visible in these pictures.

The rather disordered structure of the caesium salt-flux carbons was also confirmed with wide angle X-ray scattering (WAXS) patterns (Fig. 2–13). The peak centred at 43° that correspond to the (100) plane of graphene sheets is expected to be broad for bended, high surface area materials. The peak was intensified in the higher temperature-carbonized and lower isolated yield samples. Another peak centred at 25°,

which corresponds to the typical (002) interlayer stacking, was only observed in SFC–4–800 and SFC–14–700. This supports that the single layers are highly dispersed by the presence of the salt, making the observation of stacking peaks rather improbable. The trend was similar to that for Norit AC.

Thermogravimetric analysis (TGA) under nitrogen atmosphere for the caesium salt-flux carbons exhibited a gradual decrease (Fig. 2–14a). The weight loss of SFC–4–900 was the smallest and similar to that for Norit AC with over 90% weight retention after 900 °C. In CsOAc–4–800 that has the highest oxygen content of the samples in this measurement, the retention was as small as about 40% at that temperature; oxygen atom in the carbons probably promoted the thermal decomposition. A similar trend was confirmed in the measurement under synthetic air (Fig. 2–14b); the order for onset temperature of decomposition corresponds to the measurement under N_2. It should be noted that practically all samples were stable in the air up to 500 °C.

2.2.2. Electrochemical properties for the salt-flux carbons in aqueous sulphuric acid electrolyte

Next, for understanding the electrochemical properties of these carbons some of which have fascinating surface area, pore size distribution, heteroatom contents and thermal stability, the electrochemical behaviour was investigated using a potentiostat equipment. All the measurements were conducted with a symmetrical two-electrode Swagelok® type cell using a piece of filter paper as separator, which is similar to a real supercapacitor. The electrode was fabricated from mixture of the carbon with polyvinylidene fluoride (PVDF) in the weight ratio of 90/10. The cyclic voltammetry (CV) charts with the voltage range of 0–1 V at the sweep rate of 2, 20 and 200 mV s^{-1} using 1 mol L^{-1} aqueous sulphuric acid solution (H_2SO_4) as electrolyte were shown in Fig. 2–15. First, the chart for SFC–0–800 without CsOAc treatment exhibited very small areas which mean low capacitances due to its low specific surface area. The lower yield carbons (SFC–7–800, SFC–9–800 and SFC–4–900) exhibited nearly rectangular voltammograms as Norit AC,

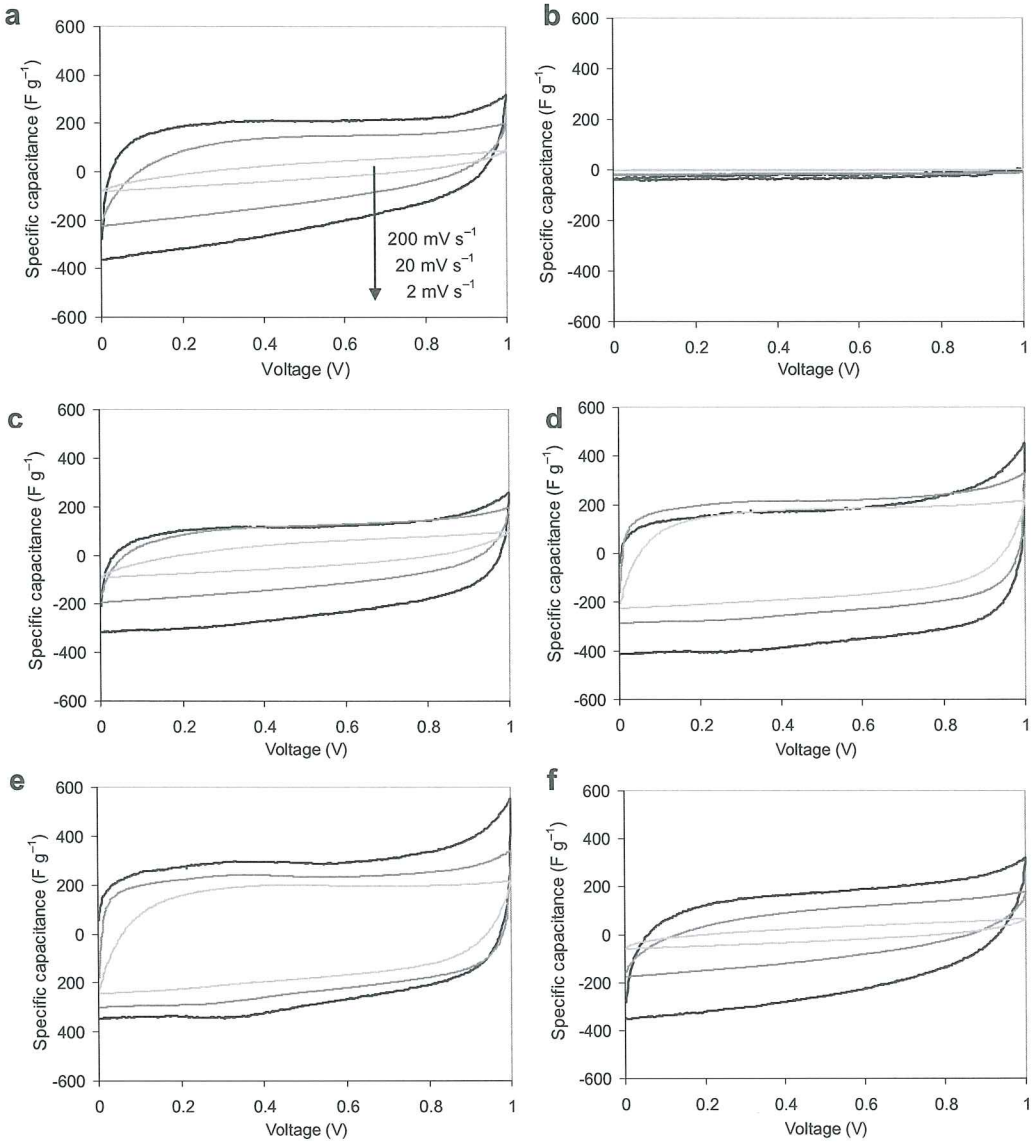

Figure 2–15 Cyclic voltammetry charts for the Cs salt-flux carbons in H_2SO_4 at the sweep rate of 2, 20 and 200 mV s^{-1}.

a, SFC–14–700. **b**, SFC–0–800. **c**, SFC–4–800. **d**, SFC–7–800. **e**, SFC–9–800. **f**, SFC–11–800.

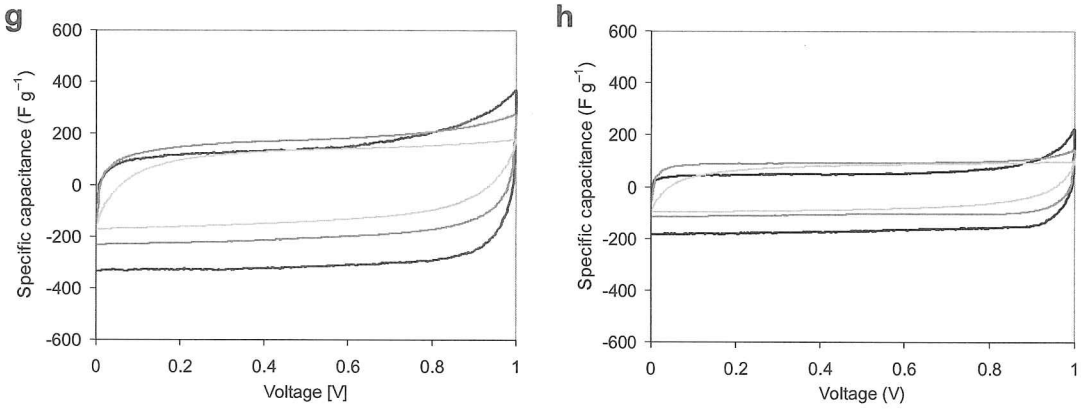

Figure 2–15 Cyclic voltammetry charts for the Cs salt-flux carbons in H_2SO_4 at the sweep rate of 2, 20 and 200 mV s^{-1} (continued).

g, CsOAc–4–900. **h**, Norit AC.

indicative of the contribution mostly from EDL capacitance. Nevertheless, small humps at about 0.4 V were detected in 2 mV s^{-1} charts of the 800 °C carbonized samples (SFC–7–800 and SFC–9–800) showing some pseudocapacitive behaviour due to redox reactions at oxygen and nitrogen sites. This is attributed to the high heteroatom contents that were demonstrated earlier in the elemental analyses (Table 2–4). The other samples with less developed pore structure (SFC–14–700, SFC–4–800 and SFC–11–800) gave the CV charts with distorted shapes. This reflects the decreased contribution from EDL capacitance because of their lower surface area along with their further higher heteroatom contents than the former three samples. It should be noted that a capacitance increase was detected in all the samples measured including Norit AC especially at 2 mV s^{-1} as the voltage approached to 1 V. This is probably due to the generation of hydrogen followed by the adsorption on the porous carbon surfaces which contributes to pseudocapacitance, as suggested by Beguin *et al.*[47]

In the galvanostatic charge/discharge profiles, which were recorded by varying the loading current density from 0.1 to 10 A g^{-1} (Fig. 2–16), the chart for the SFC–4–900 was nearly linear with the negligible curvature as Norit AC in all the current densities

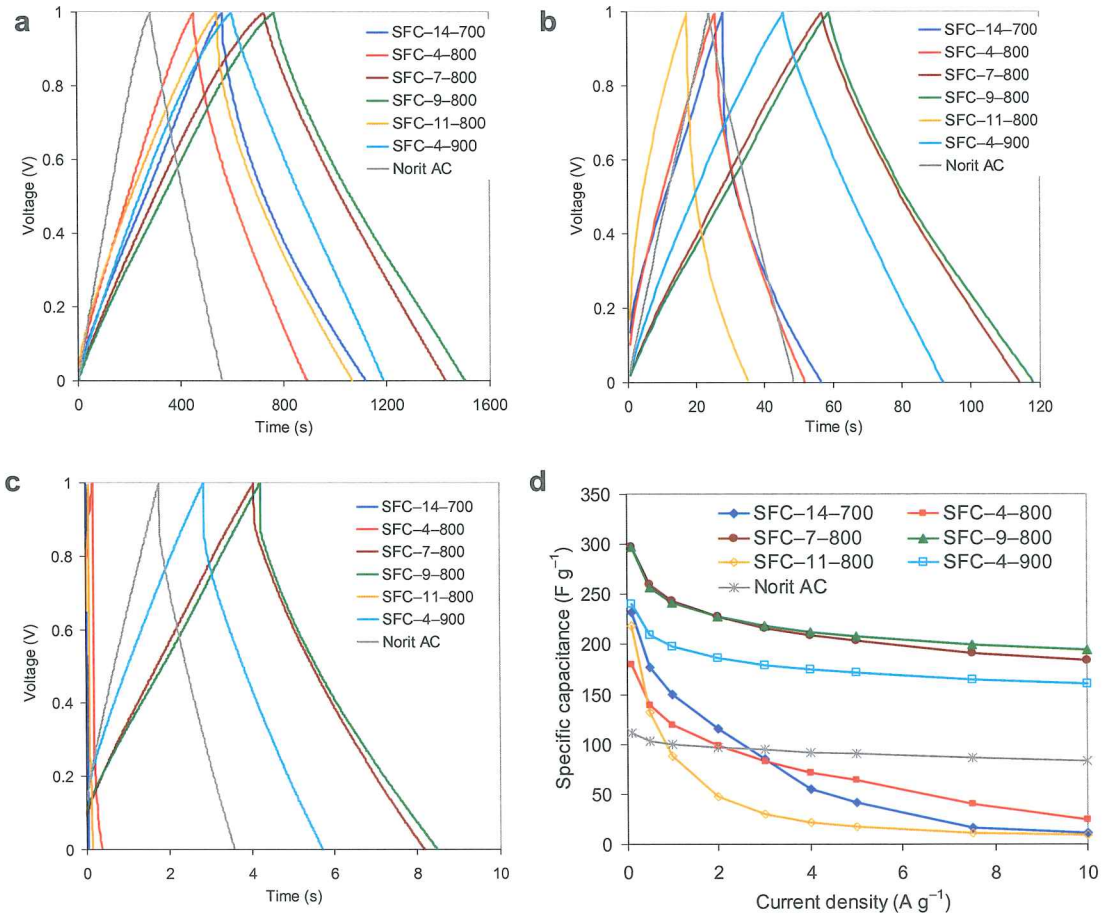

Figure 2–16 Galvanostatic charge/discharge profiles for the Cs salt-flux carbons in H_2SO_4. **a**, At 0.1 A g^{-1}. **b**, At 1 A g^{-1}. **c**, At 10 A g^{-1}. **d**, Relation of specific capacitance to current density calculated from the discharge curve.

recorded, suggesting that most of the capacitance consists of EDL capacitance. Some curvatures with deviation from straight line were observed in the other samples, indicating that pseudocapacitance was introduced to some extent due to increase of the heteroatom content. These trends definitely correspond to the CV shapes discussed earlier. Moreover, SFC–9–800 displayed the longest charge/discharge duration with small voltage drop at the beginning of the discharge process (IR drop). An IR drop in voltage should be ascribed to the variation in the quantity of ions accumulated within the double layers. A lower current density allows more time for ions to distribute and form a more

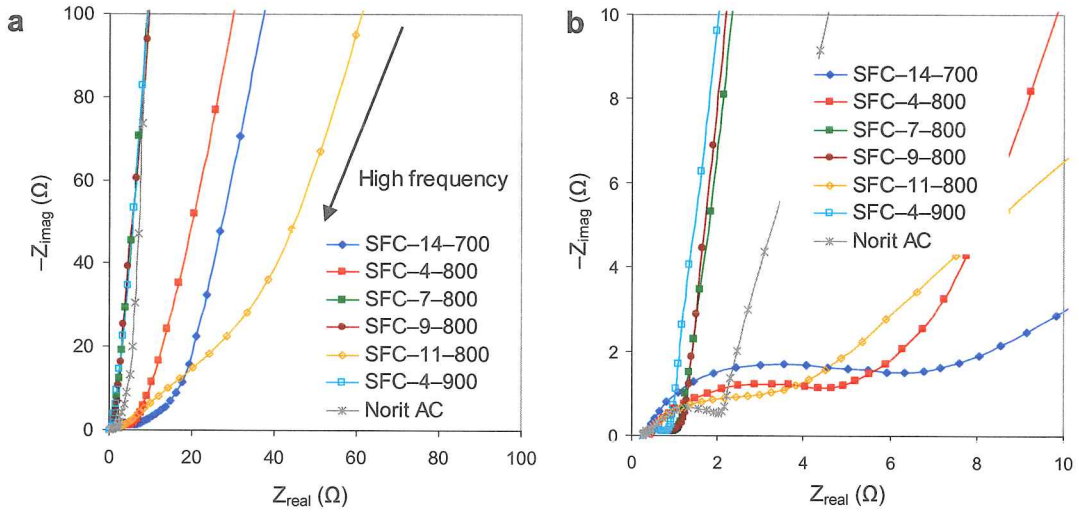

Figure 2–17 Nyquist plots for the Cs salt-flux carbons in H_2SO_4.

a, Plots for the Cs salt-flux carbons. **b**, A magnification of **a**.

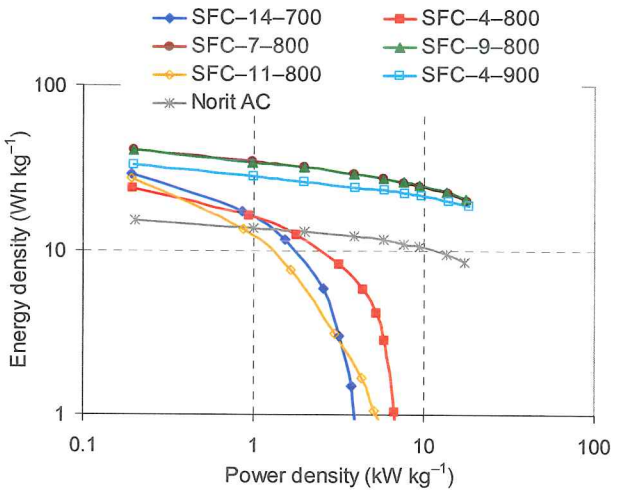

Figure 2–18 Ragone plots for the Cs salt-flux carbons in H_2SO_4.

stable double-layer structure than when the ions stack together quickly to form an unstable state at high current density.[116] In the low temperature carbonized (SFC–14–700) together with insufficiently activated (SFC–4–800 and SFC–11–800) samples, the duration for charge/discharge at 10 A g^{-1} was negligible with the large IR drop. This is probably because they do not have enough conductivity to transfer electrons at such fast rate. In addition, the calculation of specific capacitance for a single electrode was

conducted from their discharge charts (Fig. 2–16). As high as 298 F g^{-1} of specific capacitance could be achieved at the smallest current density in SFC–9–800, while retaining 65% of this capacitance (194 F g^{-1}) even at the highest current density. It should be noted that their capacitances were higher than the reference Norit AC. At 10 A g^{-1} for example, the capacitance for SFC–9–800 was about 2.3 times higher than that for Norit AC.

For further understanding of their capacitive behaviours, electrochemical impedance spectroscopy (EIS) tests were carried out. The Nyquist plots for the carbons are shown in Fig. 2–17. The chart for the higher capacitance carbons (SFC–7–800, SFC–9–800 and SFC–4–900) has three features. A nearly vertical line parallel to the imaginary axis in the lower frequency region indicates that the capacitance is mostly from EDL behaviour, a short length of 45° segment in the middle means fast diffusion of the ions into the bulk of the electrode particles, and a small semicircle in the higher frequency region is indicative of a small pseudocapacitive interaction and intrinsic resistance.[10,32] Deviation from these characteristics was observed in the other carbons, probably due to the lower conductivity along with the higher percentage of contribution from pseudocapacitance. The chart for Norit AC was similar to those for the higher capacitance carbons except for the slightly larger semicircle; the conductivity of Norit AC might be lower. The equivalent series resistance (ESR), as determined by the intersection of the Nyquist plot with the x-axis (real part of the impedance) does not vary significantly among the samples because it is largely related to the ionic conductivity of electrolyte.[115]

Plots of energy density over power density (Ragone plot) for a single carbon electrode in this study disclosed that the higher capacitance sample (SFC–7–800, SFC–9–800 and SFC–4–900) showed much higher energy density than Norit AC. For instance, 40.7 Wh kg^{-1} could be obtained in SFC–9–800, being 2.7 times higher than Norit AC (15.1 Wh kg^{-1}). This is attributed to the high specific surface area and heteroatom content together with the suitable micropore/total pore ratio. Thanks to the excellent properties

for the caesium salt-flux carbons in this study, the system already outperforms the one for lead-acid battery (PbO_2/Pb).

2.2.3. Electochemical properties for the salt-flux carbons in aqueous potassium hydroxide electrolyte

Next, the caesium salt-flux carbons were electrochemically examined in 6 mol L^{-1} aqueous potassium hydroxide (KOH), which is also frequently employed as electrolyte. The measurement method was the same as the last section, SFC–7–800, SFC–9–800 and SFC–4–900 which revealed to have high capacitance in H_2SO_4 being used as electrode in

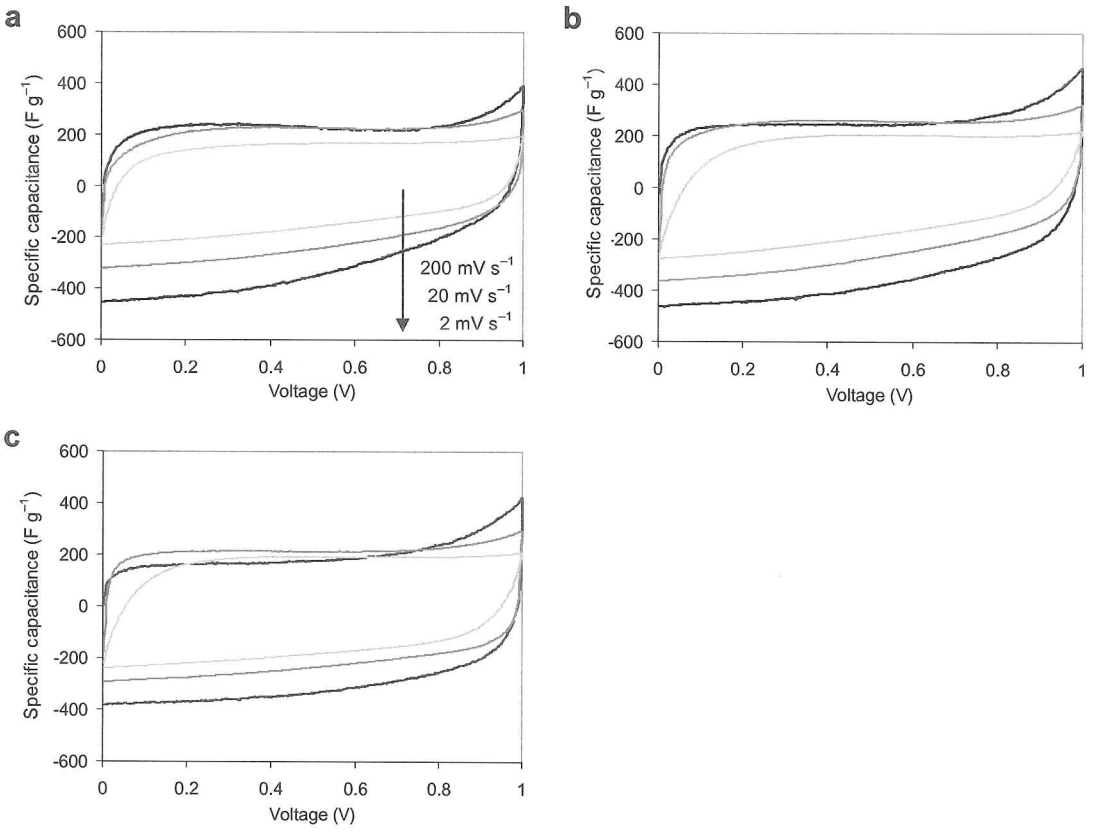

Figure 2–19 Cyclic voltammetry charts for the Cs salt-flux carbons in KOH at the sweep rate of 2, 20 and 200 mV s^{-1}.

a, SFC–7–800. **b**, SFC–9–800. **c**, SFC–4–900.

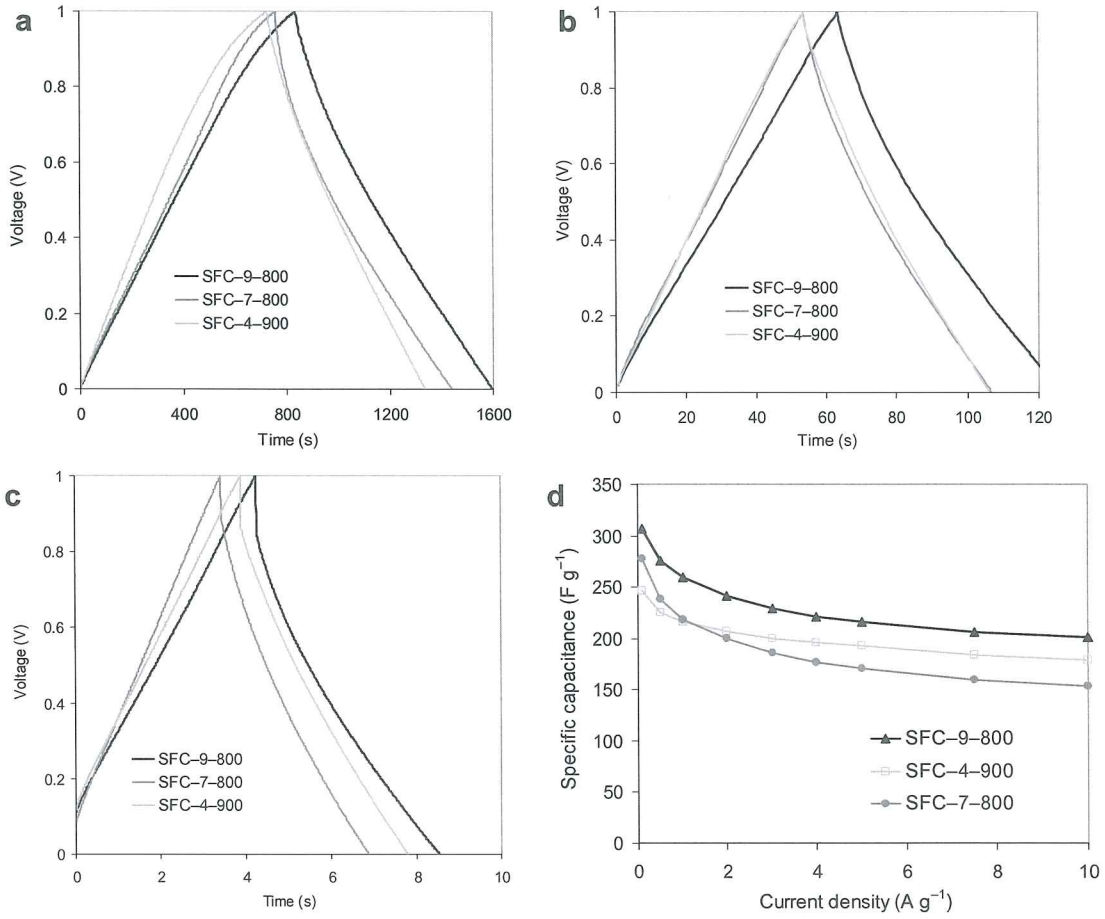

Figure 2–20 Galvanostatic charge/discharge profiles for the Cs salt-flux carbons in KOH. **a**, At 0.1 A g^{-1}. **b**, At 1 A g^{-1}. **c**, At 10 A g^{-1}. **d**, Relation of specific capacitance to current density calculated from the discharge curve.

this study. The electrochemical trends in KOH were found to be quite similar to the tests in H_2SO_4 described earlier. SFC–7–800 together with SFC–9–800 demonstrated more pseudocapacitive behaviour than SFC–4–900, which is clear from the more distorted CV shapes (Fig. 2–19) as well as the galvanostatic charge/discharge profiles with more significant curvatures (Fig. 2–20). This is probably because the higher heteroatom contents in the 800 °C carbonized samples. High capacitances were confirmed in each sample (Fig. 2–20), displaying 307 F g^{-1} in SFC–9–800 with the high capacitance retention (201 F g^{-1} at 10 A g^{-1}, 65% retention). Nyquist plots from the EIS measurement

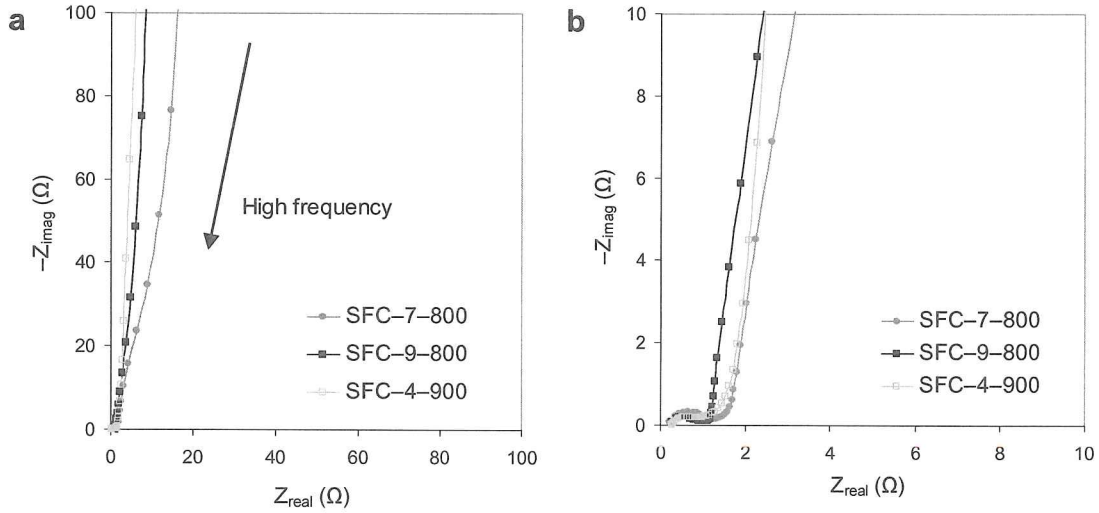

Figure 2–21 Nyquist plots for the Cs-salt flux carbons in KOH.

a, Plots for the Cs salt-flux carbons. **b**, A magnification of **a**.

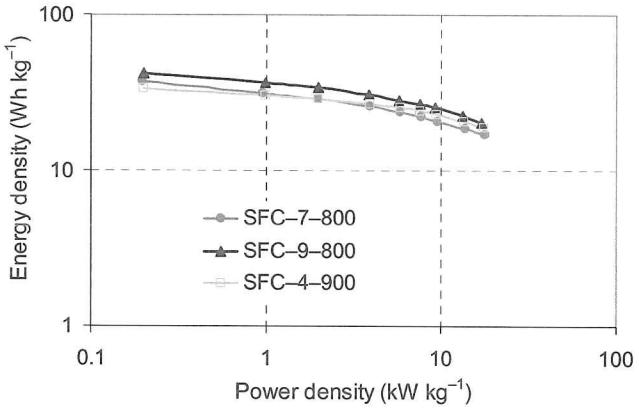

Figure 2–22 Ragone plots for the Cs-salt flux carbons in KOH.

(Fig. 2–21) exhibited the similar trends as the H_2SO_4 electrolyte, except that the size of semicircles was slightly larger than those in the H_2SO_4 electrolyte possibly due to the different pseudocapacitive mechanisms. Comparable energy density as in H_2SO_4 was achieved in KOH, 41.8 Wh kg^{-1} being obtained in SFC–9–800 (Fig. 2–22). SFC–9–800 had the highest energy density, but there was no significant difference among these three samples like in H_2SO_4.

Chapter 3

Enhancement of energy density from electrolyte: Application of salt-flux carbon particles to redox-active electrolytes

3.1. Introduction

Electrolyte, which resides inside the separator and the active material layers, is also one of the most important supercapacitor components. Properties such as high maximal operating voltage, high electrochemical stability, high ionic concentration, high conductivity and low solvated ionic radius, low viscosity, low volatility, low toxicity, low cost as well as availability at high purity are required for electrolyte of supercapacitor.[6] It can be classified into three types; aqueous electrolyte, organic electrolyte and ionic liquids (ILs).

Aqueous electrolytes such as H_2SO_4, KOH, Na_2SO_4, etc are capable of affording higher ionic concentrations and conductivities compared with organic electrolytes. Supercapacitor using aqueous electrolyte may display higher capacitance than those with other classes of electrolytes, probably due to higher ionic concentration and smaller ionic radius.[6] In addition, aqueous electrolytes can be prepared and utilized without strict control of the preparing conditions, while the other ones need rigid conditions to obtain ultra-pure electrolytes for preventing water contamination which results in the voltage reduction.[117] However, aqueous electrolytes have much lower maximal operating voltage (about 1.2 V) than those of other electrolytes, the measurement being usually conducted less than 1.0 V. Consequently, it has been accepted for a long time that the energy density of capacitors in aqueous electrolytes is much lower than in the other electrolytes. This is the reason why organic or IL electrolytes are often recommended.

Organic electrolytes can provide an operating voltage as high as 3.5 V, being about three times higher than conventional aqueous electrolytes. Acetonitrile together with propylene carbonate (PC) are the most commonly used solvents as organic

electrolytes, and organic salts such as tetraalkylammonium salts of tetrafluoroborate and hexafluorophosphate anions are used in supercapacitor electrolytes to provide mobile ions for transport to the electrode surface.[7] However, organic solvents do not meet the requirements of environmental compatibility and safety because organic solvents have inherent flammability and potential explosion risks due to the high vapour pressure. Another disadvantage of organic electrolytes is that they exhibit a significantly higher equivalent series resistance (ESR) (typical increase by a factor of 50–100 in comparison with aqueous electrolytes),[7] due to lower conductivity and higher viscosity. This has a detrimental effect on the power capability of the supercapacitor devices. However, the increased operating voltage compensates in part for the reduction in power density.[117]

Compared with aqueous and organic electrolytes, ILs (commonly defined as salts that melt below 100 °C[118]) are of advantage in terms of extremely low vapour pressure, low flammability, high thermal and chemical stability, wide electrochemical stability window ranging from 2 to 6 V, typically about 4.5 V, and conductivity at a level of *ca.* 10^{-2} S cm^{-1}.[6] Since there is no solvation shell in ILs due to a solvent-free system, they can offer a well identified ion size.[119] The main ILs studied for supercapacitor applications are imidazolium, pyridinium, pyrrolidinium, as well as asymmetric, aliphatic quaternary ammonium salts (Fig. 3–1) with anions such as tetrafluoroborate, trifluoromethanesulphonate, bis(trifluoromethanesulphonyl)imide, bis(fluorosulphonyl) imide or hexafluorophosphate.[28–30] The chemical/physical properties of these ILs strongly depend on the type of cation and anion. For example, aliphatic quaternary ammonium and pyrrolidinium salts display a wider potential range, sometimes exceeding 5 V, but their conductivity is generally lower than that of 1-ethyl-3-methylimidazolium-based ILs which remain liquid even in low temperature (< -50 °C) and show higher conductivities as high as 10^{-2} S cm^{-1} at room temperature.[29] However there are some disadvantages. ILs have relatively high viscosities and much lower ionic conductivities than aqueous electrolytes.[7] Not all ILs have particularly large voltage windows, some not being larger than an aqueous electrolyte. Operation at low temperatures may be difficult since many ILs have melting temperatures just above 273 K.[120] Some ILs,

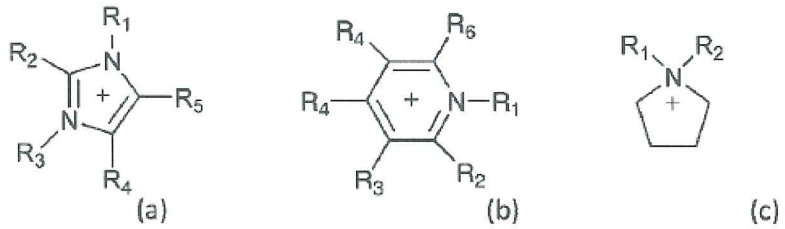

Figure 3–1 Structure of cations found in ionic liquids (ILs): (a) imidazolium, (b) pyridinium, (c) pyrrolidinium.[7]

notably those containing BF^{4-} and PF^{6-}, are known to produce hazardous hydrofluoric acid. ILs are hygroscopic which reduces the operating potential range, and have to be handled in an inert atmosphere. A major disadvantage of using ILs is their high cost, although larger scale production and alternative synthetic approaches may reduce the price in the future.

In addition to the attempts above, a new strategy through redox-active electrolytes has been recently reported. Introducing redox mediators into conventional electrolytes can lead to enormous capacitive contributions for supercapacitor systems through the reversible Faradaic reactions of the redox mediators. Roldan *et al.*[22,31] reported a novel acidic electrolyte with hydroquinone (HQ)-loaded H_2SO_4 aqueous solution, which enhanced the specific capacitance of the supercapacitors by about three folds compared to the electrolyte without HQ. The synergistic pseudocapacitive effects of Cu^{2+} and Fe^{2+} ions in porous carbon electrodes in a H_2SO_4 electrolyte system were investigated by Li *et al.*;[121] the capacity of carbon electrode reached 223 mAh g^{-1}, which was much higher than that of their H_2SO_4 system in the same conditions. Lota *et al.* disclosed that iodide aqueous solution contributed to obtain about two times higher capacitance than 1 mol L^{-1} H_2SO_4 aqueous solution,[33] because of interesting redox reaction of iodide benefiting from rich oxidation states from the most stable iodide (–1) to iodate (+5). In addition to

these examples, *p*-phenylenediamine,[35] methylene blue,[34] indigo carmine,[122] etc were loaded into conventional aqueous electrolytes, showing better capacitances.

In this chapter, the possibility for further enhancement of energy density using the caesium salt-flux carbons was investigated in redox-active aqueous electrolytes, by which the advantage of aqueous electrolyte, such as low price, low viscosity, high conductivity and safety can be utilized. The energy density could be enhanced about three folds in comparison with 1 mol L^{-1} aqueous sulphuric acid.

3.2. Results and discussion

3.2.1. Application of redox-active aqueous electrolytes to the salt-flux carbons

The influence of redox-active electrolytes on supercapacitor properties using the salt-flux carbon SFC–9–800 as electrode, which was disclosed to have the highest capacitance in the last chapter, was studied with a two-electrode Swagelok® type cell. 0.38 mol L^{-1} hydroquinone dissolved in 1 mol L^{-1} H_2SO_4 aqueous solution (HQ/H_2SO_4), 0.5 mol L^{-1} copper (II) sulphate and 0.5 mol L^{-1} iron (II) sulphate dissolved in 1 mol L^{-1} H_2SO_4 aqueous solution ($Cu/Fe/H_2SO_4$) and 1 mol L^{-1} potassium iodide aqueous solution (KI) were employed as redox-active electrolytes in this study and compared to the conventional 1 mol L^{-1} H_2SO_4 electrolyte (H_2SO_4). The measurement methods were the same as Chapter 2.

As expected, their CV charts had considerable shape deviations from the result for H_2SO_4 (Fig. 3–2); outstanding peaks that are sets of anodic and cathodic peaks were seen in HQ/H_2SO_4 along with $Cu/Fe/H_2SO_4$ especially at 2 mV s^{-1}, indicating the distinct redox behaviour. Pseudocapacitive peaks did not stand out at the highest sweep rate of 200 mV s^{-1}, but still create deviation from the shape of typical EDL capacitance. This is probably the consequence of the slower kinetics of the redox reactions with respect to the

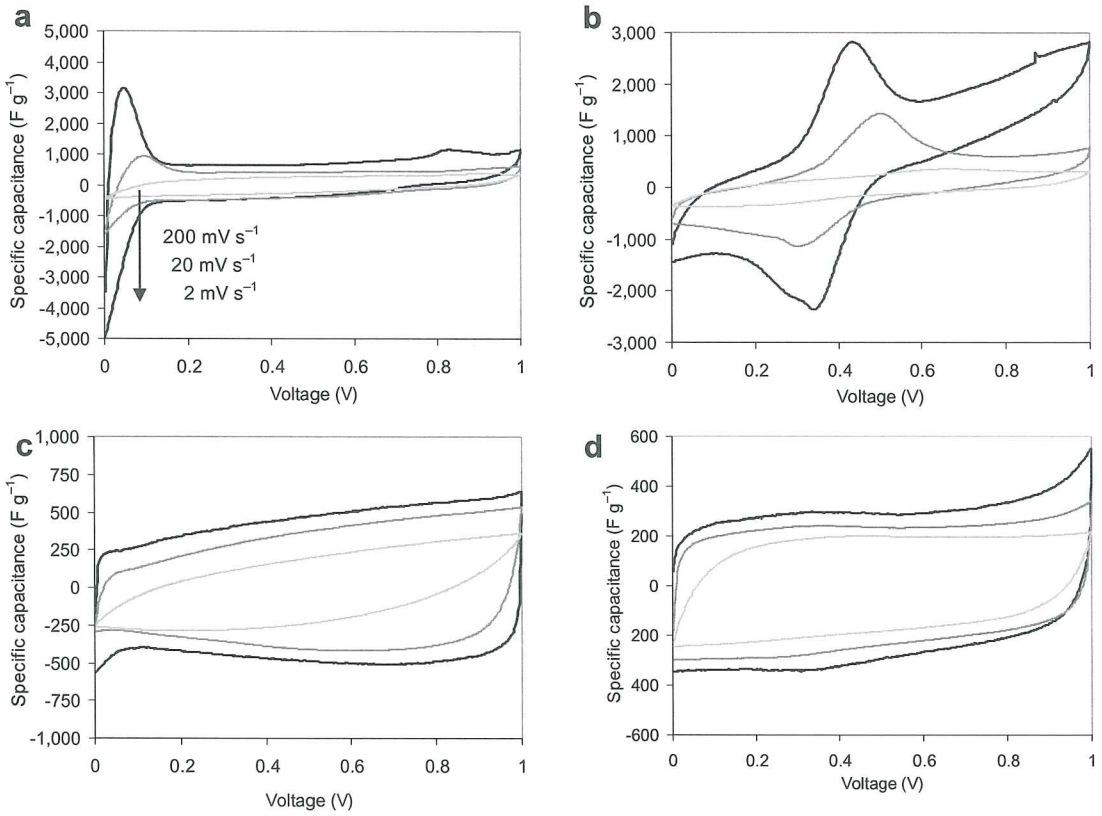

Figure 3–2 Cyclic voltammetry charts for SFC–9–800 in redox-active electrolytes at the sweep rate of 2, 20 and 200 mV s^{-1}.

a, In 0.38 mol L^{-1} hydroquinone dissolved in 1 mol L^{-1} H_2SO_4 aqueous solution (HQ/H_2SO_4). **b**, In 0.5 mol L^{-1} copper (II) sulphate and 0.5 mol L^{-1} iron (II) sulphate dissolved in 1 mol L^{-1} H_2SO_4 aqueous solution ($Cu/Fe/H_2SO_4$). **c**, In 1 mol L^{-1} potassium iodide aqueous solution (KI). **d**, In 1 mol L^{-1} H_2SO_4 aqueous solution (H_2SO_4) for comparison (the same as Fig. 2–15**e**). Note that the amplitude for y-axis is different in each figure.

scan rate. Smaller humps were detected in the experiment with the KI electrolyte at about 0 and 0.8 V for cathodic scan, but they were not so outstanding compared to the other redox-active electrolytes. It should be emphasized that the capacitance was much higher than H_2SO_4 in all the redox-active electrolytes.

Their galvanostaic charge/discharge profiles also displayed the pseudocapacitive behaviours with considerable curvatures (Fig. 3–3), most of which demonstrating the

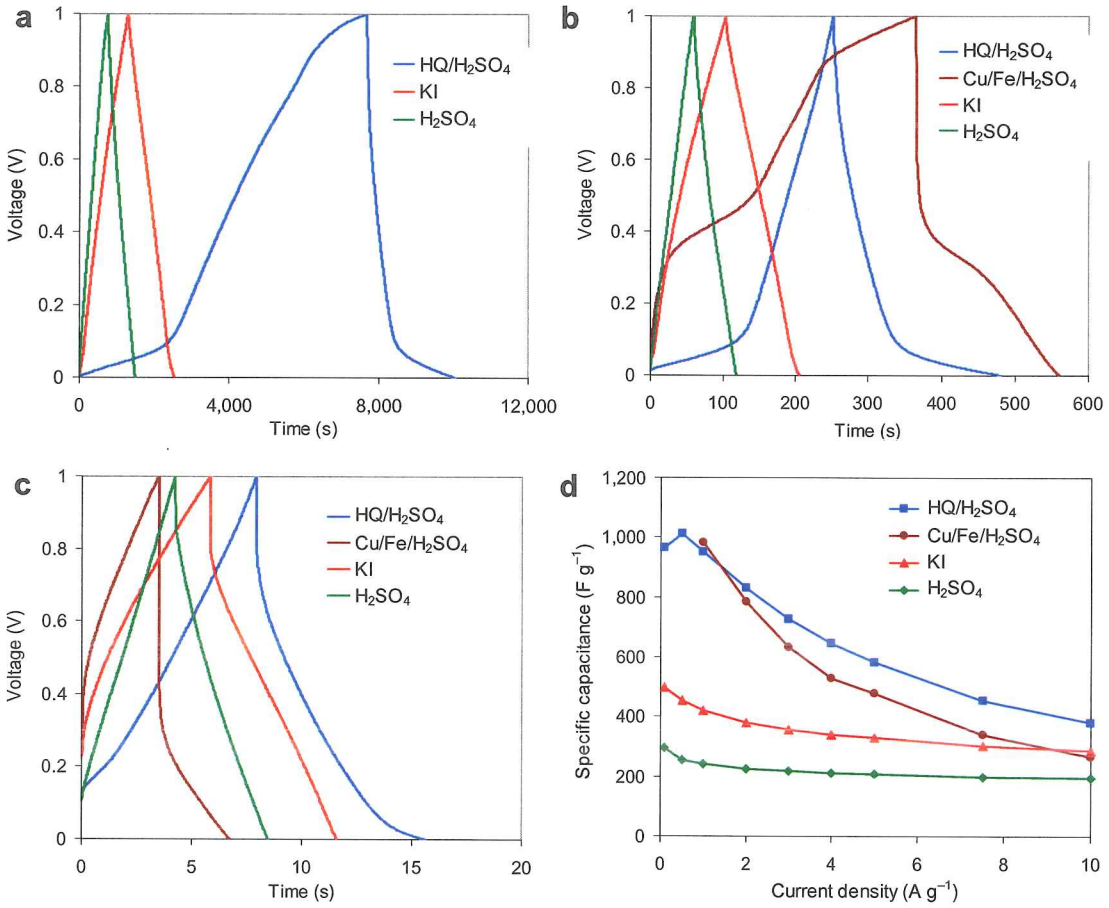

Figure 3–3 Galvanostatic charge/discharge profiles for SFC–9–800 in redox-active electrolytes.

a, A chart for 0.1 A g^{-1}. **b**, A chart for 1 A g^{-1}. **c**, A chart for 10 A g^{-1}. **d**, Relation of specific capacitance to current density calculated from the discharge curves. Note that the property in the Cu/Fe/H_2SO_4 electrolyte at 0.1 A g^{-1} could not be measured.

superior capacitive properties compared to H_2SO_4. Plateaus characteristic of redox reactions were observed the voltages of which correspond very well to the position of the CV peaks: for example, in the 0–0.1 V range for HQ/H_2SO_4 and in the 0.3–0.5 V range for Cu/Fe/H_2SO_4. KI showed nearly linear charge/discharge charts like H_2SO_4 that agrees well to the CV chart.

The specific capacitance calculated from the discharge profiles for a single electrode (Fig. 3–3) revealed that as high as 1015 F g^{-1} could be achieved at 0.5 A g^{-1} in HQ/H_2SO_4 along with 985 F g^{-1} at 1 A g^{-1} in $Cu/Fe/H_2SO_4$. This is the first example in which over 1000 F g^{-1} was obtained with such a simple carbon-based redox electrode to the best of the author's knowledge; this capacitance is comparable to metal oxide and conductive polymer systems.[4] It should be emphasized that even at 10 A g^{-1}, as high as 400 F g^{-1} was achieved in HQ/H_2SO_4, being the highest capacitance in this study at that rate; however, the capacitance is more current density dependent in the presence of HQ along with metal cations (Cu^{2+} and Fe^{2+}) as a consequence of the involved kinetics of the redox reactions which simply take longer than the readjustment of the electric double layer.[31] Hence, this leads to increase of Faradaic contribution at lower current densities. Furthermore, the specific capacitance at 0.1 A g^{-1} was somewhat lower than that at 0.5 A g^{-1} in HQ/H_2SO_4, and the measurements at 0.1 and 0.5 A g^{-1} could not be conducted in $Cu/Fe/H_2SO_4$; the voltages could not be reached to 1 V even after four hours of the charging processes, the voltages not going over 0.35 V in 0.1 A g^{-1} and 0.87 V in 0.5 A g^{-1}. These are probably due to influence of the onset of diffusive self-discharge. When a real, not an ideal, supercapacitor is charged and then left on open circuit for some time, a certain degree of self-discharge can set in;[41] an electrochemical capacitor in a charged state is in a state of high positive free energy relative to that in a discharged state. There is a virtual driving force that tends to discharge it.[122] The experiments using the KI electrolyte also showed capacitance improvement and less current density dependence than HQ/H_2SO_4, which was similar to H_2SO_4. The capacitance at 0.1 A g^{-1} was 498 F g^{-1}, about 1.5 times higher than H_2SO_4, 57% of capacitance being retained which is comparable to H_2SO_4 (65%). This finding allows for expanding the choice of current collector because KI, a neutral electrolyte, does not afford any damage to the current collector as such.

All the impedance spectra (Fig. 3–4) in redox-active electrolytes revealed slight deviation from the vertical line for the lower frequency region in comparison with H_2SO_4, suggesting the increase of pseudocapacitive contribution. In addition, their size for

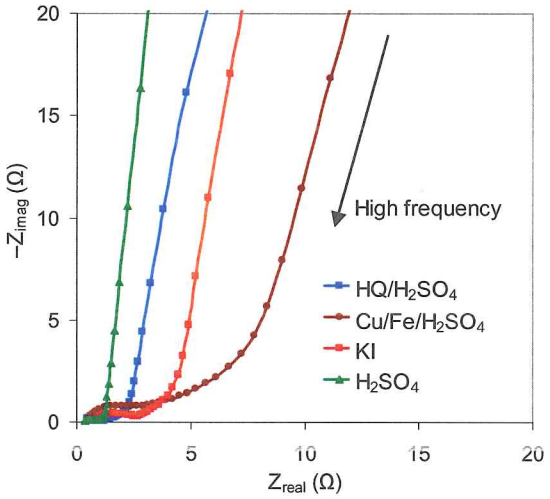

Figure 3–4 Nyquist plots for SFC–9–800 in redox-active electrolytes.

semicircles was larger and their 45° segment in the middle frequency was longer, indicating slow kinetics of the pseudocapacitive behaviour.

The mechanism for these pseudocapacitive behaviours could be considered as follows:

- As to the HQ/H_2SO_4 system, it is suggested that Faradaic reactions of hydroquinone occur in the positive electrode while hydrogen evolution or adsorption phenomena could occur in the negative electrode. As the *p*-benzoquinone (Q) / hydroquinone (HQ) reaction is an inner-sphere electron transfer process, the heterogeneous electron-transfer kinetics of this couple is also strongly influenced by the surface characteristics of the electrode.[123] These redox reactions are represented in Scheme 3–1. For the present study, *i.e.*, an unbuffered media with $[H^+] > [Q]$, the Q/HQ reactions involve steps comprising $2H^+$ and $2e^-$. However, these reactions are an oversimplification of an in reality very complex mechanism.[124]

Scheme 3–1 Redox reactions in the HQ/H_2SO_4 electrolyte.[31]

(1) *p*-Benzoquinone (Q) redox reactions in unbuffered media with $[H^+] > [Q]$. (2) Hydrogen evolution reaction in acidic medium. (3) Adsorption of nascent hydrogen on the surface of the carbon material.

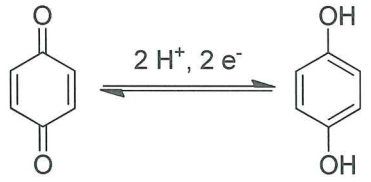

p-Benzoquinone Hydroquinone (1)

$$H_3O^+ + e^- \rightarrow H + H_2O \quad (2)$$

$$C + H \rightarrow CH_{(adsorb)} \quad (3)$$

- In the Cu/Fe/H_2SO_4 system, a synergistic electrochemical interaction is suggested to occur between Cu^{2+} and Fe^{2+} ions in the following pseudocapcaitive mechanism;[121]

$$Fe^{2+} + Cu \rightleftharpoons Fe^{3+} + Cu^{2+} + 3\ e^-$$

$$x\ Fe^{3+} + y\ Cu^{2+} + z\ C + (x+2y)\ e^- \rightleftharpoons (Fe_xCu_y)^{2x+}{}_{(adsorb)}Cz$$

The introduction of Cu^{2+} ions into electrolyte increases the capacitance due to the electrochemical redox reactions as shown below;

$$Cu^{2+}{}_{(aq)} + e^- \rightleftharpoons Cu^{+}{}_{(adsorb)}$$

$$Cu^{+}{}_{(adsorb)} + e^- \rightleftharpoons Cu_{(deposit)}$$

However, the capacitive process does not have enough stability because of the poor reversibility of the redox reactions between Cu^{2+}/Cu on the surface of porous carbon electrodes. Nevertheless, the addition of Fe^{2+} ions into the Cu(II)-containing electrolytes affords a higher and more stable capacitance.[33] This is attributed to the synergistic effects observed between Fe^{3+}/Fe^{2+} and Cu^{2+}/Cu ions

that achieved a novel electrochemical redox capacitive process. It is proposed that the synergistic effects accounting for the much improved reversibility of Cu^{2+}/Cu electrochemical redox reactions arose from the formation of complexes between the $(Fe_xCu_y)^{2x+}$ adions and the edge site carbon atoms of the porous carbon electrodes. For confirming this synergistic effect, the CV chart for 0.5 mol L^{-1} copper (II) sulphate dissolved in 1 mol L^{-1} H_2SO_4 aqueous solution (Cu/H_2SO_4) as electrolyte was also recorded and compared with the result for $Cu/Fe/H_2SO_4$ (Fig. 3–5). It was found that the capacitance was much less than that for $Cu/Fe/H_2SO_4$, although certain extent of improvement was confirmed compared to H_2SO_4.

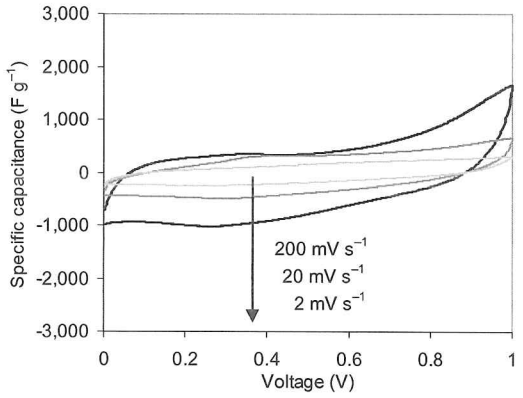

Figure 3–5 Cyclic voltammetry charts for SFC–9–800 in 0.5 mol L^{-1} copper (II) sulphate dissolved in 1 mol L^{-1} H_2SO_4 aqueous solution (Cu/H_2SO_4) as electrolyte at the sweep rate of 2, 20 and 200 mV s^{-1}.

- The electrochemical activity of the KI electrolyte is based on equations below:[47]

$$3\ I^- \rightleftharpoons I_3^- + 2\ e^-$$

$$2\ I^- \rightleftharpoons I_2 + 2\ e^-$$

$$2\ I_3^- \rightleftharpoons 3\ I_2 + 2\ e^-$$

$$I_2 + 6\ H_2O \rightleftharpoons 2\ IO_3^- + 12\ H^+ + 10\ e^-$$

These reactions occur on the electrode/electrolyte interface, and a suitable porosity is a crucial factor from this point of view. Iodine, even though it exists as a solid and/or volatile element, it easily dissolves here forming I_3^- complex. It suggests that the movement of both cations and anions is not disturbed by any additional interaction and they can easily penetrate the porous structure of the carbon electrode. These species are assumed to be adsorbed in the micropores due to the low ion–water potential, giving a typical electrostatic energy storage response besides the redox reactions.[33] This should be the reason why the CV charts had quasi-rectangular shapes in comparison with other redox-active electrolytes.

3.2.2. Energy density of the salt-flux carbons in redox-active aqueous electrolytes

Energy and power density for a single electrode were calculated based on the discharge curve, and the Ragone plot was displayed in Fig. 3–6; a set of the salt-flux carbon (SFC–9–800) and the redox-active aqueous electrolytes demonstrated excellent properties. As high as 133.0 Wh kg^{-1} could be achieved with HQ/H_2SO_4; this is well above the properties for nickel metal hydride battery (Ni/MH), slowly reaching LIB. All the electrolytes showed relatively horizontal lines in Fig. 3–6a except for $Cu/Fe/H_2SO_4$ which had a severe energy density drop at the higher power density region owing to the significant IR drops. For further understanding superiority of the HQ/H_2SO_4 system in this study by comparing with other energy storage devices, the Ragone plot for a whole supercapacitor cell was also performed onto Fig. 1–1 (Fig. 3–6b).[1]

The long-term cycling behaviour is also one of the most important properties for supercapacitor, which was examined at constant currents of 2 and 10 A g^{-1} (Fig. 3–7). The salt-flux based carbon exhibited excellent stabilities in all the electrolytes investigated except for $Cu/Fe/H_2SO_4$; more than 85% of energy density was retained even

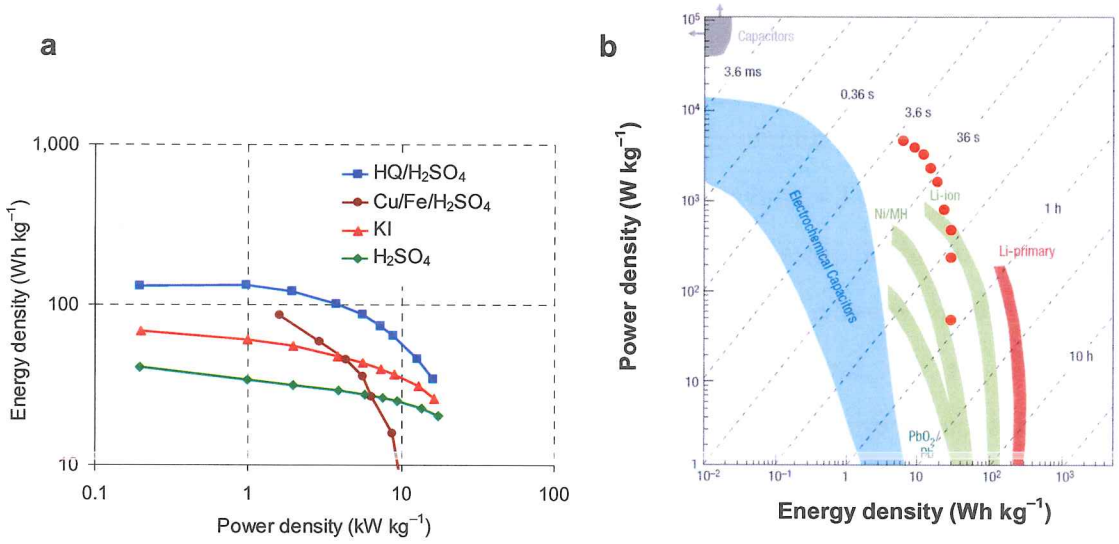

Figure 3–6 Ragone plots for SFC–9–800 in redox-active electrolytes.

a, Plots for this study. **b**, The same figure as Fig. 1–1 onto which the result for HQ/H_2SO_4 was approximately overwritten. Note that the values for energy and power density are based on a single electrode in **a**, and on a whole cell in **b**.

after the 2500 cycle (2 A g^{-1}) or 10000 cycle (10 A g^{-1}) measurement. The test with H_2SO_4 showed superior stability, showing the 94% (at 2 A g^{-1}) and 85% (at 10 A g^{-1}) energy density retention. In HQ/H_2SO_4, the energy density at 2 A g^{-1} went up to the maximum (107.4 Wh kg^{-1}) on the way, following the gradual decrease until 2500 cycles; nevertheless, the energy density for the last cycle still had a high value (93.9 Wh kg^{-1}). This might be attributed to local modification of the redox system. An outstanding decrease in energy density was seen at the beginning of the 10 A g^{-1} test, but the energy density after the 10000 cycles was still as high as 31.7 Wh kg^{-1}. It should be emphasized that the long-term cycling behaviour is superior to all that of batteries.[2] The experiments with the KI electrolyte experienced a gradual increase of the energy density in both constant currents: 60.0 Wh kg^{-1} at 2 A g^{-1} together with 24.3 Wh kg^{-1} at 10 A g^{-1} after the tests. This anomalous increase of capacitance was also observed in literature,[33] a mutual shift of operating potentials for both electrodes during cycling being suggested to

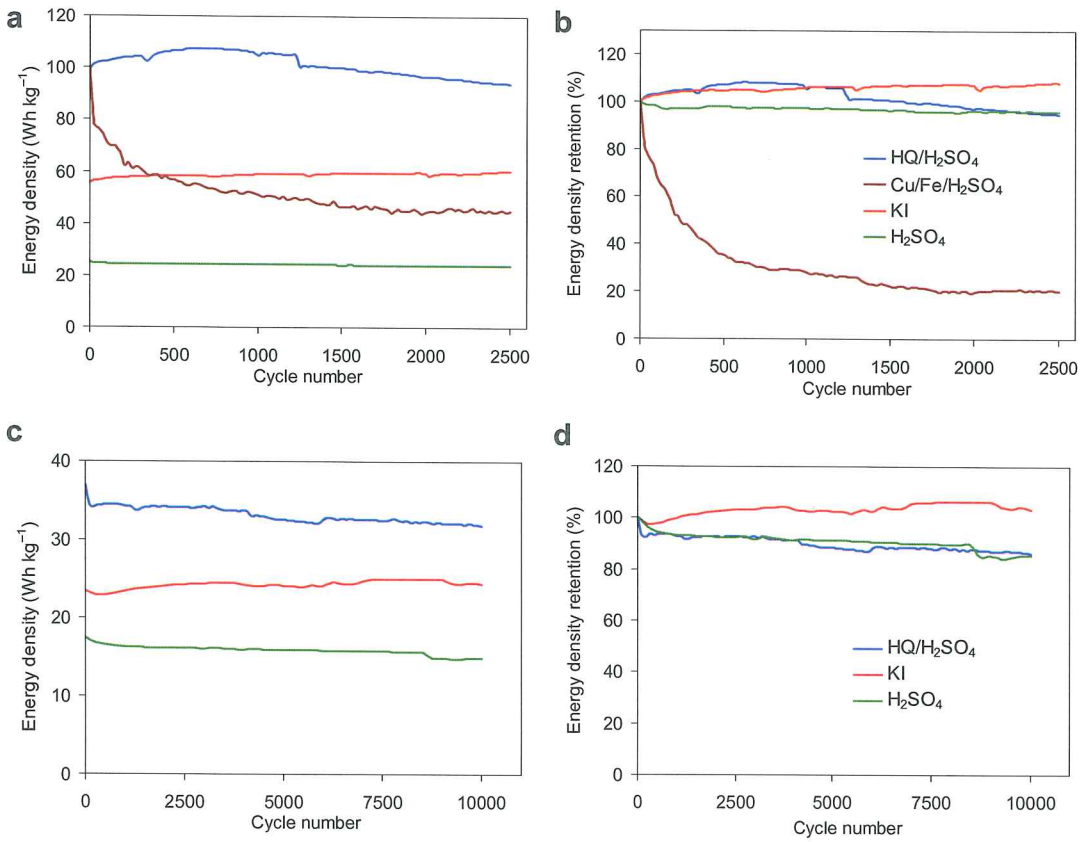

Figure 3–7 Cycle stability tests for SFC–9–800 in redox-active electrolytes.

a, Relation of energy density to cycle number at 2 A g^{-1}. **b**, Relation of energy density retention to cycle number at 2 A g^{-1}. **c,** Relation of energy density to cycle number at 10 A g^{-1}. **d**, Relation of energy density retention to cycle number at 10 A g^{-1}. Note that the test in Cu/Fe/H_2SO_4 at 10 A g^{-1} was not conducted because of the lower capacitance than H_2SO_4.

result in this profitable effect. A gradual modification of the carbon material by iodine as well as a reduction of iodine on carbon during the long-term cycling could be also considered. On the other hand, a significant property aggravation was observed in Cu/Fe/H_2SO_4 at 2 A g^{-1}. Nevertheless, it should be noted that some improvement was confirmed in comparison with Cu/H_2SO_4; in Cu/H_2SO_4, the energy density after 1,250 cycles at 2 A g^{-1} was as small as 6.2 Wh kg^{-1} with only 19% retention. This indicates that influence of copper metal deposition is to some extent diminished by introducing

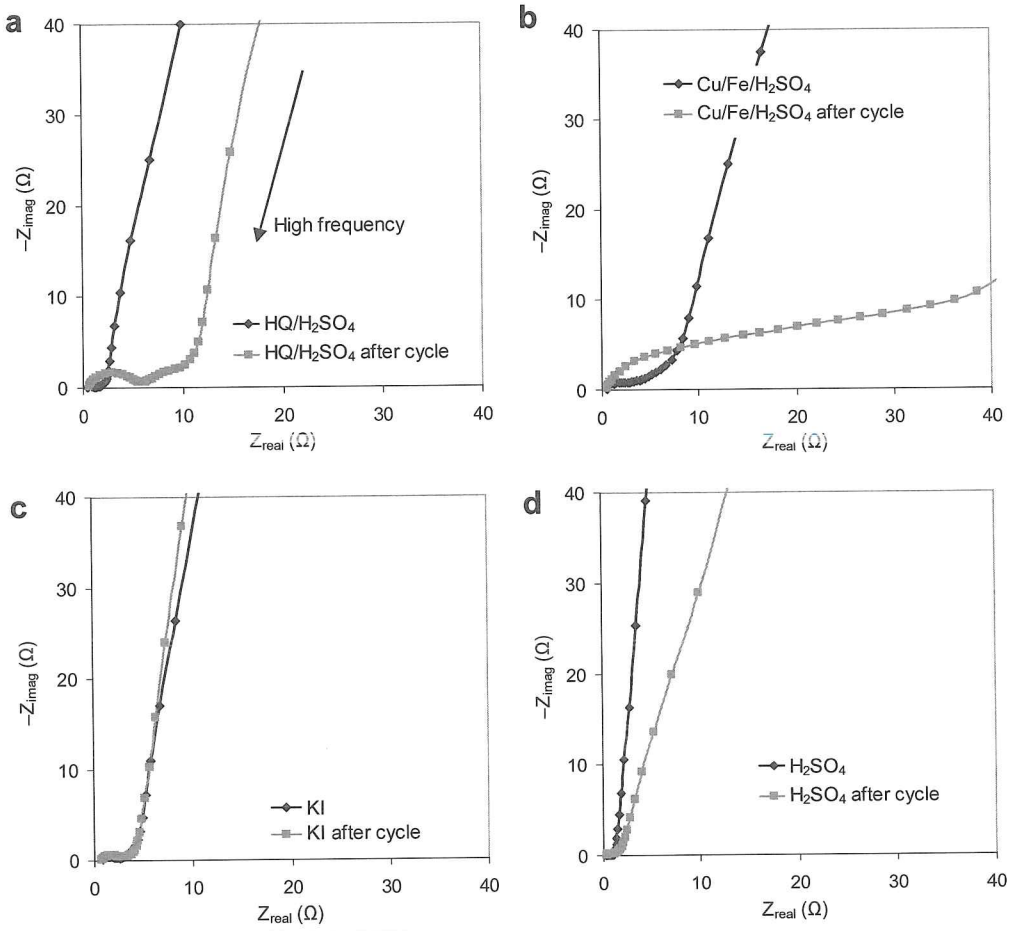

Figure 3–8 Nyquist plots for before and after the cycle stability test (2500 times at 2 A g^{-1}) of SFC–9.

a, In 0.38 mol L^{-1} hydroquinone dissolved in 1 mol L^{-1} H_2SO_4 aqueous solution (HQ/H_2SO_4). **b**, In 0.5 mol L^{-1} copper (II) sulphate and 0.5 mol L^{-1} iron (II) sulphate dissolved in 1 mol L^{-1} H_2SO_4 aqueous solution (Cu/Fe/H_2SO_4). **c**, In 1 mol L^{-1} potassium iodide aqueous solution (KI). **d**, In 1 mol L^{-1} H_2SO_4 aqueous solution (H_2SO_4).

Fe^{2+} in the cycle test. The test of Cu/Fe/H_2SO_4 at 10 A g^{-1} was not conducted owing to the lower capacitance than H_2SO_4.

Fig. 3–8 depicts the Nyquist plots for before and after the 2500 times cycle stability test at 2 A g^{-1} in the redox-active electrolytes. There was little difference in the

charts for before and after the cycle stability test in the KI electrolyte, which might be one of the reasons for the best cycle stability performance. Certain extent of deviation was confirmed in the other electrolytes; the size of semicircles became larger and the 45° segment in the middle frequency region got longer. This is probably due to deterioration of the electrodes in the course of the test by swelling and contracting.

Chapter 4

Conductive carbon films using acrodam oligomer by solution process

4.1. Introduction

Carbon films having three-dimensional network are industrially versatile as well as carbon particles described in the last chapters. Benefiting from its hardness, chemical inertness, low friction coefficient, high refractive index, high thermal and electrical conductivity,[125–127] carbon films have widespread applications as protective coatings for optical windows, automobile parts, biomedical coatings, computer hard disks and micro-electrochemical devices (MEMs).[125,128,129] Besides, they have also been used for food and beverage packaging purposes due to their attractive gas barrier properties,[130] some of them having already been widely commercialized.[126] Furthermore, introduction of porous structure into the film enables to expand the application field to supercapacitors, fuel cells, sensors, gas separations, membrane reactors, ultrafiltrations, and many more.[51,125] The attraction of three-dimensional networks lies in the essential absence of contact resistance within the network. In contrast, for particles as the filler a contact resistance exists between adjacent particles even if the particles touch one another, and the polymer matrix separating the adjacent particles gives rise to additional resistance.[132] In addition, due to the fact that the polymer matrix does not have to be included in the three-dimensional film in principle, the carbon properties can be utilized at the maximum and additional production processes are not needed, which is of advantage in industrial application.

It is known that the practical performance of the carbon films is strongly dependent on the proportion of sp^3 and sp^2 hybridizations and also on the hydrogen content.[133] To date, there are several categories of carbon films shown in Fig. 4–1. The outermost *s* and *p* orbitals of carbon atoms form π and σ bonds in sp^2 hybridizations and only σ bonds in sp^3 hybridizations. The π-bond existing only in sp^2 hybridizations is

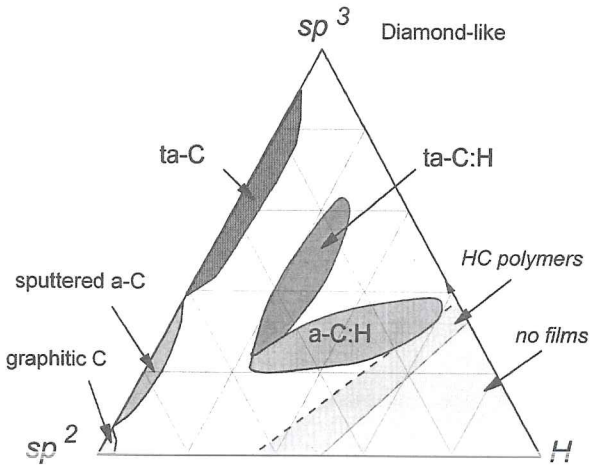

Figure 4–1 Ternary phase diagram of carbons.

The three corners correspond to diamond, graphite and hydrocarbons, respectively.[134]

weaker than the σ-bond. It is recognized that σ bonds influence the mechanical properties, while π bonds are mainly responsible for the electrical and optical properties.[125,135] The high hardness of carbon films is closely related to the sp^3 content, with higher sp^3 contents usually correlating with better film protection.[136,137]

Nitrogen atoms substituting carbon atoms in the graphite matrix are electron donors and promote *n*-type conductivity.[138] Doping with nitrogen has a significant effect on the structure of the carbon material. Another characteristic property of nitrogen-doped materials is the formation of a more defective structure of the carbon layers. Quantum chemical calculations revealed that incorporation of nitrogen atoms into a graphite-like lattice promotes the formation of pentagons facilitating distortion of the graphite layer.[139] For example, the structure of nitrogen-containing carbon (CN_x) films prepared by magnetron spraying of a graphite target in the Ar/N_2 discharge was studied for understanding relation with the nitrogen concentration in the film ([N]).[140] At [N] < 5 at% the film had a graphite-like structure. Meanwhile, at [N] > 15 at% a fullerene-like phase was formed. A transition region was observed at 5 at% < [N] < 15 at%. It was also reported that the conductivity of CN_x films did not have a linear relation with the nitrogen content; it had a maximum at [N] = 10.4 at%, decreasing at higher nitrogen

concentrations.[127] This effect was explained by the formation of an insulating phase at high nitrogen concentration in the film. This result suggests that there could be an interrelation among the nitrogen concentration in the N-doped carbon material, the material structure and its electrical properties.

For fabricating carbon three-dimensional films, vapour process such as physical vapour deposition (PVD) and chemical vapour deposition (CVD) is mostly employed to date;[141] sputtering,[142] pulsed laser deposition,[143] electron cyclotron resonance,[144] filtered cathodic vacuum arc process[145,146] and plasma enhanced chemical vapour deposition[147,148] are some of the examples. PVD and CVD techniques are used to produce thin and ultra-thin coatings (about 10 μm down to nanometre thickness) of inorganic elements (metals, semiconductors) and compounds (ceramics) as well as carbon and some organic compounds.[149] PVD coating requires vaporization of a solid material, that is target. CVD coating starts from mixtures of reactive gases (precursors) which are decomposed thermally or by plasma activation. In contrast to CVD techniques, the PVD processes are generally characterized by lower coating temperatures, larger numbers of possible coating and workpiece (substrate) materials, the higher purity of the deposited coatings and a better environmental compatibility of the manufacturing process. To reduce the coating temperature in CVD techniques, plasma enhancing (PECVD) is applied during the film deposition. Furthermore, the plasma polymerization technique allows the organic thin film deposition (polymers) from gaseous or liquid monomers. The vaporized atoms, ions and clusters can undergo chemical reactions with atoms from the process gas atmosphere before they are deposited on the substrate surface.[149]

The vapour process is a reliable method benefiting from the vast number of examples, but their high costs originating from the expensive parts such as high-vacuum pumps limit their industrial applications. Besides, the fabrication system becomes complicated, and/or the hazardous precursors have to be employed for introducing other elements such as nitrogen, boron, phosphor and metals.[150–156] In solution processes on the contrary, incorporation of other elements can be relatively easily performed by either of two ways in principle: preparing the carbon precursor bearing other elements, or using

mixture of the carbon precursor and the other elements-containing precursor(s). In addition, large-area fabrication at one time is possible because the coating can be done under ambient atmosphere.

Solution process techniques are exemplified by spin coating, doctor blading, ink jet printing, spray coating, etc,[157] spin coating being one of the predominant techniques employed to produce uniform thin films with thickness of the order of micrometres and nanometres.[158] This process has been widely used in the manufacture of integrated circuits, optical mirrors, colour television screens and magnetic disk for data storage.[159,160] In spin coating, centrifugal force drives the liquid outward. The viscous force and surface tension causes a thin residual film to be retained on the flat substrate. The film thins by the combination of outward fluid flow and evaporation.[161] Spin coating film deposition is a four step process, as illustrated in Fig. 4–2:[162]

1) Solution pouring: The material dissolved in a volatile solvent is poured by dripping on the centre of a rotating substrate.
2) Spin-up: While the substrate spins, the liquid flows radially driven by the centrifugal force.
3) Spin-off: Liquid that reaches the substrate edge is expelled in drops. As the film becomes thinner, the elimination rate of excess fluid decreases due to the increase of the viscosity with the solvent evaporation and of the flow resistance.
4) Evaporation: Evaporation occurs at all times from the beginning of the spin-coating process. However, when spin-off is slow and for less volatile solvents, the evaporation becomes the main mechanism of solvent removal and thinning of the film.

The resulting thickness, morphology and surface topography are known to depend highly on rotational speed, viscosity, volatility, diffusivity, molecular weight and concentration of the solutes.[158] They depend relatively little on the amount of solution deposited, the rate of deposition and the spinning time. Deposition by spin coating

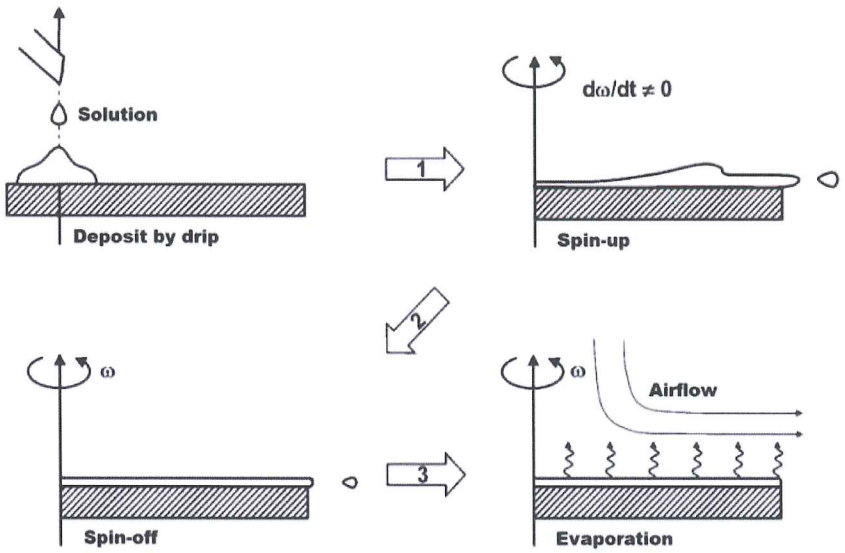

Figure 4–2 Stages of thin film deposition by spin coating.[162]

produces films with uniform thickness if the viscosity is homogeneous everywhere on the substrate and is independent of the sliding force. The uniformity of the film thickness results from the balance of two opposite main forces: the centrifugal and the viscous forces. During spin-up, the centrifugal force overcomes the gravitational force and the rapid thinning of the film exceeds all non-centrifugal inertial forces. When the film becomes very thin and viscous, the thickness continues to decrease but now controlled by evaporation. Rotation of the substrate with constant speed causes uniform evaporation of the solvent and, consequently, thickness of the film also becomes uniform.

In spite of the inherent versatility of solution process, their examples for fabricating carbon three-dimensional films are still limited. A porous carbon three-dimensional film was fabricated using a phenolic resol and Pluronic® F127 block copolymer as carbon precursor and template, which could be employed as supercapacitor electrode with 700 $m^2\ g^{-1}$ of the specific surface area and 136 F g^{-1} of the specific capacitance at 0.5 A g^{-1}.[51] Other examples using graphene oxide (GO),[163] carbon nanotube (CNT),[164] formaldehyde resin,[165–167] sucrose,[168] polyacrylonitrile (PAN)[166]

and nitrogen-containing photoresist[169] are disclosed so far. However, only some of them described the conductivities and/or the porous film fabrication which are important for supercapacitor electrode. A conductivity of about 3000 S cm^{-1} is reported with a CNT-based film,[164] but CNT is originally too expensive to expand the industrial application fields. A GO-based film exhibited 10^{+3} Ω sq^{-1} at 80% transmittance, but hazardous hydrogen fluoride has to be used for reduction, as is mostly the case with GO materials.[163] A porous carbon film with 3 nm uniform pore size and the high conductivity of 23 S cm^{-1} could be obtained using an inexpensive phenolic resol precursor.[167] Nevertheless, the number of inexpensive carbon precursors for solution process is still rather limited. Therefore, seeking suitable carbon precursors for solution process which can be industrially applicable is required.

In order to develop a new system for solution process, the precursor should have a high carbonization yield together with good solubility to solvents. The high carbonization yield facilitates to obtain a crack-free film with enough thickness. In the precursor with a low carbonization yield, the film experiences a drastic volume decrease during thermal treatment, resulting in the accumulation of internal stress. When the film has significant internal stress, it can be released with generation of crack and/or peeling off which are fatal to the film. A rigid structure with long conjugation chains is preferable for obtaining high carbonization yield,[170,171] but it has to compromise with the solubility. Not all the solvents which dissolve the precursor can be applied to solution process; suitable vapour pressure for the applied solution process and wettability to the substrate have to be considered.

In this chapter, the oligomer of acrodam[37,38] was examined as a proof-of-concept study for application to supercapacitor electrode using solution process. The reasons why this material is employed are as follows, in addition to those stated in the section 1.1:

- The oligomer which can be prepared via consecutive addition of acrodam is known to be dissolved in solvents such as tetrahydrofuran (THF) and acetone;[37] this could facilitate finding a suitable solvent system.
- The 800 °C carbonized particle is reported to have a high conductivity of 0.06 S cm^{-1};[38] therefore, a further higher conductivity is expected due to the essential absence of contact resistance if fabricated.
- The possibility for carbon film fabrication using acrodam system is referred;[38] nevertheless; there is no example of the fabrication so far.

Here, the film fabrication by a sol-gel like spin coating process along with the characterization was carried out. Besides, the possibility for the porous carbon film fabrication was attempted using an organic template of Pluronic® P123.

4.2. Results and discussion

4.2.1. Preparation of the carbon precursor for spin coating

Several kinds of acrodam oligomer were prepared using acrodam as the starting material by varying the oligomerization catalyst or employing thermal treatment (Table 4–1). When a small amount of trifluoroacetic acid (TFA) was introduced to the reaction mixture as a catalyst for the 24 h refluxing, the number and weight average molecular weights (Mn and Mw) were found to be 1186 and 2595 by gel permeation chromatography (GPC) using dimethylsulphoxide (DMSO) as eluent along with poly(methylmethacrylate) (PMMA) standards. The oligomer was soluble in various organic solvents such as acetone, ethanol, THF, dimethylformamide (DMF) and DMSO. The molecular weight could be enhanced by using a weak base catalyst like triethylamine under the same reaction condition as TFA (Entry 2), but the resulting oligomer was soluble only in DMF and DMSO, which limits the choice of solvent for spin coating. Employment of a strong base such as *n*-butyllithium (^{n}BuLi) together with thermal

Table 4–1 Investigation on oligomerization method of acrodam.

Entry	Catalyst	Solvent	Reaction condition	Molecular weight[b]		
				Mn	Mw	Mw/Mn
1	CF_3COOH	THF	Reflux, 24 h	1186	2595	2.19
2	Et_3N	THF	Reflux, 24 h	1444	7717	5.34
3	^{n}BuLi	THF	Rt, 24 h	–[c]	–[c]	–[c]
4	None	None	140 °C, 24 h	–[c]	–[c]	–[c]
5	CF_3COOH[a]	THF	Reflux, 24 h	1267	3103	2.45

[a] Prepared directly from DAMN and acrolein.
[b] Determined using DMSO as eluent and PMMA standard.
[c] The molecular weights could not be determined owing to the insolubility in DMSO.

treatment at 140 °C has made the resulting oligomer definitely insoluble in any solvents (Entries 3 and 4), suggesting a higher molecular weight.

In addition, another TFA-catalysed oligomerization reaction was attempted by a one-pot process from diaminomaleonitrile (DAMN) and acrolein (Table 4–1, Entry 5). In order to synthesize the monomer acrodam, employment of diethyl ether is needed as solvent because oligomerization, which is suggested to proceed in a conjugate addition manner, can be prevented. On the contrary, the use of THF results in the mixture of acrodam and its oligomers since the solubility of acrodam is different between THF and diethyl ether.[37] THF is not beneficial in obtaining pure acrodam owing to its high solubility to the starting materials, but it is rather useful from an industrial point of view; additional synthesis steps are not needed because of the direct reaction from inexpensive and commercially available starting materials. Hence, THF was used in this study on purpose in place of diethyl ether. There was no considerable difference in molecular weights along with solubility between the two preparation methods (Entries 1 and 5).

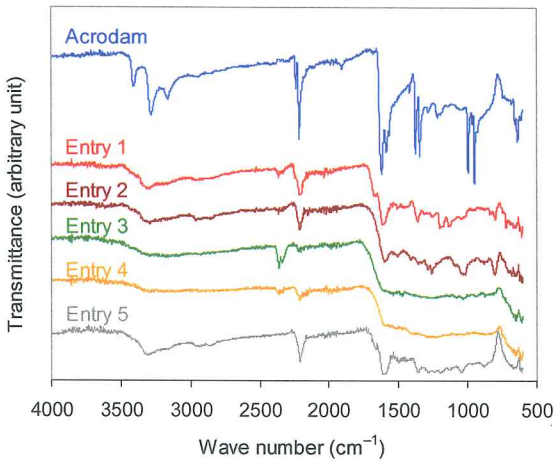

Figure 4–3 Fourier transform-infrared (FT-IR) spectra for acrodam and the oligomers. In this figure, "Entries 1–5" correspond to Table 4–1.

The structure for the oligomers was assessed by Fourier transform-infrared (FT-IR) analysis (Fig. 4–3). In comparison with the spectrum for the monomer acrodam, the peaks for amine (around 3300 and 1350 cm^{-1}) as well as acryl group (around 950 cm^{-1}) considerably diminished in each sample. Especially in the Entries 3 and 4 materials, the peaks for amine group, sp^3 C–H group (from 3000 to 2800 cm^{-1}, generated after conjugate addition) and nitrile group (around 2200 cm^{-1}) seems to be weaker than the other oligomers. This fact suggests that these groups might have involved in further oligomerization reactions *e.g.* cyclization reactions to form multi-azine and/or aromatic rings and conjugate additions, which is supported by the fact of their loss of solubility. The property for the Entry 5 material was similar to that for Entry 1, indicating that the oligomer structure was not altered significantly by the synthesis method. The peaks centred at around 2350 cm^{-1} originates from atmospheric carbon dioxide. Here, the Entry 5 product was employed for the further investigation due to the capability for an industrially useful one-pot reaction of the commercially available starting materials along with the good solubility to various solvents.

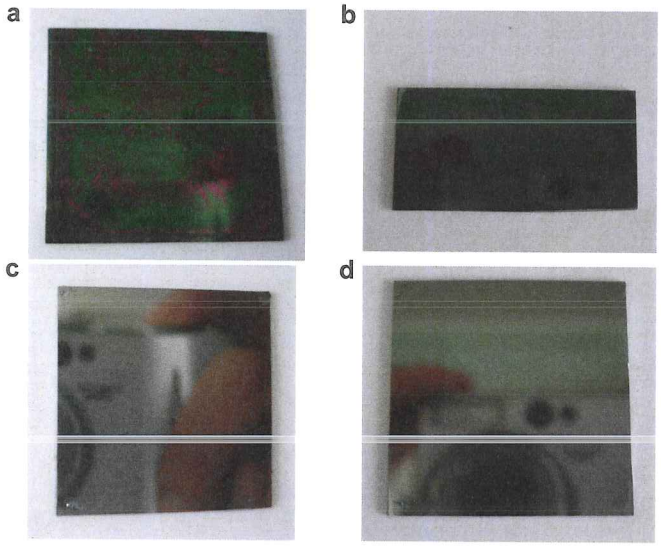

Figure 4–4 Digital photographs for the films.

a, Before carbonization. **b,** SCCF–600. **c,** SCCF–800. **d,** SCCF–1000.

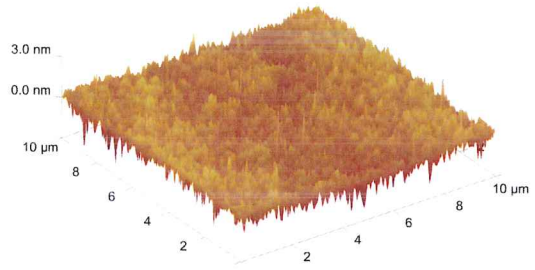

Figure 4–5 An image by atomic force microscopy (AFM) analysis for SCCF–800.

4.2.2. Carbon film fabrication and its characterization

Next, fabrication of the carbon film using spin coating method was attempted. After a piece of silicon substrate was spun with THF for cleaning, the 10 wt% oligomer solution including a small amount of Pluronic® P123 ($EO_{20}PO_{70}EO_{20}$) (1 wt% to acrodam) was spun at the rotation speed of 1200 rpm. Employing the solvent from the mixture of DMF and THF in the weight ratio of 1/1 was found to be effective in obtaining a film. When only DMF is employed, the solution repelled the silicon substrate owing to its low wettability. Introducing THF as a sole solvent failed to obtain a homogeneous film; the

Table 4–2 Summary of the film thickness and surface roughness.

Entry	Film	Thickness by SEM	R_q (nm)
1	SCCF–600	400 nm	Not determined
2	SCCF–800	220 nm	0.43
3	SCCF–800A[a]	810 nm	2.96
4	SCCF–1000	200 nm	0.38

[a] A thicker film than the other enrties was fabricated by chaging the coating method.

oligomer particles appeared soon after the coating had started due to its high vapour pressure along with the lower solubility than DMF. Besides, incorporation of P123 contributed to obtain a defect-free film, probably because it helps to lower the surface tension and enhances the wettability.

After the coated substrate was put on a hotplate for one minute at 200 °C, it was carbonized at elevated temperature under nitrogen atmosphere for one hour. Here, the films are named "SCCF–x", where "SCCF" stands for "spin coating carbon film" and "x" for carbonization temperature of the films prepared by the method described above. Both SCCF–800 and SCCF–1000 were mirror-like reflective films on the silicon substrate (Fig. 4–4), and found to have very smooth surfaces with the root mean square roughness (R_q) being about 0.4 nm by atomic force microscopy (AFM) analysis (Fig. 4–5 and Table 4–2). Their thickness was found to be in the hundred nanometre region by the cross-sectional scanning electron microscopy (SEM) (Table 4–2 and Fig. 4–6). The pictures also reveal that all the films are homogeneous, flat, void- and crack-free. The adhesion for SCCF–1000 was especially excellent; the film could not be completely scratched by a cutter knife enough to measure thickness by a surface profiler. The carbon film thickness could be raised up to 810 nm in the 800 °C carbonization by varying concentration for the solution along with decreasing the rotating speed in spin coating (this thicker film is named SCCF–800A), and the film also displayed a homogeneous cross section. However, it had to compromise with surface roughness and adhesion. R_q had a higher value of 2.96 nm in AFM analysis (Table 4–2) and the film could be easily peeled off with a piece of cellophane tape; in contrast, the 220 nm film (SCCF–800) had sufficient adhesion

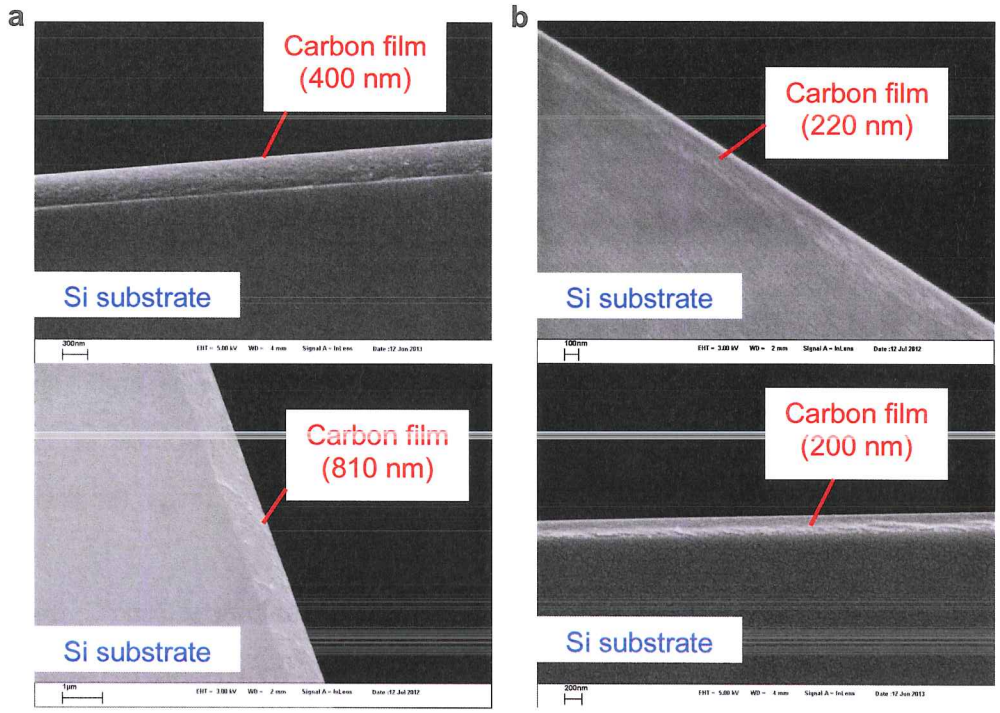

Figure 4–6 Cross-sectional scanning electron microscopy (SEM) images for the films.
a, SCCF–600. **b,** SCCF–800. **c,** SCCF–800A. **d,** SCCF–1000.

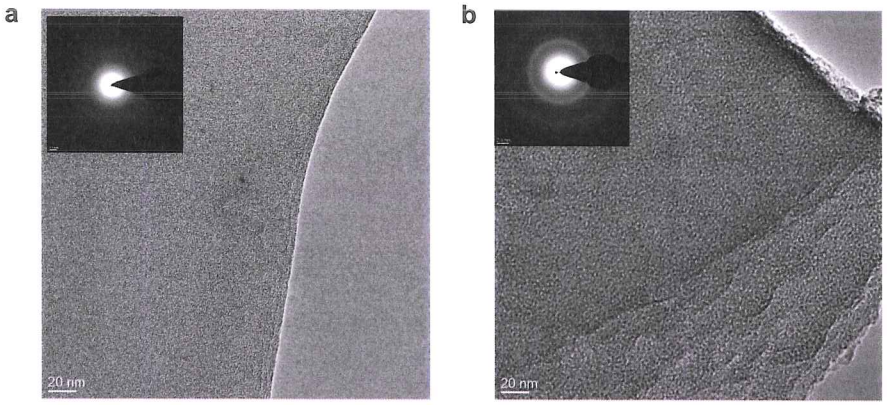

Figure 4–7 Transmission electron micrographs for the films. Inset: The selected area electron diffraction (SAED) images.
a, SCCF–600. **b,** SCCF–800.

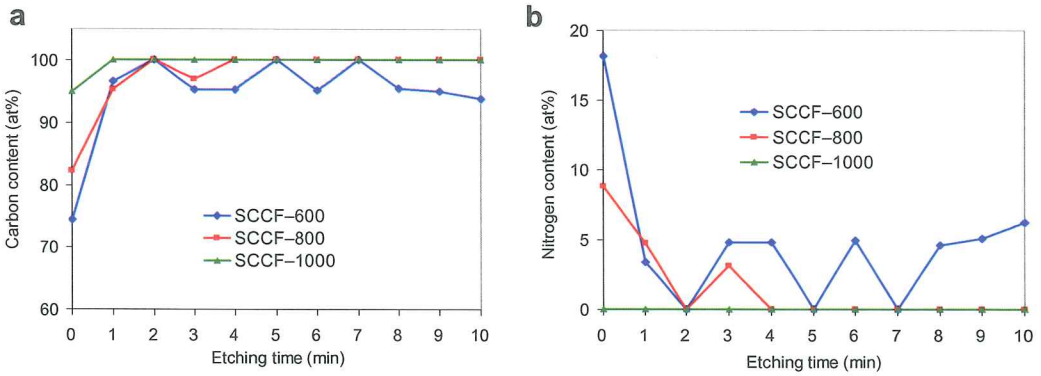

Figure 4–8 Depth profiles for the films by X-ray photoelectron spectroscopy (XPS).
a, The carbon content. **b,** The nitrogen content. Note that oxygen was detected only at the surface in each film.

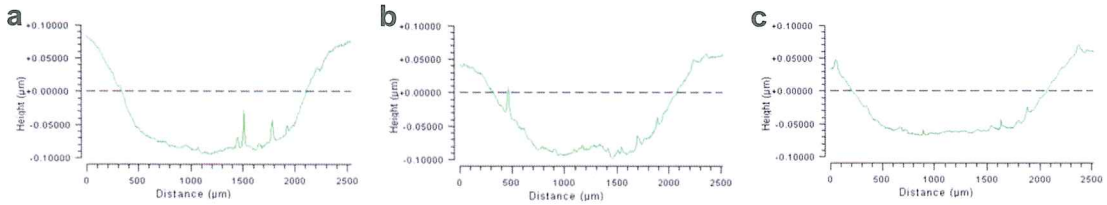

Figure 4–9 Topography measurements for the 10 min etched films using an optical surface profiler.
a, SCCF–600. **b,** SCCF–800. **c,** SCCF–1000. From this measurement, 0.18, 0.15 and 0.13 μm were confirmed to be etched, respectively.

towards the tape. This is probably due to increase of the internal stress in the thicker film generated during and after carbonization, some of which being released by peeling off, film shrinking, etc.

Transmission electron microscopy (TEM) pictures for SCCF–600 and SCCF–800, which are separated from the silicon substrate using 10 wt% potassium hydroxide aqueous solution for the observations,[51] also exhibited the homogeneity without finding an internal structure (Fig. 4–7). The selected area electron diffraction (SAED) images support the TEM observation results, displaying two amorphous halos with SCCF–800

being more distinct (Fig. 4–7, inset). This indicates that the film is comprised of small randomly distributed grains and has low degree of graphitization.

Depth profiles using X-ray photoelectron spectroscopy (XPS) for the films, which were conducted with argon ion (Ar^+) etching, revealed that there was considerable difference in the component proportion percentage between the surface and inside of the film (Fig. 4–8). Oxygen element was detected only at the surface; 10.2, 11.3 and 7.5 at% of oxygen were detected for SCCF–600, SCCF–800 and SCCF–1000, respectively, but no oxygen was observed inside the film. Oxygen atom is not included in acrodam oligomer; therefore, this is probably due to adsorption of the oxygen-containing species from ambient atmosphere such as carbon dioxide (CO_2) and water. On the other hand, the nitrogen element was detected in both the surface and the inside in SCCF–600 and SCCF–800, the content for the surface being much higher than that for the inside. Taking into the account the fact that only trace amount of nitrogen was detected in SCCF–1000, influence of nitrogen gas (N_2) adsorption onto the surface is considered to be limited; some of the nitrogen-rich moiety in the carbon precursor might have moved up to the surface during the thermal treatment. Besides, it is clear that the nitrogen content gradually decreased with raising the carbonization temperature, which reflects a gradual increase of the graphitization degree by losing the nitrogen element. After 10 min Ar^+ treatment towards the films, 0.18, 0.15 and 0.13 μm were confirmed to be etched in SCCF–600, SCCF–800 and SCCF–1000, respectively, which are estimated using an optical surface profiler (Fig. 4–9). A finer analysis for XPS N1s peaks of SCCF–600 and SCCF–800 with the three-minute etching, gave C–N or C≡N groups centred at 398.4 eV, while the rest belongs to C=N groups centred at 400.0 eV (Fig. 4–10). The ratio was not changed to a significant extent by the carbonization temperature with regard to the inside, but the C=N groups preferred to be at the surface to some extent (Table 4–3).

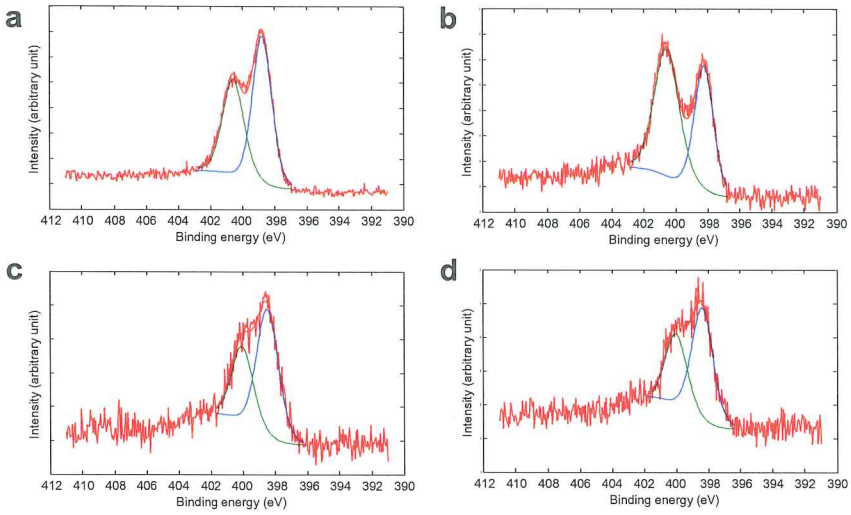

Figure 4–10 Finer analyses for N1s peaks for X-ray photoelectron spectrum.

a, SCCF–600 before etching. **b,** SCCF–800 before etching. **c,** SCCF–600 after 3 min etching. **d,** SCCF–800 after 3 min etching. Note that only trace amount of nitrogen was detected in SCCF–1000.

Table 4–3 Chemical state analyses with XPS N1s.

Film	At the surface (at%)		After 3 min etching (at%)	
	398.4 eV	400.0 eV	398.4 eV	400.0 eV
SCCF–600	56.8	43.3	62.6	38.7
SCCF–800	43.1	56.9	61.3	38.7

Electron energy loss spectroscopy (EELS) spectra were recorded in the carbon K-edge region to investigate the structure of the films (Fig. 4–11). The EELS can be used to distinguish between different carbon films such as diamond-like carbon (DLC), graphite and amorphous carbon.[175] The main EELS features in the carbon K-edge region are a peak at 285 eV that corresponds to the transitions from the 1s to the π^* states ($1s \rightarrow \pi^*$), and a peak at 291 eV that corresponds to the transitions from the 1s to the σ^* states ($1s \rightarrow \sigma^*$).[175] SCCF–1000 could not be measured because the film could not be separated from the silicon substrate even by the treatment with 10 wt% KOH aqueous solution.[51] The two typical peaks at 285 and 291 eV for graphite structure (Fig. 4–11) were broad displaying the amorphous structure, which agrees well with their TEM observation. In

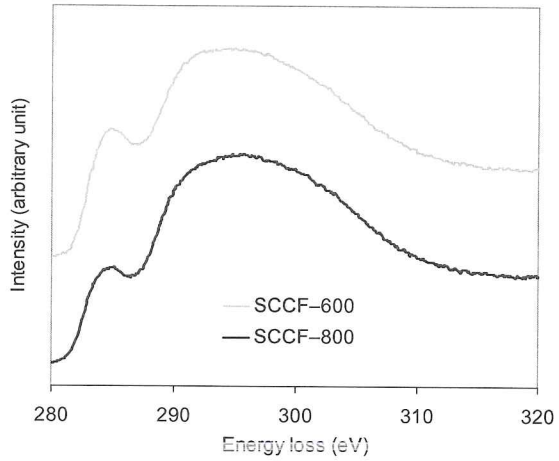

Figure 4–11 Electron energy loss spectra in the carbon K-edge region for the films.
The intensity is normalized to the σ* peak.

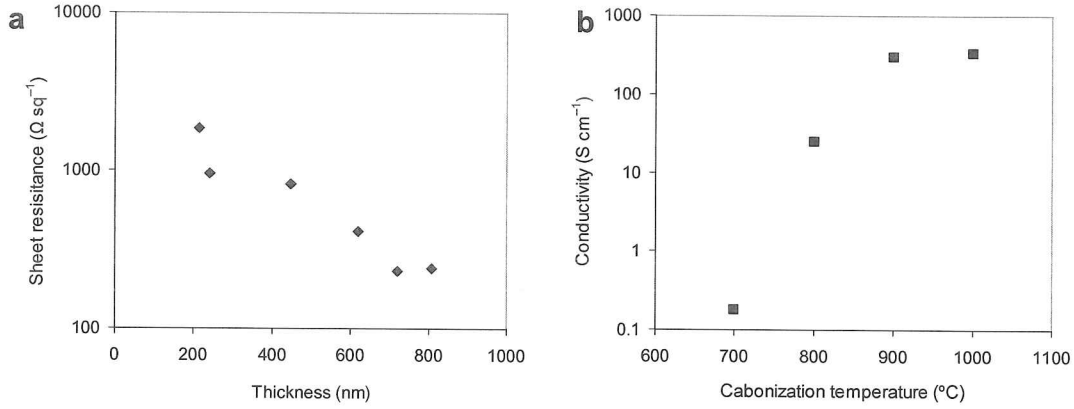

Figure 4–12 Electrical properties for the films.
a, Relation of sheet resistance to the thickness. **b,** Relation of conductivity to carbonization temperature using the films fabricated with the same procedure.

addition, all the chart for the σ* region were featureless, indicating that the film have significant amount of sp^3 carbon.

For understanding the electrical properties, sheet resistance of the carbon films was measured using a four-point method, varying thickness together with carbonization temperature. A 233 Ω sq^{-1} of sheet resistance could be obtained at the thickness of 721

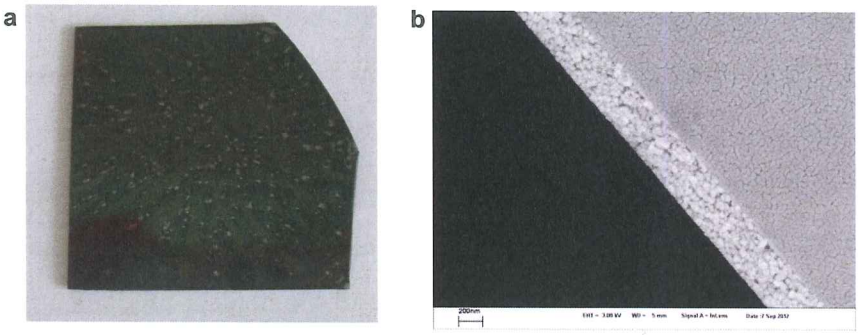

Figure 4–13 An attempt to prepare a porous carbon film.

a, A digital photograph for the carbonized film. **b,** A cross-sectional SEM image.

nm (Fig. 4–12), at which point the conductivity was calculated to be as high as 60 S cm^{-1}. This means that conductivity for the film is two order higher than that for the particle.[38] Besides, higher conductivity could be achieved with increasing the carbonization temperature; as high as 334 S cm^{-1} was obtained in SCCF–1000, which was similar to the 900 °C sample. The sheet resistance for SCCF–600 was too high to measure, calculation for the conductivity being not conducted. This corresponds to the observation that the film was not so reflective as the 800 and 1000 °C carbonized films (Fig. 4–4). This is the first example in which a film with such a high conductivity was achieved using a simple solution process to the best of the author's knowledge; it is higher than the films using photoresist (~ 10^{+1} S cm^{-1})[169] and resol precursor (26 S cm^{-1}),[167] being close to graphene oxide reduction system (10^{+3} S cm^{-1} order).[163]

4.2.3. An attempt to prepare a porous carbon film

Now that conductive films were found to be obtained using spin coating method with the acrodam oligomer, the fabrication possibility for a porous carbon three-dimensional film, which might be applied to electrode for supercapacitor, was examined. An organic oligomer of P123 was employed as template for the first attempt, because no further treatment such as washing after carbonization is needed in principle due to evaporation of the template during thermal treatment, which is very useful in commercialization. The films were prepared with a spin coater using the oligomer/P123 (in the weight ratio of

1/1) solution. As-coated film had defects and they did not disappear even after carbonization (Fig. 4–13a), indicating that influence of flow refilling during the thermal treatment was rather limited. However, the cross-sectional SEM picture clearly displayed the porous structure with about 400 nm thickness (Fig. 4–13b) in comparison with the template-free conditions discussed earlier (Fig. 4–6). This finding might contribute to further enhancement for the supercapacitor properties due to the contact resistance-free system.

Chapter 5

Conclusions and outlook

In this doctoral dissertation new heteroatom-containing carbons in the form of particles and three-dimensional films were prepared and examined, with a view to attaining high energy density supercapacitor systems that can be comparable to that for batteries. Acrodam-derived carbons enabled a significant progress in this field. In the form of particles, which were prepared through the reaction in a salt-flux, an excellent energy density could be achieved in redox-active electrolytes. Highly conductive carbon three-dimensional films could be fabricated by industrially versatile solution process, and possibility of the porous carbon film fabrication which might be employed for supercapacitor electrode was also elucidated.

In Chapter 2, a high capacitance porous carbon, which was synthesized from acrodam along with caesium acetate as a meltable flux agent, was established as electrode. The salt caesium acetate turned out to promote homogeneous dissolution of the educts and acts as a large molecular template which can be easily removed and recycled after the carbon condensation step. The acetate counterion was shown to contribute to carbon formation rather than being a classical etching activation agent. Porosimetry revealed a high pore volume/high surface area pore system (up to 1.64 mL g^{-1} and 2413 m^2 g^{-1}), which is fully accessible with pores sized of the Cs-ion pairs or small salt clusters, *i.e.* exactly the conceptual size range discussed to be useful and needed for supercapacitance. Due to the higher content for heteroatoms (oxygen and nitrogen), the carbon electrode exhibited much higher capacitances (up to 298 F g^{-1}) than a commercially available activated carbon in sulphuric acid aqueous solution. The effectiveness was also confirmed in potassium hydroxide aqueous solution. The salt-flux carbon, SFC–9–800, showed an excellent energy density up to 41.8 Wh kg^{-1}.

In Chapter 3, redox-active aqueous electrolytes were employed with the salt-flux carbon electrode for obtaining enormous capacitive contributions in supercapacitor systems through reversible Faradaic reactions. The hydroquinone-loaded sulphuric acid as well as potassium iodide solution as electrolyte afforded the superior properties for supercapacitors with these salt flux carbons; above all, specific capacitances around 1000 F g^{-1} and energy densities as high as 133.0 Wh kg^{-1} were achieved in hydroquinone-loaded sulphuric acid. Furthermore, these systems exhibited excellent cycle stabilities, more than 85% of energy density being retained even after the 2500 cycle (2 A g^{-1}) or 10000 cycle (10 A g^{-1}) measurement. These properties are already now comparable to those of current LIB, using cheap and safe redox-doped sulphuric acid as a solvent system. Here, a high energy density supercapacitor system only composed of simple, sustainable and non-combustible components was established. Energy density considerably decreased during the cycle stability test in copper and iron ion-loaded sulphuric acid. However, in comparison with the result in the only copper-loaded electrolyte, iron ions were found to promote reionization of the deposited copper metal to some extent, which resulted in the stability enhancement.

In Chapter 4, conductive carbon three-dimensional films were fabricated using the solution of acrodam oligomer as the precursor by the spin coating method. The oligomer could be easily synthesized by a one-pot procedure from the same starting materials for the monomer acrodam (DAMN and acrolein). The films were found to be homogeneous, flat, void- and crack-free, and could be fabricated up to 810 nm thickness in the 800 °C carbonization. They were found to include considerable amount of sp^3 carbon by EELS analysis. High conductivities (up to 334 S cm^{-1}) were achieved at the carbonization temperature of 1000 °C. Furthermore, a porous carbon three-dimensional film could be formed using an organic template at the first attempt, although the film had significant amount of defect. This finding demonstrates the film's potentiality for various applications such as supercapacitor electrode; the essential absence of contact resistance

within the network should contribute to effective transportation of electron within the electrode.

The author believes that further progress could be made based on the acrodam-derived system. For further enhancing the properties of supercapacitor, the investigation below can be considered for example:

- First, in principle, the energy density can be much enhanced by employing electrolytes such as ionic liquids (ILs) or utilizing other possible redox mediators into conventional aqueous solutions. Energy density is calculated by the operating voltage squared; therefore ILs, some of which have much higher operating voltage (up to 6 V)[6] than aqueous electrolytes, should contribute to the considerable enhancement. Besides, since the investigation on redox-active electrolytes has just started recently, mediators which exceed hydroquinone might be found in the not so distant future.
- Secondly, examination on other salts than caesium acetate for preparing porous carbons might lead to further enhancement of capacitance for the carbons. The pore properties and the heteroatom contents, which are important in determining the capacitive behaviour, might be more sophisticated by varying anion as well cation of the salt.
- The last but not least, introducing other components into the carbons in this study might enhance the properties. Hybrid of the salt-flux carbons with the materials exhibiting pseudocapacitive behaviour such as metal oxides and conductive polymers might contribute to afford more capacitance. Besides, introduction of rigid structures like acetylene moiety into the carbon precursor might lead to enhance the carbonization yield, which is of advantage in the effective use of the precursor as well as preparing thicker films due to decrease of the internal stress. Moreover, metal incorporation that works as a graphitization catalyst might

contribute to lower the carbonization temperature, which enables the film fabrication on the lower melting point substrates.

The supercapacitor was chosen here for application of the acrodam-derived carbon, but this material could be potentially utilized in various other applications including electrodes for batteries, catalysts for oxygen reduction reaction (ORR) as well as various organic reactions, thermal and/or electrical conductive films, gas storage materials, materials for biomaker, etc. In most cases, employment of carbon three-dimensional films using solution process, which are free of contact resistance, should afford a significant positive influence on the properties.

The author believes that the progress made in this dissertation will open a new way to further enhancement of energy density for supercapacitor as well as other applications that exceeds the current properties. Further development on both the materials and the applications in this field is eagerly awaited.

Chapter 6

Experimental

6.1. Materials

All the chemicals in this study including diaminomaleonitrile (DAMN) (Alfa Aesar, 98%), acrolein (Aldrich, 95%), trifluoroacetic acid (TFA) (Aldrich, 98%), caesium acetate (CsOAc) (Aldrich, 99.9%), polyvinylidene fluoride (PVDF) (MTI Corp.), hydroquinone (HQ) (Sigma-Aldrich, 99.5%), potassium iodide (KI) (Sigma-Aldrich, 99%), copper (II) sulphate pentahydrate ($CuSO_4 \cdot 5H_2O$) (Sigma-Aldrich, 98.0%), iron (II) sulphate heptahydrate ($FeSO_4 \cdot 7H_2O$) (Aldrich, 98%), Norit DLC SUPRA 30 (Norit AC), triethylamine (Sigma-Aldrich, 99%), *n*-butyllithium (^{n}BuLi) (Aldrich, 2.5 M in hexanes), Pluronic® P123 ($EO_{20}PO_{70}EO_{20}$) (BASF), ethanol (VMR, 99.8%), tetrahydrofuran (THF) (VMR, 99.8%), diethyl ether (Merck, 99.7%), hexane (VMR, 95%) and DMF (Sigma-Aldrich, 99.8%) were used as received without further purification. *p*-Type silicon (100) substrates were purchased from Active Business Company GmbH.

(1*Z*)-1-Amino-1,2-dicyano-3-aza-1,3,5-hexatriene (acrodam) was synthesized according to the reported procedure.[37] The structure was confirmed the same as the reported data.[38,176] Typical procedure: To a 250 mL round bottom flask with a magnetic stirring bar in a ventilation hood, were added DAMN (5.41 g, 50 mmol) and diethyl ether (60 mL), which was allowed to cool for 15 min using an ice/water bath. To this mixture, 4.0 mL of acrolein (55 mmol) was added with stirring, and the mixture was again allowed to cool for another 15 min. After addition of 0.06 g of TFA with small amount of diethyl ether, the reaction solution was kept stirring for 30 min, during which the reaction solution became heterogeneous. The reaction mixture was poured into 400 mL of pre-cooled hexane, the resulting solid being collected by filtration under reduced pressure, affording the quantitative amount of acrodam.

Preparation of Cs salt-flux carbons (for Chapters 2 and 3)

In a glass bottle, a brown solution from acrodam (0.50 g) with 1.5 g of THF and 3.0 g of ethanol was prepared. A solution from CsOAc (4.50 g in SFC–9–800 for instance) with 1.5 g of pure water and 3.0 g of ethanol was prepared in another bottle as well, which was poured into the acrodam solution prepared earlier with magnetic stirring. The resulting homogeneous solution was heated at 90 °C under ambient atmosphere in a ventilation hood for one day to remove the solvents, the precursor for the salt-flux carbons being obtained. It was put into a ceramic crucible with a lid, and heated with a rate of 100 K h^{-1} to the purpose temperature (700, 800 or 900 °C) under N_2 in a Nabertherm N7/H Chamber Oven, keeping the temperature for one hour. After cooling down to room temperature, the resulting solid was washed with pure water twice and pH 7 for the second filtrate was confirmed. Following stirring in ethanol, the collected solid was evacuated at 60 °C under reduced pressure. All the measurements were carried out after grinding the solid. The samples are named "SFC–x–y", where "SFC" denotes salt flux carbon, "x" stands for the CsOAc/acrodam weight ratio and "y" for the thermal treatment temperature (700, 800 or 900 °C).

Preparation of acrodam oligomer (for Chapter 4, Table 4–1, Entry 1)

To a 100 mL round bottom flask fitted with a magnetic stirring bar under nitrogen atmosphere, were added acrodam (1.00 g) and THF (10 mL). After the homogeneous solution was obtained, 0.08 g of TFA was added and the solution was heated to reflux for 24 h. After cooling down to room temperature, the reaction mixture was evaporated under reduced pressure, and the resulting solid was ground. The solid was further evacuated under reduced pressure at 60 °C, affording the quantitative amount of acrodam oligomer. The oligomers for Entries 2–4 were also prepared under the conditions as shown in the Table 4–1.

Preparation of acrodam oligomer (for Chapter 4, Table 4–1, Entry 5)

The oligomer was synthesized utilizing the same procedure for acrodam preparation except that THF was employed instead of diethyl ether. To a 250 mL round bottom flask in a ventilation hood, fitted with a magnetic stirring bar and an ice/water cooling bath, were added DAMN (5.41 g, 50 mmol) and THF (60 mL), which was allowed to cool for 15 min. To this mixture, 4.0 mL of acrolein (55 mmol) was added with stirring, and the mixture was again allowed to cool for 15 min. After addition of 0.06 g of TFA with small amount of diethyl ether, the reaction solution was allowed to stir for 30 min in total. Following the system was kept under N_2 atmosphere, the reaction mixture was heated to reflux for 24 h. It was homogeneous all the time. It was evaporated under reduced pressure, and the resulting solid was ground. The solid was further evacuated under reduced pressure at 60 °C, affording the quantitative amount of acrodam oligomer.

Fabrication method of carbon films without template (for Chapter 4)

For preparing the coating solution by spin coating, 0.10 g of the acrodam oligomer synthesized above, 1 mg of P123, 0.45 g of DMF and 0.45 g of THF was added into a glass bottle. After confirming that all ingredients dissolved into homogeneous solution, part of the solution was poured onto a piece of silicon substrate (3 cm × 3 cm in size) which had been beforehand cleaned by spinning with sufficient amount of THF. The substrate was spun at the speed of 1200 rpm for 15 s, and it was put on a 200 °C hotplate for one minute. After cooling down to room temperature, it was put in a ceramic container with a lid and heated under a nitrogen (N_2) flow using a rate of 100 K h^{-1} from room temperature to the desired temperature, at which the sample was kept for one hour. For changing the film thickness, the solution concentration as well as the spin speed was varied.

Fabrication method of carbon films with template (for Chapter 4)

For preparing the coating solution by spin coating, 0.10 g of the acrodam oligomer synthesized above, 0.10 g of P123, 0.45 g of DMF and 0.45 g of THF was added into a

glass bottle. After confirming that all ingredients dissolved into homogeneous solution, part of the solution was poured onto a piece of silicon substrate (3 cm × 3 cm in size) which had been beforehand cleaned by spinning with sufficient amount of THF. The substrate was spun at the speed of 600 rpm for 180 s. The film was put in a ceramic container with a lid and heated under a nitrogen (N_2) flow using a procedure shown in Fig. 6–1.

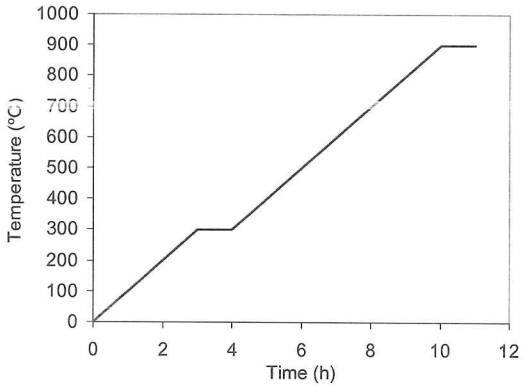

Figure 6–1 Procedure for the thermal treatment of porous carbon film fabrication.

6.2. Characterization methods

6.2.1. Characterization

Isolated yield for the Cs salt-flux carbons was calculated by dividing the amount for the final carbon after grinding by the acrodam amount.

Anions for the first filtrate after caesium species removal were analysed by CURRENTA GmbH: Hydroxide ion was estimated by measuring pH using a pH-electrode. Total inorganic carbon (TIC) measurement was performed using a TIC-Analyzer (Shimadzu) with IR-detection. Other ions were measured using ion chromatography with conductivity detector. Prior to analysis, the sample was diluted and neutralized using a cationic ion exchanger.

N_2 sorption measurement was carried out at 77 K using a Quantachrome Quadrasorb SI porosimeter equipped with an automated surface area and pore size analyzer. Prior to

measurements, samples were degassed at 150 °C for 20 h using a Masterprep degassing system. For estimating the Brunauer-Emmett-Teller (BET) surface area, the relative pressure range of $P/P_0 < 0.11$ was chosen.[177] The pore size distribution as well as the pore volume was calculated from N_2 sorption data using the non-local density functional theory (NLDFT) equilibrium model method for slit pores provided by Quantachrome data reduction software QuadraWin Version 5.05.[178]

Combustion elemental analysis was performed on a Vario Elmer-Perkin elemental analyzer.

X-ray photoelectron spectroscopy (XPS) was accomplished using a Quantum2000 instrument with monochromatic X-ray source AlKα (1486.6 eV) and a monochromatic spot of 100 μm by Mr. Tomikazu Ueno (JSR Corporation, Japan). Binding energies for the high-resolution spectra were calibrated by setting C 1s at 285.0 eV.

Inductively coupled plasma-optical emission spectroscopy (ICP-OES) analyses were performed using an OPTIMA 2100 DV instrument (Perkin Elmer) by Dr. Hendrik Wetzel (Fraunhofer Institut).

Wide-angle X-ray scattering (WAXS) patterns were recorded with a Bruker-D8 Advance instrument, operating with Cu–Kα radiation ($\lambda = 1.54$ Å).

Thermogravimetric analysis (TGA) was conducted on a Netzsch TG 209 F1 under mixed air and N_2 with a flow rate of 100 mL min^{-1} and temperature ramp of 10 K min^{-1}.

Scanning Electron Microscopy (SEM) was performed using a Gemini Leo-1550 instrument after sputtering with platinum.

Transmission electron microscopy (TEM) images for Chapter 2 were obtained using a Zeiss EM 912Ω instrument. For Chapter 4, TEM and electron energy loss spectroscopy (EELS) investigations have been carried out on a Philips CM 200 FEG equipped with a Gatan Tridiem Filter. The TEM sample was prepared by mortaring the samples and then dry deposition of the obtained powder on Cu supported holey carbon grids, after separating the film from the silicon substrate using 10 wt% potassium hydroxide aqueous solution.[51] The EELS data processing such as background removal and removal of plural scattering contributions were done with the Digital Micrograph software package.

GPC results are collected in a Thermo-Fischer GPC device equipped with a Shodex RI detector and a PSS-GRAL-LIN:VS+-+HS column (300 mm × 7.5 mm, Polymer Standard Service, Mainz). 0.5 g L^{-1} lithium bromide-loaded DMSO was used as eluent. The molecular weights were estimated from a calibration relative to polymethylmethacrylate (PMMA) standards.

Fourier transform-infrared (FT-IR) spectra were recorded with a Varian 1000 FT-IR spectrometer, equipped with an attenuated total reflection (ATR) setup.

Atomic force microscopy (AFM) was performed on a NanoScope IIIa device (Veeco Instruments, Santa Barbara, CA) in tapping mode. Commercial silicon tips (Type NCR-W) were used with a tip radius < 10 nm and a spring constant of 42 N m^{-1} at a resonance frequency of 285 kHz.

An Alpha-Step IQ surface profiler (KLA-Tencor) was used for measuring the film thickness by Mr. Hisashi Nakagawa (JSR Corporation, Japan).

The sheet resistance of the films was measured using a four-point probe resistivity meter (Loresta-GP MCP-T600, Mitsubishi chemical, Japan) by Mr. Hisashi Nakagawa (JSR Corporation, Japan). Conductivity was calculated by multiplying sheet resistance value with the thickness.

6.2.2. Electrochemical measurement

For electrode preparation, 10 mg of the carbon was put into a small bottle, where 200 µL of N-methylpyrrolidone (NMP) solution of polyvinylidene fluoride (PVDF), which was beforehand prepared by dissolving 52 mg of PVDF and 10 mL of NMP, was poured. This means the carbon/PVDF weight ratio equals to 90/10. After thorough dispersion, 60 µL of the solution was poured onto a platinum-coated circular-shape carbon disk (1 cm in diameter) as current collector with a micropipette. After removing most of the solvent at 120 °C at ambient pressure, it was further put under reduced pressure for overnight. The weight for the electrode was about 2 mg. Two disks thus prepared were employed to form a two-electrode symmetric Swagelok® type cell, separated by a piece of filter paper. 5 drops of electrolyte (aqueous solutions of 1 mol L^{-1} H_2SO_4 (H_2SO_4), 6 mol L^{-1} KOH

(KOH), 0.38 mol L^{-1} HQ dissolved in 1 mol L^{-1} H_2SO_4 (HQ/H_2SO_4), 0.5 mol L^{-1} copper (II) sulphate and 0.5 mol L^{-1} iron (II) sulphate dissolved in 1 mol L^{-1} H_2SO_4 ($Cu/Fe/H_2SO_4$) or 1 mol L^{-1} potassium iodide (KI)) were put inside the cell. The cell was connected to an Interface Gamry 1000 potentiostat and all the electrochemical measurements (cyclic voltammetry (CV), galvanostatic charge/discharge profile and electrochemical impedance spectroscopy (EIS)) were carried out at room temperature. The CV charts were recorded with the voltage range of 0–1 V at 2, 20 and 200 mV s^{-1}, the second cycle being adopted. The galvanostatic charge/discharge measurements were carried out with the voltage range of 0–1 V at different current densities ranging from 0.1 to 10 A g^{-1} based on the total mass of the carbons, the fifth cycle being employed. EIS measurements were carried out in the frequency range from 1 mHz to 100 kHz with the alternate current amplitude of 10 mV.

The specific gravimetric capacitance of the supercapacitor cell (C^s_{total}) was evaluated from the charge/discharge test using the following equation:

$$C^s_{total}\,(\mathrm{F\ g^{-1}}) = \frac{I \times \Delta t}{V \times m} \qquad (6\text{–}1)$$

where I in A is the constant discharging current, Δt in s is the discharge time, V in V is the maximal operation voltage during the discharge process excluding the IR drop, and m in g is the total mass of the two-electrode materials, respectively. In order to evaluate the specific capacitance of a single electrode, the fact that two separate capacitors are connected in series to form a two-electrode supercapacitor has to be considered. Thus, it is four times the total cell specific capacitance (equation (2)) from the calculations below (equations (3) and (4)):[179]

$$C^s\,(\mathrm{F\ g^{-1}}) = 4 \times C^s_{total} \qquad (6\text{–}2)$$

$$\frac{1}{C_{total}} = \frac{1}{C} + \frac{1}{C} \qquad (6\text{–}3)$$

$$\frac{C^s}{C^s_{total}} = \frac{C/m'}{C_{total}/2m'} = \frac{4}{1} \qquad (6\text{–}4)$$

where C is capacitance of the single electrode, C_{total} is capacitance of the testing cell, C^s is specific capacitance of the single electrode, C^s_{total} is specific capacitance of the whole testing cell, and m' is the mass of the single electrode.

The specific energy density (E) and power density (P) are defined as below;

$$E\,(\mathrm{Wh\ kg^{-1}}) = \frac{0.5 \times C^s \times V^2}{3.6} \qquad (6\text{–}5)$$

$$P\,(\mathrm{kW\ kg^{-1}}) = \frac{3600 \times E}{\Delta t} \qquad (6\text{–}6)$$

6.3. Selected measurement principles

6.3.1. Gas sorption

Gas sorption measurement is one of the most important methods to characterize porous materials. This allows for qualitative and quantitative determination for physicochemical properties such as the surface area, pore volume and pore size distribution.[180] Nitrogen, argon, krypton and carbon dioxide are used as model adsorbates and usually, nitrogen is employed as an adsorptive and the measurement is performed at 77 K (that is, the boiling point of nitrogen). This ensures solely weak interaction through van der Waals interaction of the adsorbent and adsorbate which is called physisorption and enables multilayer formation. After adsorption equilibrium vapour pressure (P_0) has been established, the amount adsorbed is calculated from the change in pressure and the results are derived from the relation between relative pressure (P/P_0) and volume of adsorbed gas. The respective plot (the sorption isotherm) indicates the type and quantity of pores. With regard to the different sorption effects caused by different pore sizes, porous materials are classified by the IUPAC into three categories:[181]

micropores (< 2 nm) < mesopores (2 – 50 nm) < macropores (> 50 nm).

The three classes possess different adsorption effects which allow the assignment of characteristic isotherm shapes to certain pores. It is distinguished by six types of isotherms (Fig. 6–2).

Type I isotherms are characteristic for microporous materials having relatively small external surfaces. Because the small pores are already filled at low relative pressures ($P/P_0 < 0.1$) due to micropore filling, the amount of adsorbate reaches a plateau as P/P_0 approaches 1. Type II isotherms are obtained for macro- or non-porous materials and displays unrestricted monolayer-multilayer adsorption. The point B indicates the complete coverage of the first layer after which multilayer formation starts. Type III isotherms are uncommon and are observed when the adsorbate/adsorbent interaction is important. Type IV isotherms with a hysteresis loop are characteristic for mesoporous materials. Here, the nitrogen uptake is typically limited at high relative pressures. Furthermore, a steep increase of the adsorption branch at higher relative pressures can be attributed to capillary condensation in mesopores where the pore size and form govern the isotherm shape. It is admitted that the different shapes of the hysteresis are related to different pore structures in terms of shape, pore connectivity and cavitations in the material, which are influencing the capillary condensation inside the mesopores. Type V isotherms are also uncommon but are obtained in porous materials with weak adsorbate/adsorbent interactions, while a type VI isotherm represents a stepwise multilayer adsorption on a uniform non-porous surface, where the step-height represents the monolayer capacity for each adsorbed layer.

For determination of the surface area of solid materials, the BET method, which was established by Brunauer, Emmett and Teller, is the most widely used procedure.[113] The surface area is determined by the relation of the adsorbed volume to the thickness of mono- and multilayer formation on the pore walls. Besides, the density functional theory (DFT) has been recently used for the determination of micro- and mesoporous materials.

In this dissertation, the non-local DFT (NLDFT) method was chosen, because it correctly describes the local fluid structure near curved solid walls; adsorption isotherms in model pores are determined based on the intermolecular potentials of the fluid-fluid and solid-fluid interactions.

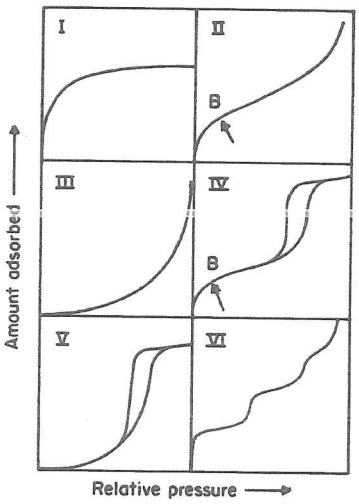

Figure 6–2 Types of physisorption isotherms.[181]

6.3.2. Combustion elemental analysis

Elemental analysis is an experiment that determines the amount (typically a weight per cent) of an element in a compound.[182] Because there are many different elements, there are many different experimental methods for determining elemental composition. The most common type of elemental analysis is for carbon, hydrogen, nitrogen and sulphur (CHNS analysis), which is analysed by burning under O_2 atmosphere. This type of analysis is especially useful for organic compounds (compounds containing carbon-carbon bonds).

6.3.3. X-ray photoelectron spectroscopy (XPS)

When the surface is irradiated with X-rays, electron emission occurs due to the photoelectric and Auger effects. The photoelectron emission process is illustrated in Fig. 6–3. The kinetic energy of the emitted photoelectrons is given by:[172]

$$E_K = h\nu - E_b - W_s \qquad (6\text{–}7)$$

where hν is the energy of the photon, E_b is the binding energy of the atomic orbital from which the electron originates, and W_s is the spectrometer work function. Because the energy of the released electrons also depends on their chemical and electronic environment, XPS can be used to identify and determine the concentration of the elements within the escape depth of the photoelectrons in the near surface region with a maximal depth of around 5 to 10 nm, although X-ray photons penetrate the sample to a micrometre. Hence, ultra-high vacuum is necessary for the measurement. And it should be noted that the element of hydrogen and helium cannot be measured because their ionization energy are too small. Variations in the elemental binding energies (the chemical shifts) arise from the differences in the chemical potential and polarizability of the compounds. These chemical shifts can be used to identify the chemical state of the materials.[172]

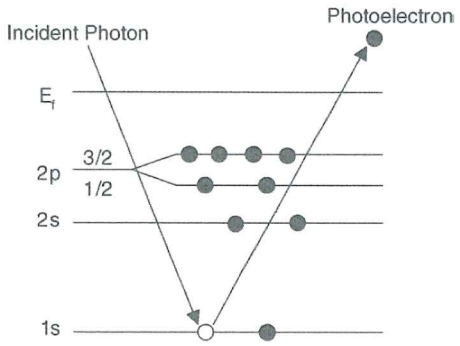

Figure 6–3 Schematic of the emission process of photoelectrons excited by X-rays.[172]

6.3.4. Scanning electron microscopy (SEM)

Scanning electron microscopy (SEM) is an equipment which allow for imaging materials at high magnifications using the wave behaviour of accelerated electrons.[172] In a SEM instrument, a voltage is applied to an electron emitting filament typically made of W or LaB_6 to produce an electron beam. The electrons are focused by electron optics including

condenser lenses and objective lenses, and eventually covered by a set of scanning coils onto the sample surface. The electrons interact with the top few nanometres to several microns of the sample. The contrast is due to varying probabilities of electrons to be released from different sample areas. Thus, SEM gives a three-dimensional image of the surface topology. In order to guarantee an efficient electron release, the samples have to be conductive; otherwise, the surface is sputtered with a metal such as gold or platinum. This technique also enables the visualization of structures on the nanometre scale.

6.3.5. Transmission electron microscopy (TEM)

In TEM, the transmission of electrons through a very thin sample is used to obtain much higher resolution than SEM.[172] The electrons pass through the thinned materials, and the output (image) is modulated by the structure (opaqueness) of the materials. The electrons interact in several ways with the solid material, such as absorption, diffraction and elastic or inelastic scattering. The intensity of the transmitted electron beam varies with the sample structure. The transmitted image is magnified and projected onto the viewing screen. As a result, heavy elements lead to stronger scattering, which results in fewer electrons reaching the image plate. Hence, sample regions containing these elements appear comparably dark. On the other hand areas with only lightweight elements, such as typical organic compounds, result in limited scattering of electrons and therefore the image becomes bright. The wavelength of electron beam is much less than that of the visible light (wavelength of green light is 500 nm versus λ = 0.004 nm for 100 keV electron) and there is very little electron deflection through a thin specimen; therefore, much higher resolution (atomic scale) than that achievable by optical microscopy and even conventional SEM can be obtained.

6.3.6. Electron energy loss spectroscopy (EELS)

Electron energy loss spectroscopy is a very powerful method to study the detailed structures.[172] When an electron beam interacts with a film, it can give up all or part of its energy in the process depending on various inelastic scattering processes within the

sample. The energy loss corresponds to the film electron arrangement of the solid. By collecting the electron energy loss information, the bonding or vibrational information of the solid can be obtained.

EELS has been shown to be a very useful tool in the unambiguous identification of diamond and graphite.[173,175] For diamond in the higher energy loss region, only the K edge peak at around 291 eV due to the excitation of σ* states of sp^3 appears, but the peak at 285 eV due to excitation to π* states cannot be observed. Both the 285 eV and 291 eV peaks will appear in graphite EELS. The latter peak is due to the π* states of sp^2. It can be postulated that in amorphous carbon films or in nanocrystalline carbon films, the 285 eV peak and 291 eV peak will appear because the film structures are usually composed of either sp^2 or sp^3.

6.3.7. Wide angle X-ray scattering (WAXS)

When X-ray radiation passes through a matter, the radiation interacts with the electrons in the atoms, resulting in scattering of the radiation. If the atoms are organized in planes (*i.e.*, the matter is crystalline) and the distances between the atoms are of the same magnitude as the wavelength of the X-rays, constructive and destructive interference will occur. This results in diffraction where X-rays are emitted at characteristic angles based on the spaces between the atoms organized in crystalline structures called planes.[183]

Most crystals can have many sets of planes through their atoms. Each set of planes has a specific interplanar distance and will give rise to a characteristic angle of diffracted X-rays. The relationship between wavelength, atomic spacing and angle was solved as the Bragg equation. If the illuminating wavelength is known (depends on the type of X-ray tube and if a monochromator is employed) and the angle can be measured (with a diffractometer) then the interplanar distance can be calculated from the Bragg equation. Here, the diffraction lines become broader with decreasing structure size and increasing lattice imperfection. The lattice planes can be classified by the Miller Indices (hkl) which are defined as the reciprocal points of intersection of the planes with the unit cell. In addition, the crystallite size can be estimated by the Scherrer equation.

6.3.8. Electrochemistry

Cyclic voltammetry (CV) is useful as a quick screening procedure to identify potential capacitor materials. The experimental procedure involves potential cycling between two voltage values preselected for a given electrolyte.[41] Besides, adsorption phenomena such as double layer charging are detectable which enables the determination of a capacitive behaviour. Furthermore, electrochemical reactions such as redox reactions can be identified by current changes.

In galvanostatic charge/discharge measurements, the cell is charged and discharged at a constant current. By computing the input energy and the realized output energy, figures of merit for the charge and discharge efficiency can be derived. The magnitude of the internal resistance can be used to understand the compound energy efficiency, *i.e.*, large internal resistance lead to poor energy efficiency. The external resistance of the system (*e.g.*, solution resistance) can be determined by means of the impedance measurements, with data plotted according to complex-plane analysis.

The frequency-response characteristics of a capacitor and its equivalent series resistance (ESR) are important in an evaluation of a capacitor and are dependent upon: (1) the intrinsic nature of the electrode material; (2) the pore-size distribution of the high-area material used in the fabrication of the electrodes; and (3) the engineering parameters used in the preparation of the electrodes, *e.g.*, the thickness of the active material of the electrode and the nature of the particle-particle contact, as well as the macropore distribution as determined by the applied pressure. Impedance spectroscopy provides a convenient way to assess the frequency-response characteristics of a capacitor material, especially the power-limiting internal resistance. In Nyquist plots, the imaginary component, Z_{imag}, shows the capacitive property and the real component, Z_{real}, shows the ohmic property.[179] These plots usually consist of one or more semicircles in the complex plane. The theoretical Nyquist plot of a supercapacitor consists of three regions which are dependent on the frequencies. At very high frequency, the supercapacitor behaves like a pristine resistor. At low frequency, the imaginary part sharply increases and a nearly

vertical line is observed, indicating a pristine capacitive behaviour. In the medium frequency domain, the influence of the electrode porosity can be observed. When the frequency decreases, starting from the very high frequency, the signal penetrates deeper and deeper into the porous structure of the electrode, then more and more electrode surface becomes available for ion adsorption. This medium frequency range with the 45° segment is related to the electrolyte penetration in the porous structure of the high porosity electrode, and usually called the Warburg curve.[179]

References

[1] P. Simon, Y. Gogotsi, *Nat. Mater.* **2008**, *7*, 845.

[2] K. B. Hueso, M. Armand, T. Rojo, *Energy Environ. Sci.* **2013**, *6*, 734.

[3] For example, a fire incident of the LIB in a Boeing 787 at Boston's Logan Airport on January 2013, a fire incident of the LIB in a Mitsubishi's automobile on March 2013, etc.

[4] Y. Zhai, Y. Dou, D. Zhao, P. F. Fulvio, R. T. Mayes, S. Dai, *Adv. Mater.* **2011**, *23*, 4828.

[5] J. Zhang, X. S. Zhao, *ChemSusChem* **2012**, *5*, 818.

[6] G. Wang, L. Zhang, J. Zhang, *Chem. Soc. Rev.* **2012**, *41*, 797.

[7] P. J. Hall, M. Mirzaeian, S. I. Fletcher, F. B. Sillars, A. J. R. Rennie, G. O. Shitta-Bey, G. Wilson, A. Cruden, R. Carter, *Energy Environ. Sci.* **2010**, *3,* 1238.

[8] D. S. Su, R. Schlögl, *ChemSusChem* **2010**, *3*, 136.

[9] H.-P. Cong, X.-C. Ren, P. Wang, S.-H. Yu, *Energy Environ. Sci.* **2010**, *6*, 1185.

[10] M. M. Jaramillo, A. Mendoza, S. Vaquero, M. Anderson, J. Palma, R. Marcilla, *RCS Adv.* **2012**, *2*, 8439.

[11] M. Seredych, M. Koscinski, M. Sliwinska-Bartkowiak, T. J. Bandosz, *J. Power Sorces* **2012**, *220*, 243.

[12] L.-Z. Fan, Y.-S. Hu, J. Maier, P. Adelhelm, B. Smarsly, M. Antonietti, *Adv. Funct. Mater.* **2007**, *17*, 3083.

[13] K. Sakaushi, G. Nickerl, F. M. Wisser, D. Nishio-Hamane, E. Hosono, H. Zhou, S. Kaskel, J. Eckert, *Angew. Chem. Int. Ed.* **2012**, *51*, 7850.

[14] I. H. Kim, K. B. Kim, *J. Electrochem. Soc.* **2006,** *153,* A383.

[15] J. P. Zheng, T. R. Jow, *J. Power Sources* **1996,** *62,* 155.

[16] C. C. Hu, K. H. Chang, M. C. Lin, Y. T. Wu, *Nano Lett.* **2006,** *6,* 2690.

[17] K. S. Ryu, K. M. Kim, N. G. Park, Y. J. Park, S. H. Chang, *J. Power Sources* **2002,** *103,* 305.

[18] K. Lota, V. Khomenko, E. Frackowiak, *J. Phys. Chem. Solids* **2004,** *65,* 295.

[19] W. Li, J. Chen, J. Zhao, R. Zhang, R. Zhu, *J. Mater. Sci. Lett.* **2005,** *59,* 800.

[20] H. Zhu, X. Wang, X. Liu, X. Yan, *Adv. Mater.* **2012**, *24*, 6524.

[21] C. Ma, Y. Song, J. Shi, D. Zhang, X. Zhai, M. Zhong, Q. Guo, L. Liu, *Carbon* **2013,** *51,* 290.

[22] S. Roldan, C. Blanco, M. Granda, R. Menendez, R. Santamaria, *Angew. Chem. Int. Ed.* **2011,** *50,* 1699.

[23] L. Wei, M. Sevilla, A. B. Fuertes, R. Mokaya, G. Yushin, *Adv. Funct. Mater.* **2012,** *22,* 827.

[24] H. F. Li, R. D. Wang, R. Cao, *Microporous Mesoporous Mater.* **2008,** *111,* 32.

[25] C. Z. Yuan, L. Chen, B. Gao, L. H. Su, X. G. Zhang, *J. Mater. Chem.* **2009,** *19,* 246.

[26] Y. G. Wang, H. Q. Li, Y. Y. Xia, *Adv. Mater.* **2006,** *18,* 2619.

[27] L. X. Li, H. H. Song, Q. C. Zhang, J. Y. Yao, X. H. Chen, *J. Power Sources* **2009,** *187,* 268.

[28] M. Galinski, A. Lewandowski, I. Stepniak, *Electrochim. Acta,* **2006,** *51,* 5567.

[29] J. Carche, C. K. Dyer, P. T. Moseley, Z. Ogumi, D. A. J. Rand, B. Scrosati, *Encyclopedia of Electrochemical Power Sources,* Elsevier B.V., 2009.

[30] A. Lewandowski, M. Galinski, *J. Phys. Chem. Solids* **2004,** *64,* 281.

[31] S. Roldan, M. Granda, R. Menendez, R. Santamaria, C. Blanco, *J. Phys. Chem. C* **2011,** *115,* 17606.

[32] S. T. Senthilkumar, R. K. Selvan, Y. S. Lee, J. S. Meloc, *J. Mater. Chem. A,* **2013,** *1,* 1086.

[33] G. Lota, E. Frackowiak, *J. Electroanal. Chem.* **2007,** *611,* 43.

[34] S. Roldan, M. Granda, R. Menendez, R. Santamaria, C. Blanco, *Electrochim. Acta* **2012,** *83,* 241.

[35] J. Wu, H. Yu, L. Fan, G. Luo, J. Lin, M. Huang, *J. Mater. Chem.* **2012,** *22,* 19025.

[36] P. S. Robertson, J. Vaughan, *J. Am. Chem. Soc.* **1958,** *80,* 2691.

[37] D. M. Johnson, P. G. Ramussen, *Macromolecules* **2000,** *33,* 8597.

[38] D. M. Johnson, S. E. Reybuck, R. G. Lawton, P. G. Ramussen, *Macromolecules* **2005,** *38,* 3615.

[39] F. Beguin, E. Frackowiak, *Adsorption by Carbons,* Elsevier, 2008.

[40] V. Aravindan, J. Gnanaraj, Y. Lee, S. Madhavi, *J. Mater. Chem. A,* **2013,** *1,* 3518.

[41] B. E. Conway, *Electrochemical Supercapacitors: Scientific Fundamentals and Technological Applications,* Kluwer Academic/Plenum Publisher, New York, 1999.

[42] A. G. Pandolfo, A. F. Hollenkamp, *J. Power Sources* **2006,** *157,* 11.

[43] http://www.innoresearch.net/report_summary.aspx?id=71&pg=171&rcd=ET-111&pd=2/1/2010

[44] http://www.umicore.com/investorrelations/en/newsPublications/presentations/2008/20080603_AdvancedMaterials_EN.pdf

[45] G. Lota, K. Fic, E. Frackowiak, *Energy Environ. Sci.* **2011,** *4,* 1592.

[46] C. Liu, Z. Yu, D. Neff, A. Zhamu, B. Z. Jang, *Nano Lett.* **2010,** *10,* 4863.

[47] K. Fic, E. Frackowiak, F. Beguin, *J. Mater. Chem.* **2012,** *22,* 24213.
[48] Y. Wan, Y. F. Shi, D. Y. Zhao, *Chem. Mater.* **2008,** *20,* 932.
[49] C. D. Liang, Z. J. Li, S. Dai, *Angew. Chem., Int. Ed.* **2008,** *47,* 3696.
[50] Y. Xia, Z. Yanga, R. Mokaya, *Nanoscale,* **2010,** *2,* 639.
[51] D. Feng, Y. Lv, Z. Wu, Y. Dou, L. Han, Z. Sun, Y. Xia, G. Zheng, D. Zhao, *J. Am. Chem. Soc.* **2011,** *133,* 15148.
[52] A. H. Lu, F. Schuth, *Adv. Mater.* **2006,** *18,* 1793.
[53] R. Ryoo, S. H. Joo, M. Kruk, M. Jaroniec, *Adv. Mater.* **2001,** *13,* 677.
[54] J. Wang, S. Kaskel, *J. Mater. Chem.* **2012,** *22,* 23710.
[55] T. Otowa, R. Tanibata, M. Itoh, *Gas Sep. Purif.* **1993,** *7,* 241.
[56] D. Lozano-Castello, J. M. Calo, D. Cazorla-Amoros, A. Linares-Solano, *Carbon,* **2007,** *45,* 2529.
[57] E. Raymundo-Pinero, P. Azais, T. Cacciaguerra, D. Cazorla-Amoros, A. Linares-Solano, F. Beguin, *Carbon,* **2005,** *43,* 786.
[58] W. Qiao, S.-H. Yoon, I. Mochida, *Energy Fuels* **2006,** *20,* 1680.
[59] H. Wang, Q. Gao, J. Hu, *J. Am. Chem. Soc.* **2009,** *131,* 7016.
[60] A. Swiatkowski, *in Studies in Surface Science and Catalysis,* Elsevier, 1999.
[61] J. Chmiola, G. Yushin, R. Dash, Y. Gogotsi, *J.Power Sources* **2006,** *158,* 765.
[62] D. Lozano-Castello, D. Cazorla-Amoros, A. Linares-Solano, S. Shiraishi, H. Kurihara, A. Oya, *Carbon* **2003,** *41,* 1765.
[63] K. Kierzek, E. Frackowiak, G. Lota, G. Gryglewicz, J. Machnikowski, *Electrochim. Acta* **2004,** *49,* 515.
[64] D. Qu, H. Shi, *J. Power Sources,* **1998,** *74,* 99.
[65] G. Gryglewicz, J. Machnikowski, E. Lorenc-Grabowska, G. Lota, E. Frackowiak, *Electrochim. Acta,* **2006,** *50,* 1197.
[66] G. Sun, W. Song, X. Liu, D. Long, W. Qiao, L. Ling, *Electrochim. Acta,* **2011,** *56,* 9248.
[67] H. T. Wang, J. F. Ya, *Ind. Eng. Chem. Res.* **2006,** *45,* 6393.
[68] M. M. Titirici, M. Antonietti, *Chem. Soc. Rev.* **2010,** *3* , 103.
[69] S. M. Saufi, A. F. Ismail, *Carbon* **2004,** *42,* 241.
[70] M .Inagaki, H. Konno, O. Tanaike, *J. Power Sorces* **2010,** *195,* 7880.
[71] S. Trasatti, *Electrochim. Acta* **1991,** *36,* 225.
[72] S. W. Donne, A. F. Hollenkamp, B. C. Jones, *J. Power Sources,* **2010,** *195,* 367.
[73] P. J. Kulesza, S. Zamponi, M. A. Malik, M. Berrettoni, A. Wolkiewicz, R. Marassi, *Electrochim. Acta* **1998,** *43,* 919.

[74] T. Y. Wei, C. H. Chen, K. H. Chang, S. Y. Lu, C. C. Hu, *Chem. Mater.* **2009,** *21,* 3228.

[75] J. Xu, L. Gao, J. Cao, W. Wang, Z. Chen, *Electrochim. Acta* **2010,** *56,* 732.

[76] X. Zhao, C. Johnston, P. S. Grant, *J. Mater. Chem.* **2009,** *19,* 8755.

[77] H. Y. Lee, J. B. Goodenough, *J. Solid State Chem.* **1999,** *148,* 81.

[78] E. B. Castro, S. G. Real, L. F. D. Pinheiro, *Int. J. Hydrogen Energy* **2004,** *29,* 255.

[79] V. Gupta, T. Kawaguchi, N. Miura, *Mater. Res. Bull.* **2009,** *44,* 202.

[80] J. Cheng, G. P. Cao, Y. S. Yang, *J. Power Sources* **2006,** *159,* 734.

[81] H. Y. Lee, J. B. Goodenough, *J. Solid State Chem.* **1999,** *144,* 220.

[82] E. Raymundo-Pinero, V. Khomenko, E. Frackowiak, F. Beguin, *J. Electrochem. Soc.* **2005,** *152,* A229.

[83] K. R. Prasad, N. Miura, *J. Power Sources* **2004,** *135,* 354.

[84] A. Clemente, S. Panero, E. Spila, B. Scrosati, *Solid State Ionics* **1996,** *85,* 273.

[85] A. Laforgue, P. Simon, C. Sarrazin, J. F. Fauvarque, *J. Power Sources* **1999,** *80,* 142.

[86] C. Arbizzani, M. Mastragostino, F. Soavi, *J. Power Sources* **2001,** *100,* 164.

[87] A. Rudge, I. Raistrick, S. Gottesfeld, J. P. Ferraris, *Electrochim. Acta* **1994,** *39,* 273.

[88] K. Naoi, S. Suematsu, A. Manago, *J. Electrochem. Soc.* **2000,** *147,* 420.

[89] M. Kawaguchi, T. Yamanaka, Y. Hayashi, H. Oda, *J. Electrochem. Soc.* **2010,** *157,* A35.

[90] L. Zhao, L.-Z. Fan, M.-Q. Zhou, H. Guan, S. Qiao, M. Antonietti, M.-M. Titirici, *Adv. Mater.* **2010,** *22,* 5202.

[91] C. O. Ania, V. Khomenko, E. Raymundo-Pinero, J. B. Parra, F. Beguin, *Adv. Funct. Mater.* **2007,** *17,* 1828.

[92] K. Xie, X. Qin, X. Wang, Y. Wang, H. Tao, Q. Wu, L. Yang, Z. Hu, *Adv. Mater.* **2012,** *24,* 347.

[93] J. Lang, X. Yan, W. Liu, R. Wang, Q. Xue, *J. Power Sources* **2012,** *204,* 220.

[94] S. Roldan, I. Villar, V. Ruiz, C. Blanco, M. Granda, R. Menendez, R. Santamaria, *Energy Fuels* **2010,** *24,* 3422.

[95] A. Alonso, V. Ruiz, C. Blanco, R. Santamaria, M. Granda, R. Menendez, S. G. E. Jager, *Carbon* **2006,** *44,* 441.

[96] M. D. Stoller, R. S. Ruoff, *Energy Environ. Sci.* **2010,** *9,* 1294.

[97] D. Hulicova-Jurcakova, M. Seredych, G. Q. Lu, Q. T. J. Bandosz, *Adv. Funct. Mater.* **2009,** *19,* 438.

[98] M. Inagaki, H, Konno, O. Tanaike, *J. Power Sorces* **2010,** *195,* 7880.

[99] B. E. Conway, V. Birss, J. Wojtowicz, *J. Power Sources* **1997,** *66,* 1.
[100] E. Frackowiak, F. Beguin, *Carbon* **2001,** *39,* 937.
[101] M. J. Bleda-Martinez, J. A. Macia-Agullo, D. Lozano-Castello, E. Morallon, D. Cazorla-Amoros, A. Linares-Solano, *Carbon* **2005,** *43,* 2677.
[102] V. Ruiz, C. Blanco, E. Raymundo-Pinero, V. Kohmenko, F. Beguin, R. Santamaria, *Electrochim. Acta* **2007,** *52,* 4969.
[103] C. Hsieh, H. Teng, *Carbon* **2002,** *40,* 667.
[104] K. Okajima, K. Ohta, M. Sudoh, *Electrochim. Acta* **2005,** *50,* 2227.
[105] Y. R. Nian, H. Teng, *J. Electrochem. Soc.* **2002,** *149,* A1008.
[106] H. Oda, A. Yamashita, S. Minoura, M. Okamoto, T. Morimoto, *J. Power Sources* **2006,** *158,* 1510.
[107] C. Hu, C. Wang, *J. Power Sources* **2004,** *125,* 299.
[108] K. Jurewicz, R. Pietrzak, P. Nowicki, H. Wachowska, *Electrochim. Acta* **2008,** *53,* 5469.
[109] D. Hulicova, M. Kodama, H. Hatori, *Chem. Mater.* **2006,** *18,* 2318.
[110] G. Lota, B. Grzyb, H. Machnikowaka, J. Machnikowaki, E. Frackowiak, *Chem. Phys. Lett.* **2005,** *404,* 53.
[111] E. Frackowiak, G. Lota, J. Machnikowski, C. Vix-Gutrl, F. Beguin, *Electrochim. Acta* **2006,** *51,* 2209.
[112] N. Fechler, T.-P. Fellinger, M. Antonietti, *Adv. Mater.* **2013,** *25,* 75.
[113] S. Brunauer, P. Emmett, E. Teller, *J. Am. Chem. Soc.* **1938,** *60,* 309.
[114] P. I. Ravikovitch, A. Vishnyakov, A. V. Neimark, *Phys. Rev. E* **2001,** *64,* 011602.
[115] L. Wei, G. Yushin, *J. Power Sorces* **2011,** *196,* 4072.
[116] Q. Zhang, J. Rong, D. Ma, B. Wei, *Energy Environ. Sci.* **2011,** *4,* 2152.
[117] R. Kotz, M. Carlen, *Electrochim. Acta* **2000,** *45,* 2482.
[118] K. E. Johnson, *Electrochem. Soc. Interface* **2007,** *16,* 38.
[119] C. Largeot, C. Portet, J. Chmiola, P. Taberna, Y. Gogotsi, P. Simon, *J. Am. Chem. Soc.* **2008,** *130,* 2730.
[120] M. Galinski, A. Lewandowski, *Electrochim. Acta* **2006,** *51,* 5567.
[121] Q. Li, X. Li, C. Sun, Y. Li, *Electrochem. Commun.* **2009,** *11,* 87.
[122] S. Roldan, Z. Gonzalez, C. Blanco, M. Granda, R. Menendez, R. Santamaria, *Electrochim. Acta* **2011,** *56,* 3401.
[123] J. H. White, M. P. Soriaga, A. T. Hubbard, *Electroanal. Chem.* **1985,** *185,* 331.
[124] M. Quan, D. Sanchez, M. F. Wasylkiw, D. K. Smith, *J. Am. Chem. Soc.* **2007,** *129,* 12847.
[125] J. Robertson, *Mater. Sci. Eng. R* **2002,** *37,* 129.

[126] M. Agemi, K. Kayama, M. Noborisaka, Y. Tachimoto, A. Shirakura, T. Suzuki, *Surf. Coat. Tech.* **2011,** *206,* 2025.

[127] W. Zhang, Y. Xia, J. Ju, L. Wang, Z. Fang, M. Zhang, *Solid State Commun.* **2003,** *126,* 163.

[128] S. V. Singh, T. Zaharia, M. Creatore, R. Groenen, K. V. Hege, M. C. M. Sanden, *J. Appl. Phys.* **2010,** *107,* 013305.

[129] O. S. Panwar, Ishpal, R. K. Tripathi, A. K. Srivastava, M. Kumar, S. Kumar, *Diam. Relat. Mater.* **2012,** *25,* 63.

[130] A. Shirakura, M. Nakaya, Y. Koga, H. Kodama, T. Hasebe, T. Suzuki, *Thin Solid Films* **2006,** *494,* 84.

[131] H. C. Foley, *Microporous Mater.* **1995,** *4,* 407.

[132] Chung, D. *Materials for Electronic Packaging,* 1st Edition Butterworth-Heinemann.

[133] N. M. S. Marins, R. P. Mota, R. Y. Honda, P. A. P. Nascente, M. E. Kayama, K. G. Kostov, M. A. Algatti, N. C. Cruz, E. C. Rangel, *Surf. Coat. Tech.* **2011,** *206,* 640.

[134] A. C. Ferrari, J. Robertson, *Phys. Rev. B* **2000,** *61,* 14095.

[135] J. Diaz, G. Paolicelli, S. Ferrer, F. Comin, *Phys. Rev. B,* **1996,** *54,* 8064.

[136] D. R. McKenzie, *Rep. Prog. Phys.* **1996,** *59,* 1611.

[137] O. R. Monteiro, *Annu. Rev. Mater. Res.* **2001,** *31,* 111.

[138] Z. R. Ismagilov, A. E. Shalagina, O. Y. Podyacheva, A. V. Ischenko, L. S. Kibis, A. I. Boronin, Y. A. Chesalov, D. I. Kochubey, A. I. Romanenko, O. B. Anikeeva, T. I. Buryakov, E. N. Tkachev, *Carbon* **2009,** *47,* 1922.

[139] H. Sjostrom, S. Stafstrom, M. Boman, J.-E. Sundgren, *Phys. Rev. Lett.* **1995,** *75,* 1336.

[140] N. Hellgren, M. P. Johansson, E. Broitman, L. Hultman, J.-E. Sundgren, *Phys. Rev. B* **1999,** *59,* 5162.

[141] K. L. Choy, *Prog. Mater. Sci.* **2003,** *48,* 57.

[142] D. J. Choi, W. H. Koo, S. M. Jeong, D. W. Han, D. Y. Lee, H. K. Baik, S. W. Jang, S. M. Lee, *Vacuum* **2004,** *72,* 445.

[143] P. Tian, X. Zhang, Q. Z. Xue, *Carbon* **2007,** *45,* 1764.

[144] J. G. Buijnsters, R. Gago, I. Jimenez, M. Camero, F. Agullo-Rueda, C. Gomez-Aleixandre, *J. Appl. Phys.* **2009,** *105,* 093510.

[145] O. S. Panwar, M. A. Khan, M. Kumar, S. M. Shivaprasad, B. S. Satyanarayana, P. N. Dixit, R. Bhattacharya, M. Y. Khan, *Thin Solid Films* **2008,** *516,* 2331.

[146] Y. Yamada, T. Tanaka, K. Machida, S. Suematsu, K. Tamamitsu, H. Kataura, H. Hatori, *Carbon* **2012,** *50,* 1422.
[147] C. Casiraghi, A. C. Ferrari, J. Robertson, *Phys. Rev. B* **2005,** *72,* 085401.
[148] Y. Miyajima, S. J. Henley, S. R. P. Silva, *Thin Solid Films* **2011,** *519,* 6374.
[149] J. M. Lackner, W. Waldhauser, *J. Adh. Sci. Tech.* **2010,** *24,* 925.
[150] S. Liua, G. Wang, Z. Wang, *J Non-Cryst. Solids* **2007,** *353,* 2796.
[151] S. Adhikari, M. Umeno, *J. Mod. Phys. B* **2009,** *23,* 2159.
[152] S. Y. Liu, C. M. Zhen, Y. Z. Li, C. F. Pan, H. J. Zhou, D. L. Hou, *J. Appl. Phys.* **2012,** *111,* 053922.
[153] F. M. Wang, M. W. Chen, Q. B. Lai, *Thin Solid Films* **2010,** *518,* 3332.
[154] G. S. Cordeiro, R. S. Rocha, R. B. Valim, F. L. Migliorini, M. R. Baldan, M. R. V. Lanza, N. G. Ferreira, *Diam. Relat. Mater.* **2013,** *32,* 54.
[155] C. Wan, X. Zhang, X. Zhang, X. Gao, X. Tan, *Appl. Phys. Lett.* **2009,** *95,* 022105.
[156] A. Liu, J. Zhu, J. Han, H. Wu, W. Gao, *Electroanalysis* **2007,** *19,* 1773.
[157] F. C. Krebs, *Energ. Mat. Sol. C.* **2009,** *93,* 394.
[158] N. Sahu, B. Parija, S. Panigrahi, *Indian J. Phys.* **2009,** *83,* 493.
[159] K. M. Coakley, M. D. McGehee, *Chem. Mater.* **2004,** *16,* 4533.
[160] H. Hoppe, N. S. Sariciftci, *J. Mater. Res.* **2004,** *19,* 1924.
[161] C. Winder, N. S. Sariciftci, *J. Mater. Chem.* **2004,** *14,* 1077.
[162] R. G. Aguilar, J. O. Lopez, *Lat. Am. J. Phys. Educ.* **2011,** *5,* 368.
[163] H. A. Becerril, J. Mao, Z. Liu, R. M. Stoltenberg, Z. Bao, Y. Chen, *ACS Nano,* **2008,** *2,* 463.
[164] D. S. Hecht, A. M. Heintz, R. Lee, L. Hu, B. Moore, C. Cucksey, S. Risser, *Nanotechnology* **2011,** *22,* 075201.
[165] L. Song, D. Feng, N. J. Fredi, K. G. Yager, R. L. Jones, Q. Wu , D. Zhao, B. D. Vogt, *ACS Nano,* **2010,** *4,* 189.
[166] M. Daranyi, I. Sarusi, A. Sapi, A. Kukovecz, Z. Konya, A. Erdohelyi, *Thin Solid Films,* **2011,** *520,* 57.
[167] L. Song, D. Feng, C. G. Campbell, D. Gu, A. M. Forster, K. G. Yager, N. Fredin, H.-J. Lee, R. L. Jones, D. Zhao, B. D. Vogt, *J. Mater. Chem.* **2010,** *20,* 1691.
[168] J. Pang, X. Li, D. Wang, Z. Wu, V. T. John, Z. Yang, Y. Lu, *Adv. Mater.* **2004,** *16,* 884.
[169] A. Singh, J. Jayaram, M. Madou, S. Akbara, *J. Electrochem. Soc.* **2001,** *149,* E78.
[170] Y. Wei, R. Hariharan, J. K. Ray, *J. Polym. Sci. Part A Polym. Chem.* **1991,** *29,* 749–758.
[171] H. J. Kim, Z. Brunovska, H. Ishida, *Polymer* **1991,** 40, 6565.

[172] P. K. Chu, L. Li, *Mater. Chem. Phys.* **2006,** *96,* 253.
[173] E. Riedo, F. Comin, J. Chevrier, F. Schmithusen, S. Decossas, M. Sancrotti, *Surf. Coat. Tech.* **2000,** *125,* 124.
[174] N. Wang, K. Komvopoulos, *IEEE Trans. Magn.* **2012,** *48,* 2220.
[175] D. Varshney, C. V. Rao, M. J.-F. Guinel, Y. Ishikawa, B. R. Weiner, G. Morell, *J. Appl. Phys.* **2011,** *110,* 044324.
[176] P. G. Ramussen, S. E. Reybuck, T. Jang, R. G. Lawton, *US patent* **1998,** 5712408.
[177] K. S. Walton, R. Q. Snurr, *J. Am. Chem. Soc.* **2007,** *129,* 8552.
[178] P. I. Ravikovitch, A. V. Neimark, *Colloid. Surface. A* **2001,** *187–188,* 11.
[179] Q. Cheng, J. Tang, J. Ma, H. Zhang, N. Shinya, L.-C. Qin, *Phys. Chem. Chem. Phys.* **2011,** *13,* 17615.
[180] J. Rouquerol, F. Rouquerol, K. S. W. Sing, *Adsorption by Powders and Porous Solids, Principles, Methodology, and Applications.* Academic Press, 1998.
[181] K. S. W. Sing, D. H. Everett, R. A. W. Haul, L. Moscau, R. A. Pierotti, J. Rouquerol, T. Siemieniewska, *Pure Appl. Chem.* **1985,** *57,* 603.
[182] K. Hozumi, *Anal. Sci.* **1993,** *9,* 167.
[183] F. Xu, Y.-C. Shi, D. Wang, *Carbohyd. Polym.* **2013,** *94,* 904.

List of abbreviations

AC	Activated carbon
AFM	Atomic force microscopy
BET	Brunauer-Emmet-Teller
CNT	Carbon nanotube
CV	Cyclic Voltammetry
CVD	Chemical vapour deposition
DAMN	Diaminomaleonitrile
DFT	Density functional theory
DMF	Dimethylformamide
DMSO	Dimethylsulphoxide
EDL	Electrical double layer
EDLC	Electrical double layer capacitor
EELS	Electron energy loss spectroscopy
EIS	Electrochemical impedance spectroscopy
ESR	Equivalent series resistance
FT-IR	Fourier-transform infrared spectroscopy
GO	Graphene oxide
GPC	Gel permeation chromatography
HQ	Hydroquinone
IL	Ionic liquid
LIB	Lithium ion battery
NLDFT	Non-local density functional theory
PVD	Physical vapour deposition
PVDF	Polyvinylidene fluoride
Q	*p*-Benzoquinone
SAED	Selected area electron diffraction
SCCF	Spin coating carbon film

SEI	Solid electrolyte interface
SEM	Scanning electron microscopy
SFC	Salt-flux carbon
TEM	Transmission electron microscopy
TFA	Trifluoroacetic acid
TIC	Total inorganic carbon
TGA	Thermogravimetric Analysis
WAXS	Wide angle X-ray scattering
XPS	X-ray photoelectron spectroscopy

Acknowledgements

This work would not have been possible without help and support of many people, to whom I am deeply grateful.

I would like to express the deepest appreciation to my supervisor Prof. Dr. Markus Antonietti for affording the opportunity to conduct my doctoral studies at Max Planck Institute of Colloids and Interfaces to me, who at first started working merely as a guest researcher. He kindly provided support, innovations, continuous encouragements and fruitful discussions throughout the development of this work.

I would like to also acknowledge my company, JSR Corporation, which accepted my research plan on heteroatom-containing carbons and permitted to work under the direction of Prof. Dr. Markus Antonietti for two years. My current boss in my company, Mr. Tatsuya Sakai is deeply appreciated for his kind support on my work and life here. Other colleagues including Mr. Hisashi Nakagawa, Dr. Taichi Matsumoto, Mr. Ryuuichi Saitou and Mr. Tomikazu Ueno should be thanked as well. Especially, I am grateful to Mr. Hisashi Nakagawa for measurement of sheet resistance and thickness, and to Mr. Tomikazu Ueno for XPS measurement.

Prof. Xinchen Wang is sincerely acknowledged for his kind communication with me before studying here as well as discussions at the beginning of my work here.

I am very grateful to Dr. Nina Fechler for affording an important knowledge on my work and for a lot of kind supports and discussions. Dr. Florian Schipper is also thanked for instructing me in the operation and the knowledge on electrochemistry. Dr. Manfred Erwin Schuster (Fritz-Haber-Institut) is acknowledged for measuring my carbon film samples by EELS and for useful discussions. Dr. Naoya Nishi (Kyoto Univ.) is thanked for useful discussions and for providing me the basic knowledge on electrochemistry.

Special Dankeschön goes to the technicians; Frau Sylvia Pirok (EA), Frau Rona Pitschke (SEM & TEM), Frau Marlies Gräwert (GPC), Frau Ursula Lubahn (TG) and Frau Anneliese Heilig (AFM). I could not have done this work without their kind supports.

Great thanks are also for all the colleagues that I have met here at the MPI during my stay here: Camillo, Constanze, Danuta, Davide, Debora, Hiro, Dr. Jiayin Yuan, Katharina, Konrad, Linghui, Liping, Liujian, Marcos, Shiori, Tim, Tristan, Vincent, Wouter, Xiaofeng, Xin-Hao, Yongjun and many others, who I cannot possibly enumerate here.

Finally, my last but greatest "thank you" goes to my family for their kind support, who accepted my plan to study abroad as well as to make a challenge to obtain a doctoral degree here. 아빠, 힘 냈어요!

"Das ist das Kennzeichen eines wirklich bewundernswerten Mannes:

Standhaftigkeit im Angesicht von Schwierigkeiten."

–Ludwig van Beethoven zugeschrieben–